Summer 2012

A progressive collapse evaluation of steel structures in high temperature environment with optical fiber sensors

Ying Huang

A PROGRESSIVE COLLAPSE EVALUATION OF STEEL STRUCTURES IN HIGH TEMPERATURE ENVIRONMENT WITH OPTICAL FIBER SENSORS

by

YING HUANG

A DISSERTATION

Presented to the Faculty of the Graduate School of the

MISSOURI UNIVERSITY OF SCIENCE AND TECHNOLOGY

In Partial Fulfillment of the Requirements for the Degree

DOCTOR OF PHILOSOPHY

in

CIVIL ENGINEERING

2012

Approved by

Dr. Genda Chen, Advisor
Dr. Hai Xiao, Co-Advisor
Dr. K. Chandrashekhara
Dr. John Myers
Dr. Lesley Sneed

ABSTRACT

In the process of a progressive failure of steel structures in a post-earthquake fire, real-time assessment and prediction of structural behaviors are of paramount significance to an emergency evacuation and rescue effort. However, existing measurement technologies cannot provide the needed critical data such as large strains at high temperature. To bridge this gap, a novel optical fiber sensor network and an adaptive multi-scale finite element model (FEM) are proposed and developed in this study. The sensor network consists of long period fiber gratings (LPFG) sensors and extrinsic Fabry-Perot interferometer (EFPI) sensors or their integration. Each sensor is designed with a three-tier structure for an accurate and reliable measurement of large strains and for ease of installation. To maintain a balance between the total cost of computation and instrumentation and the accuracy in numerical simulation, a structure is divided into representative/critical components instrumented densely and the remaining components simulated computationally. The critical components and the remaining were modeled in different scales with fiber elements and beam/plate elements, respectively, so that the material behavior and load information measured from the critical components are representative to the remaining components and can be used to update the temperature distribution of the structure in real time. Sensitivity studies on the number of sensors and the initial selection of an updating temperature parameter were conducted. Both the sensor network and the FEM were validated with laboratory tests of a single-bay, one-story steel frame under simulated post-earthquake fire conditions. The validated FEM was applied to a two-bay, four-story steel building under the 1995 Kobe earthquake excitations. Based on extensive tests and analyses, the proposed sensor can measure a strain of 12% at as high as 800 ℃ (1472 ℉) in temperature. Within the application range, the LPFG wavelength and the EFPI gap change linearly with the applied strain and temperature. The proposed updating criterion and algorithm in the adaptive FEM are proven to be effective. The number of sensors is sufficient in engineering applications as long as the sensors can adequately represent the material behavior of the instrumented components. The predicted structural behavior is unaffected by any change in a low temperature range and thus insensitive to the initial selection of the updating parameter.

ACKNOWLEDGMENTS

The author wishes to express her sincere gratitude to Drs. G. Chen and H. Xiao for providing constant guidance, advice, and encouragement during her graduate study at Missouri University of Science and Technology. She will never forget the countless hours of discussion with Dr. G. Chen. Special thanks are also due to him for providing an excellent working environment and supporting the author in every aspect. It has been a privilege and a pleasure to have worked with him.

Appreciation is extended to the members of the advisory committee, Drs. K. Chandrashekhara, J. J. Myers, and L. Sneed for their valuable time, advice and effort to review this dissertation.

The author also appreciates the assistance from her fellow colleagues and friends during various laboratory tests, including Dr. Z. Zhou, Dr. T. Wei, Dr. Z. Wang, Dr. Z. Gao, Mr. F. Tang, Mr. X. W. Lan, Miss. Y. N. Zhang, and Mr. W. J. Bevans.

The author would also like to acknowledge the financial support in the form of a Graduate Assistantship through grants and contracts from the U.S. National Science Foundation under Award No. CMMI-0825942 and Mid-America Transportation Center under several awards including Award No. 25-1121-0001-345.

Finally, the author wishes to express her deepest gratitude to her parents, her husband, her sisters and friends for their understanding, patience, encouragement, support, and for helping realize and accomplish her dreams.

TABLE OF CONTENTS

LIST OF ILLUSTRATIONS

Page

LIST OF TABLES

Page

1. INTRODUCTION

1.1. BACKGROUND

Steel is a commonly-used material in civil engineering due to its ductile behavior and desirable physical properties such as high strength and toughness, uniformity, and ease to erect. It is one of the most versatile construction materials for large-scale infrastructures such as long-span bridges, high-rise buildings, pipelines and towers. However, steel structures are disadvantageous over concrete structures in that they are relatively high in maintenance cost, low in fire resistance, and susceptible to buckling under compression in harsh environments. For example, the material properties of steel can be significantly changed at evaluated temperatures. With respect to ambient temperature, the yield strength of steel is reduced to 23% at 700 ℃ (1292 ℉), 11% at 800 ℃ (1472 ℉), and 6% at 900 ℃ (1652 ℉) [1]. In these harsh environments, some of steel components may fail due to their susceptibility to buckling under gravity loads, leading to the progressive collapse of entire structures.

Progressive collapse of a structure often initiates from the damage or failure of a relatively small part of the structure [2]. This phenomenon is often associated with a disproportionate design of the structure. Minor damage at one or more locations may result in an unstable structural system. For example, a seven-story steel building in the University of Aberdeen Zoology, Aberdeen, Scotland, failed entirely during construction on November 1, 1966, causing five deaths and three injuries. The world's first example of the total progressive collapse of a steel-frame building was caused by the fatigue failure at poor girder welds under wind loads. On September 11, 2001, the twin towers of the World Trade Center, New York, U.S.A., collapsed progressively following a terrorist attack and the induced subsequent fires, claimed for 2,752 lives. The 2001 tragedy attracted a worldwide attention to the progressive failure of steel structures in harsh environments. After three years of investigation on the collapse of the World Trade Center by the National Institute of Standards and Technology (NIST), the cause for the initiation of the progressive collapse was attributed to the instability of the attacked floors after the loss of fire protection from impact and explosion, and the creep buckling induced by the prolonged heating of steel columns up to 800 ℃ (1472 ℉). The falling

superstructure as a rigid body further induced dynamic overloads to the remaining structure, leading to a complete collapse of the whole building system [3].

Therefore, the behavior of steel structures in harsh environments such as earthquakes, explosions, and fires becomes extremely important for their safety evaluation. Critical buildings, such as hospitals and police stations, must remain functional even in harsh environments, for example, immediately following a major earthquake-induced or man-made fire event. Due to earthquake or explosion effects, buildings often experience inelastic behavior (large strains), leading to progressive collapses. During this process, tenants could be injured and trapped in the collapsed structures. The induced high temperature environment can accelerate the collapse process in steel structure, increasing difficulties for post-earthquake or post-attack rescues. Therefore, monitoring and assessing the health condition of critical buildings is of paramount importance to the post-event response and evacuation in earthquake-prone regions. An accurate assessment of building conditions in harsh environments can assist fire fighters in rescuing earthquake or attack victims.

1.2. LITERATURE REVIEW ON STATE-OF-THE-ART DEVELOPMENT

1.2.1. Structural Health Monitoring and Assessment. To assess the condition of an engineering structure, the most direct parameter and information to take may be the stress distribution of the structure under various loads. However, stress measurement is often not feasible, if not impossible, in practical applications. In most cases, strain distribution instead is measured and related to the stress distribution by a well-calibrated material constitutive relation. For steel structures, uniform material properties can be obtained experimentally. Up to date, the most widely used and commercialized technique for strain sensing/measurements are electrical resistance gauges or strain gauges.

Strain gauges were firstly proposed in 1856 by Lord Kelvin [5]. A strain gauge is attached to an object by appropriate adhesives such as cyanoacrylate. Once installed, it will deform together with the object under loading, which changes the electrical resistance of the gauge. By recording the change in electrical resistance, the strain applied on the object can be correlated and obtained. As a well-developed technology, strain

gauges have several advantages: simple concept, easy installation, and relatively lower cost. However, due to electromechanical properties of the alloys, backing materials and the adhesives used to install strain gauges, the maximum strain that can be measured by strain gauges prior to their failure is limited to approximately 1.5%. For strains higher than 1.5%, extensometers, linear variable differential transformers [6], grating based mark tracking techniques [7, 8], and conductive textiles [9] are commonly used. These methods can measure a strain of up to 5%, but suffer from low resolution of 4,500 με or 0.45%. In addition to the limited strain dynamic range, the allowable working temperature of the strain gauges must be less than 200 ℃ (392 ℉), which will limit SHM applications for civil engineering structures in harsh environments. Although strain gauges were modified for harsh environment applications in the last decade [10, 11], they had a significantly reduced dynamic measurement range as the required temperature increased.

As discussed in Section 1.1, the material properties of steel change with temperature in high temperature environments. In addition to strain measurement, temperature measurements are also important for steel structures in harsh environments such as explosion and fire effects. Therefore, high temperature measurement becomes another critical topic in SHM systems. Several commercial products are available for temperature measurements. Among them, thermocouple is the most widely used and commercialized one.

Thermocouples were firstly proposed in 1822 by Fourier and Oersted following the discovering of thermoelectricity principle by Thomas in 1821 [12]. Since then, thermocouples had been well developed and widely used for high temperature measurements. The types of thermocouples currently available include Type K, E, J, N, B, R, S, T, C, and M. However, with the use of electrical wire connections, thermocouples would likely lose their signals due to power outage during a strong earthquake when structures being monitored are subjected to large strains in a fire.

To solve the above issue with the traditional sensing technology, optical fiber sensors have recently been proposed as one of the potential solutions for SHM in harsh environments due to their unique and inherent advantages of lightweight, compact size, remote and real-time sensing capability, low power consumption, resistance to

electromagnetic interference, high sensitivity, wide bandwidth, environmental ruggedness, and independence on electric power [13].

1.2.2. Optical Fiber Based Sensing Techniques. A fiber optic sensor is a device that uses optical fiber either as a sensing element in intrinsic sensors or as a signal transmission medium from a remote sensor to the electronics that process the received signal, called the extrinsic sensors. Optical fiber is made of glass; its refractive index can be changed with the applied stress or strain, which is referred to as a photo-elastic effect. By modulating some of the fiber properties such as intensity, wavelength, phase, polarization, and transmission time of light, the optical fiber is sensitive to the effects of strain, temperature, and pressure; it can thus become a sensing unit as a component of a SHM system. Based on the modulation and demodulation process, optical fiber sensors can be classified into intensity, grating, and interferometer based devices [14].

Among various optical fiber sensors, the intensity based one is the simplest; it only requires a light source and a corresponding light detector in application [15]. To obtain a change in intensity as light transmits through an optical fiber, many transduction mechanisms can be used; they include micro bending loss [16], breakage [17], fiber-to-fiber coupling, modified cladding [18], reflectance [19], absorption, attenuation, molecular scattering, molecular effect, and evanescent field [20]. Although the intensity based optical sensors have been used for years, they still have a number of limitations associated with light intensity losses in the optical fiber instead of structural and/or environmental effects to be measured. The potential sources for these intensity losses are attributed to imperfect connectors and splices, unexpected micro/macro bending, mechanical creep, and misalignment of light sources and detectors. To improve the performance of intensity based optical fiber sensors, dual wavelengths are sometimes applied with one as a reference and the other for sensing [21].

Grating based optical sensors were developed along two main directions: fiber Bragg gratings (FBG) and long period fiber gratings (LPFG). An FBG sensor couples two light strings in their respective forward- and backward-propagating core-guided modes near a resonant wavelength, functioning like a wavelength-selective mirror [22]. It reflects light with a particular wavelength, called Bragg wavelength, and transmits the

others. Therefore, an applied strain or temperature will shift the Bragg wavelength and in turn can be detected by tracking the Bragg wavelength change from either the reflected or the transmitted wave. The first in-fiber Bragg grating was demonstrated by Ken in 1978 [23]. Initially, visible lasers propagating along the core of a fiber were used to inscribe the FBG sensor. In 1989, Gerald et al. [24] developed a much more flexible transverse holographic inscription technique using the interference pattern of an ultraviolet laser light illumination from the side of the fiber, greatly accelerating the practical application of FBG sensors in SHM systems. Compared to other grating based optic fiber sensors, FBG sensors have their advantages such as insensitivity to the surrounding refractive index change, compact size, and ability for quasi-distributed sensing, which placed FBG sensors as the most well-developed and commonly-used optical fiber sensors in civil engineering. The most attractive feature of FBG sensors is the capability of integrating a large number of FBG sensors in a single fiber so that a quasi-distributed optical fiber sensing system can be achieved in a cost-effective way [25]. With the rapid development of optical communication networks, by using the wavelength division multiplexing technique [26], more than 100 FBG sensors can be placed in one single fiber. Furthermore, by combining other methods such as time and frequency division multiplexing method [27], the number of sensors can be further increased in one optical fiber at a fractional cost.

With a periodic refractive index perturbation in its fiber core at a hundreds-of-micrometer scale, an LPFG sensor couples the guided light inside the fiber core into the cladding modes at certain discrete wavelengths known as resonance wavelengths. With co-propagating modes coupled, the multiple resonances of a LPFG sensor can be observed in a transmission spectrum at different valleys and wavelengths corresponding to various cladding modes in a single-mode fiber [28, 29]. The resonant wavelengths can be influenced by an applied strain, temperature, or environmental changes. The first long period grating was successfully inscribed on an optical fiber in 1996 [28] and the modulation of a periodic effective index change between the core and cladding of a LPFG sensor can be achieved by UV irradiation [30] and CO_2 laser irradiation [31]. With different fabrication methods, LPFG sensors have different properties for strain and temperature measurements. The strain and temperature properties of UV-induced LPFG

sensors have been widely investigated in the past few years, highly depending on the types of fibers due to their diverse strain-optic coefficients [32]. Compared to the UV-induced LPFGs, CO_2 laser induced LPFG sensors have a larger dynamic range of temperature measurements and thus become a better candidate for high temperature applications. In addition, with multiple resonances in one single fiber, the LPFG sensors are promising devices for multiple parameter measurements [33, 34]. Furthermore, due to their high sensitivity to environmental and temperature changes [35], LPFG sensors have been widely investigated for various applications for temperature [36, 37], strain [38], chemical [39], pH [40], and bio-sensing [41].

An interferometer-based optical fiber sensor measures interference fringes that are formed as two or more light streams merge in an optical instrument [42]. The interference signal contains information on the sensor head structure and position of interest. Optical interferometer sensors can be made in several forms, for example, with fiber Mach–Zehnder interferometer [43], Michelson interferometer [44], Fabry–Perot interferometer [45], and Sagnac interferometer [46]. Among various optical interferometers, Fabry–Perot interferometer (FPI) is the most sensitive to the change in cavity when light bounces back and forth for multiple times between the two highly reflective fiber mirrors. Therefore, FPI based optical fiber sensors have been widely applied in the field of sensors and sensing systems for strain [47], temperature [48], chemical or bio-sensing [49], and even corrosion measurements [50].

With their rapid development, optical fiber sensors have been applied in the past two decades into the SHM of civil engineering buildings in harsh environments, where a strain measurement of larger than 5% was required at over 500 ℃ (932 ℉). Both grating based [51, 52] and interferometer based sensors [53, 54] have been investigated. However, existing grating based fiber optical sensors often have a relatively small dynamic range due to the limited deformability of silica glass. For example, the break-strain for an uncoated fiber grating sensor is approximately 1%. To overcome this shortcoming, various coating techniques [55] and strain transfer mechanisms have recently been developed and applied to large strain measurements [34, 56]. Even so, the maximum strain that can be measured with existing fiber optical sensors is limited to 2.4%, which is still low to study the progressive collapse of structural systems under

extreme loads. For extrinsic Fabry-Perot interferometer (EFPI) sensors, they also have a limited dynamic range due to the use of a typical sensor structure design. In 1994, a concept of the movable EFPI sensor was developed [57]; the sensor was applied to measure strains during the first few hours of concrete hydration reaction [58-60]. Although only a small strain range had been investigated, the innovative EFPI packaging method provides an opportunity for large strain measurement at high temperature.

Based on the above reviews, large strain measurements at high temperature are still a challenging topic that requires further research and development. To date, structural health monitoring in high temperature environments is yet to be studied.

1.2.3. Finite Element Model Analysis.

1.2.3.1. FEM analysis and model updating technique. In an effort to get the realistic structural behavior of a steel structure, full-scale structural tests are preferred in harsh environments such as post-earthquake fire/explosion conditions. However, considering the complexity and cost of carrying out full-scale fire tests, only limited test data on structural behavior in real fire-involved environments are available to date. This difficulty stimulated an increasing interest in the use of numerical models. On the other hand, numerical models need to be validated with full-scale fire tests [61]. During the past two decades, significant efforts have been made to develop a high fidelity finite element model (FEM) of a steel structure for the evaluation of its progressive failure process at high temperature replicating post-earthquake fire or explosion conditions. Such a model can be used to predict the structural response to the disturbance from service environmental changes and evaluate the design advantage from the modification in configuration of the structural system [62-65]. Currently, several research- and commercial-level software tools are available for the analysis of fire hazards, loss estimation, and structural responses.

For the prediction and evaluation of structural behavior in harsh environments, a general-purpose linear model and associated commercial software may be simply used when a structure is subjected to low temperature or free to thermal expansion. In this case, the analyst must account for any yielding or other non-linear behavior by manually modifying material properties at various steps of analysis. In contrast to the linear model,

a nonlinear FEM can be established in FIRES-RC II, FASBUS II SAFIR, ABAQUS, and DIANA [66] for the progressive failure analysis in harsh environments. With nonlinear properties taken into account at every step, the relative error between tests and computer simulations can be reduced significantly. However, modeling of temperature-dependent material properties in nonlinear FEM analysis is still a major challenge [67]. In the last few decades, significant efforts were made to obtain the best estimate of temperature dependent material properties for steel structures [68-74]. In addition to these sophisticated computer simulation approaches, simplified approaches can be considered under certain circumstances. For example, relatively unrestrained steel members can be analyzed in a similar way to linear systems when the applied temperature does not exceed a temperature threshold of typically 400 ℃-500 ℃ (800 ℉-1000 ℉) at which the member stresses are well below the yield strength of steel. This is also the type of acceptance criterion used in ASTM E-119 furnace tests when assemblies are not loaded during tests [75].

When numerical predictions are compared with experimental results, it is often found that the degree of correlation is not good enough to apply the FEM with confidence [76]. Therefore, the model must be updated in time to improve the accuracy of material properties [77-79]. Up to date, most model updating studies were focused on the updating of the natural frequencies of buildings under seismic loading. No research work on temperature-dependent FEM updating has ever been investigated for a real-time structural behavior prediction of buildings in harsh environments.

1.2.3.2. Hybrid simulation with multi-scale modeling. For a large-scale civil engineering structure, full-scale model tests are extremely expensive. Even numerical analysis at such a large scale can cost a significant computational time in addition to the need for model validation with measurements. Therefore, hybrid simulation with a coupled instrumented and computational model is desirable. One part of the structure is densely instrumented and the remaining part is numerically simulated. The measured data can be used for model updating over time. The material and load information that can be directly inferred from the part of the structure instrumented can be applied to the remaining part of the structure in real time. For the evaluation of material properties, the instrumented part of the structure will be modeled with fiber elements in small scale. The

remaining part can be modeled with conventional beam and plate elements. The previous hybrid simulation experiences for earthquake analysis [80-83] are important for the development of 3-D model updating analysis with multi-scale modeling in the future.

Hybrid simulations with multiple-scale modeling can not only improve the efficiency of a FEM progressive failure analysis of steel structures in harsh environments in a cost-effective way, but also enhance the accuracy with real-time updating of the monitored data from a sensing system through the updating of material properties and service conditions such as temperature and strain. Today, civil engineering structures are designed with the load and resistance factor design (LRFD) philosophy in most parts of the world. This philosophy recognizes the uncertainty in the determination of loads and strengths [84]. A specific structure can be viewed as a sample of the structures with probabilistic loads and resistances in the LRFD design space. The material properties and external loads of the structures in the LRFD design space are not known in prior at any time of service life. Even though general properties such as the modulus of elasticity and density can be evaluated from low amplitude vibration under operational loads, critical properties for structural behavior evaluation such as yield strength of steel and tensile/compressive strengths of concrete are unable to obtain without damaging the structure. Moreover, the elastic waves due to crack nucleation generated in a solid structure may change the characteristics of noise under extreme loads. Therefore, to understand and evaluate the actual behavior of an engineering structure, real-time structural monitoring and modeling taking into account its practicality and cost restraint is necessary during an extreme event.

1.3. RESEARCH OBJECTIVES AND SCOPE OF WORK

The above literature review indicates two critical needs for the progressive collapse evaluation of steel structures in harsh environments: a novel measurement system for structural behavior monitoring and a hybrid simulation methodology for structural system assessment. Therefore, the main objectives of this study are to develop (1) a comprehensive optical fiber based sensing system and (2) a coupled instrumented and computational, multi-scale FEM that will be updated in real time at key

instrumentation locations for both material properties and structural conditions. To achieve these objectives, five technical tasks were planned as introduced in the following five sections.

1.3.1. Large Strain Measurement with Adjustable Resolution. For the monitoring and assessment of a progressive failure in post-earthquake fire environments, the most critical response parameter of a structure is the large strain distributed in the structure. For this application, the currently available strain gauges lack the measurement range of strains and corresponding resolution, particularly in harsh environments. In this task, a three-layer packaged structure of EFPI optical fiber sensors is proposed to enable the measurement of large strains in a high temperature environment. Adjustable strain resolution can be achieved with various data processing algorithms for different monitoring purposes. Sensor prototypes are designed, fabricated, and tested in the laboratory to validate the newly developed sensor concept.

1.3.2. Simultaneous Large Strain and High Temperature Measurements. Structures in a post-earthquake fire environment are not only subjected to large strains but also to high temperature environments. Therefore, large strain measurements must be done in high temperature environment or simultaneous measurements for large strain and high temperature are desirable. In this task, various optical fiber sensors are investigated and compared, including a hybrid optical fiber sensor of movable EFPI and LPFG technologies.

1.3.2.1. A temperature self-compensated LPFG sensor. In an effort to achieve a simultaneous large strain and high temperature measurement, a single LPFG sensor using two different cladding modes is attempted. The applied gratings are induced by a CO_2 laser irradiation. The two cladding modes, LP_{06} and LP_{07}, of an LPFG sensor are utilized for simultaneous measurements of strain and temperature. To improve its dynamic range for strain measurement, an LPFG sensor is packaged with a combined mechanism of elastic attachment amplification and gauge length change. The feasibility and dynamic range of the packaged single LPFG sensor are investigated both analytically and experimentally. With the use of two different cladding modes in one single LPFG

sensor, the exact temperature at the monitored location can be used to compensate strain measurements, providing a temperature self-compensated strain sensor in high temperature environments.

1.3.2.2. A hybrid LPFG/movable EFPI sensor. To further increase the dynamic range of strain measurements, a hybrid optical fiber sensor of LPFG and movable EFPI technologies is then proposed and developed. The hybrid sensor combines two optical fiber sensors in one sensor head. The movable EFPI senor can be used for large strain sensing and the LPFG sensor can be applied for high temperature measurements. Various laboratory tests are performed to validate the feasibility and performance of the newly developed hybrid sensor for simultaneous large strain and high temperature measurements.

1.3.3. Sensor Networking and Experimental Validation under Simulated Post-Earthquake Fire Conditions. For the behavior monitoring and condition assessment of a structural system, various types of optical fiber sensors are multiplexed to form a sensor network, and validated with laboratory tests. Specifically, the developed sensors are networked into a quasi-distributed optical fiber sensing system and validated through a comprehensive assessment of the inelastic structural behavior of a one-story, one-bay steel frame under simulated post-earthquake fire conditions. The sensing system consists of LPFG, EFPI, and hybrid LPFG/EFPI sensors. Sensor calibration and network architecture are discussed in great detail. In addition, commercial thermocouples and high temperature strain gauges are also deployed in the frame structure for performance comparison and system validation of the proposed optical sensor network. The proposed optical sensor network can provide insightful information on the development of inelastic deformations in the progressive failure process of the frame structure in a simulated harsh environment of post-earthquake fire conditions.

1.3.4. Temperature Dependent FEM Updating in Real Time. Along with the sensor validations is the development of a real-time prediction technique for structural behavior of the tested steel frame in the simulated harsh environments on the ABAQUS software platform. To ensure the accuracy in prediction of structural behavior, a

temperature-dependent FEM is updated in real time. A nonlinear baseline model of the one-story one-bay steel frame is established with three-dimensional (3-D) finite element analysis in ABAQUS. The structural nonlinearity in high temperature environments is taken into account by using temperature-dependent material properties specific to the steel material. A temperature-dependent optimization algorithm is developed to update the FEM analysis with the acquired strain and temperature data. The algorithm is validated with the steel frame tests in gradually increasing temperatures.

1.3.5. Progressive Collapse Evaluation of Steel Buildings with Hybrid Simulations. Based on the validated sensors and the FEM updating method, a hybrid simulation technique with multi-scale modeling is developed for real-world buildings. The hybrid simulation technique has a representative substructure fully instrumented for its actual behavior and the remaining substructure computationally simulated for its predicted behavior. In a hybrid simulation, a steel structure is divided into many groups, each having similar geometries and identical materials due to structural symmetry. For each group, the most critical structural member referred to as "master member" is modeled with fiber elements and the remaining members called "slave members" are modeled with beam and plates elements. The material behavior (stiffness and yielding stress) and service environments (temperature distribution) of the master member can be introduced to the modeling of slave members in real time, based on the premise that the latter can be related to the former in terms of construction process and the noise characteristics can be related to the structural damage under various external loads. An emphasis is placed on the development of a multi-scale modeling framework with environment characterization (noise and temperature), load determination, and structural resistance evaluation in real time. Towards this end, the master member is instrumented with an array of sensors for material property, temperature distribution, and structural behavior monitoring. The slave members are numerically simulated with a FEM established in ABAQUS. To verify and support the premise about member construction processes and noise attributes, finite element updating is performed to ensure that the interface between the master member and the slave members is compatible in terms of temperature, forces, and displacements under a predetermined evaluation criterion.

To demonstrate its implementation feasibility, the proposed hybrid simulation technique with multi-scale modeling is applied to a four-story two-bay steel building. The full-scale steel structure was tested on the 3-D shaking table located in Miki City, Hyogo Prefecture, Japan to study the effects of the 1995 Kobe earthquake [85]. The dynamic characteristics (e.g. natural frequencies) and structural responses (e.g. building displacements) from the hybrid simulation are compared to experimental results to validate the hybrid simulation technique in practical applications.

The validated hybrid simulations are then combined with model updating for both material and temperature effects on the responses of the four-story, two-bay steel structure. The progressive failure paths of the structure are then investigated and evaluated to understand the most critical failure condition for emergency rescue efforts during a post-earthquake fire event.

1.4. ORGANIZATION OF THIS DISSERTATION

This dissertation consists of seven chapters. Each main chapter (2-5) will be organized as a stand-alone paper including a detailed technical review section. Chapter 1 introduces the objectives and scope of work of this study, literature reviews on related topics such as optical fiber sensors and FEM updating, and five technical tasks that will be addressed in the following five chapters. Chapter 2 deals with the development and validation of large-strain sensors based on the EFPI principle. Chapter 3 discusses two methods for simultaneous large strain and high temperature measurement. Both analytical derivation and experimental validation for strain and temperature coefficients on the change in wavelength are presented. Chapter 4 deals with the development and application of an optical fiber network of LPFG, EFPI, and hybrid LPFG/EFPI sensors. Chapter 5 introduces a new model updating method based on the change in temperature. The temperature-dependent material properties are used in various FEM formulations. Chapter 6 presents a new hybrid simulation methodology with a micro-scale model of several critical components instrumented with a dense array of sensors and a macro-scale model of the remaining components simulated numerically. The main research outcomes, findings, and future studies are summarized in Chapter 7.

2. AN EFPI-BASED LARGE STRAIN SENSOR WITH ADJUSTABLE RESOLUTION

2.1. INTRODUCTION

Reinforced concrete and steel structures have been widely used in civil infrastructure due to their ductile behavior, extensive deformability, and competitive low cost. They are designed for service functionality under normal loads and for life safety under extreme loads associated with natural or man-made hazards. Under normal loads, structures often behave elastically and they are often subjected to a strain of less than 2,000 με. Under extreme loads, such as earthquakes and landslides, they exhibit inelastic behaviors and experience excessive deformation or strain in the order of 10,000 με to 100,000 με. To address the current need for the study of progressive collapse of structural systems under extreme loads, large strain measurements are of paramount importance. Such tasks become more complicated when considering the high resolution requirements for the functionality monitoring of structures under normal loads and for the understanding of structural behaviors. For example, at the critical strain levels related to the states of structural limit such as concrete cracking process and steel yielding process, a small change in the amount of strain could convey key information about the health condition of a structural system. Under these conditions, high resolution for strain measurements is highly desirable and a large strain sensor with adjustable strain resolution (lower resolution in regular locations and higher resolution in key locations) is preferred.

The development of large strain sensors has recently attracted worldwide attention. To this endeavor, the main challenge remains in producing strain measurements with both a large dynamic range and a degree of high resolution. Conventional strain sensors, such as electro-resistive strain gauges, have the desired resolution but possess a limited dynamic range of less than 15,000 με or 1.5%. For strains higher than 2%, extensometers, linear variable differential transformers [6], and grating based mark tracking techniques [7-9] are commonly used. With these methods, strain measurements up to 5% are expected but they suffer from low resolution of 4,500 με or 0.45%.

In the past two decades, fiber optic sensors have found many applications in structural health monitoring. In addition to their unique advantages such as compactness, immunity to electromagnetic interference, and real-time monitoring capability [13], fiber optic sensors are also known for their high resolution measurement of 2 με in the case of strain measurement. However, fiber optic sensors have a relatively small dynamic range due to the limited deformability of silica glass. For example, the break-strain for an uncoated fiber grating sensor is approximately 1%. To overcome this shortcoming, various coating techniques [55] and strain transfer mechanisms have recently been investigated [34, 56]. Their maximum strain (up to 2.4%) is still limited for the study of progressive collapse of structural systems under extreme loads. Another commonly used fiber optic sensor, the extrinsic Fabry-Perot interferometer (EFPI), also suffers from the limited strain dynamic range due to the use of a typical sensor structure design. Claus et al. (1992) [86] and Cibula et al. (2007) [87] reported EFPI sensors for strain and crack opening displacement measurements with a large temperature range. Although these particular sensors had an extremely high resolution of 1 με, they only functioned properly within a small dynamic range of 1%.

An EFPI sensor can be made by first inserting two cleaved optical fibers into a capillary tube. The two fibers are then bonded to the tube using either epoxy or thermo fusion. This packaging improves the sensor's robustness in applications, but limits the sensor's dynamic range to the corresponding maximum deformation of the capillary tube. On the other hand, if the two cleaved ends are left unattached to the tube, the packaged device is essentially a displacement sensor. By converting the measured displacement between the two cleaved ends to the corresponding strain, the device can be implemented as a large strain sensor. For example, if one or both ends of the fibers are adhered to a substructure to be monitored, as the substructure deforms under external loads, it will experience an applied strain that can be determined from the measured displacement signal by the EFPI. In this case, the technological challenge remains in achieving high resolution during a large strain measurement. The concept of the movable EFPI sensor was developed in 1994 [57] and it had also been applied in the investigation of the strain measurements during the first few hours of the hydration reaction of concrete embedded packaging structures [58-60]. However, most applications of the movable EFPI sensors

involved small strain ranges, and the sensor's resolution have not yet been systemically analyzed. Since optical fiber EFPI sensors have been widely applied to structural health monitoring for more than twenty years, several data processing methods have been investigated [88, 89]. In most cases, the strain measurement ranges of the EFPI sensors have been small and phase tracking method with relatively high resolution has been widely applied. Qi et al. (2003) developed a hybrid data processing method by combining multiple methods using a white light interferometer [89]. Although the tested EFPI strain sensors were only able to function over a small dynamic range, the development of this novel data processing method made it possible to obtain both a larger dynamic range and a higher resolution in subsequent device.

More recently, intensity-based plastic optical fiber (POF) sensors have been reported to successfully monitor strains as high as 40% or more [90-95]. Among the various sensor developments, one attractive operating principle for large strain monitoring has been based on the displacement measurement between two cleaved fiber surfaces housed within a tube. With the two ends of a POF sensor free to move under an applied axial load, the sensor's strain measurement range was not limited by the yield strain of the POF material. However, these plastic fiber sensors were mostly intensity-based, which resulted in a decreased resolution. In addition, plastic optical fibers revealed a strong thermo-optic coupling with a high thermal expansion coefficient, resulting in a large temperature-strain cross sensitivity. The strong coupling limited their applications to lower temperature ranges than glass optical fibers.

In this chapter, a new design for an EFPI-based glass fiber optic sensor for large strain measurements with adjustable resolution is proposed. Three data processing methods, including interference frequency tracking, period tracking, and phase tracking, are studied and integrated to achieve adjustable strain resolution from 10 με to 6,000 με within a ±12% dynamic range. The proposed sensor design can be applied to monitor the health condition of building structures and alert building tenants of any dangerous situations during disastrous events such as earthquakes and fires.

2.2. PRINCIPLES OF OPERATION

2.2.1. Sensor Structure and Signal Interrogation System. Figure 2.1 shows the schematic of a fiber optic EFPI sensor structure and the associated signal interrogation system. The EFPI is formed by two perpendicularly cleaved end faces of a single-mode optical fiber (Corning SMF-28). One side (the left side in Figure 2.1) of the fiber serves as a lead-in fiber and the other side (the right side in Figure 2.1) serves as a low reflective mirror that is illustrated by the enlarged view of the sensor head in Figure 2.1 (a).

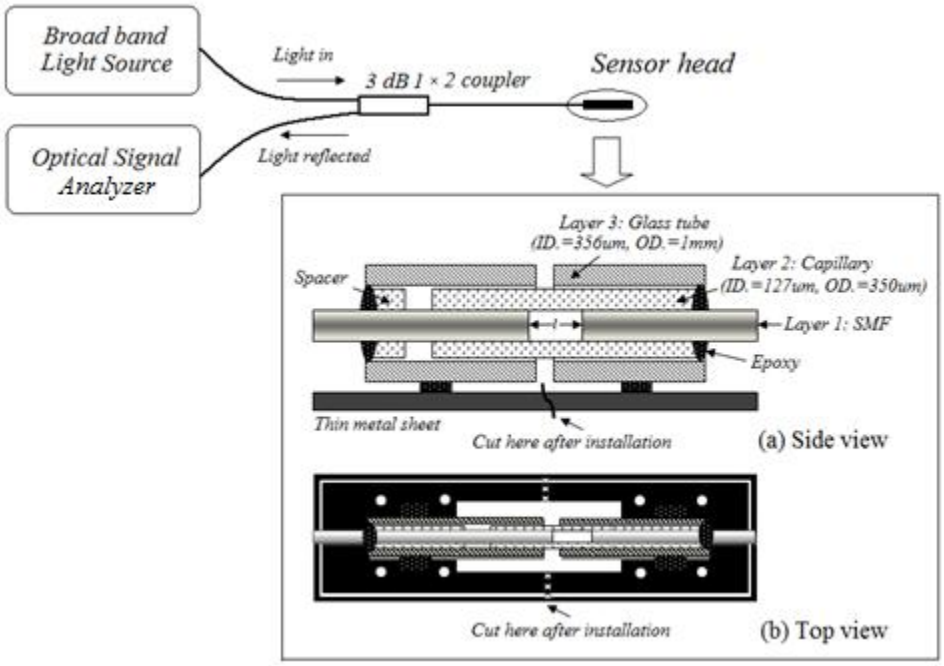

Figure 2.1 Schematic of a fiber optic EFPI: sensor structure and signal interrogation system

In theory, a Fabry-Perot cavity with a freely movable end face can be constructed by inserting two cleaved fiber ends into the two ends of a glass tube and gluing one side of the bare fiber to the tube. However, the freely movable bare fiber ends, when not glued to the capillary, are easy to break in applications since optical fibers are susceptible to any shear force or action. To solve this problem, a three layer structure is used to package the strain sensor, including the core, intermediate layer and outmost layer. The core layer (layer 1 in Figure 2.1) is an optical glass fiber of 125 μm in diameter. The intermediate layer (layer 2 in Figure 2.1) is a capillary glass tube with an inner diameter of 127 μm

and an outer diameter of 350 μm. The capillary tube is designed to guide the cleaved fiber to ensure that its two end faces can move in parallel. The outmost layer (layer 3 in Figure 2.1) is a glass tube with an inner diameter of 356 μm and an outer diameter of 1,000 μm, which is designed to enhance the overall stability of the packaged sensor. On one side (right) of the interferometer, all three layers are bonded together with epoxy as illustrated in Figure 2.1 (a). On the other side (left), the fiber is bonded to the third layer through an inserted spacer while the intermediate layer is unbounded to allow for free movement of the fiber end faces within the capillary tube. The three-layer structure transfers the shear force from the bare fiber to the intermediate layer (spacer) during operation. With a larger diameter, the intermediate layer is less susceptible to any applied shear force, so that the proposed structure can operate steadily without breakage. The two pieces of the outside glass tube are bonded to a thin metal sheet at both the lead-in side and mirror side of the fiber sensor, which in turn can be bolted to a steel substructure in applications. As indicated in Figures 2.1 (a, b), the sensor installation is completed by cutting the thin metal attachment sheet, which has a precut rectangular hole through the middle section and two perforated side strips. The resulting separation of two attachment sheets ensures that the sensor actually measures the elongation of the steel substructure between the two attachment points, as clearly illustrated in the side view of Figure 2.1 (a) and the top view of Figure 2.1 (b). The distance between the two inner bolts is defined as the gauge length of the sensor, which is L = 2mm (0.08 in.) in this study. The EFPI cavity length is designated as l.

As shown in the signal interrogation system of Figure 2.1, a broadband light source (BBS) ranging from 1520 nm to 1620 nm is generated by multiplexing a C-band (BBS 1550A-TS) and an L-band (HWT-BS-L-P-FC/UPC-B) Erbium Doped fiber amplified spontaneous emission (ASE). The light propagates into the EFPI sensor through a 3 dB coupler. As light travels through the lead-in fiber, part of the light is reflected at both cleaved end faces of the EFPI sensor, producing a backward travelling interference signal. The reflected interference spectrum coupled back by the coupler is detected by an optical spectrum analyzer (OSA, HP 70952B). A personal computer is used to record and process the interference spectra. Finally, the characteristic wavelength

on the spectra is related to the cavity of the EFPI, which results in a representation of the strain applied to the substructure.

Based on the proposed sensor structure, a sensor prototype was fabricated as shown in Figure 2.2 (a). The micro-view of its sensor head can be seen in Figure 2.2 (b).

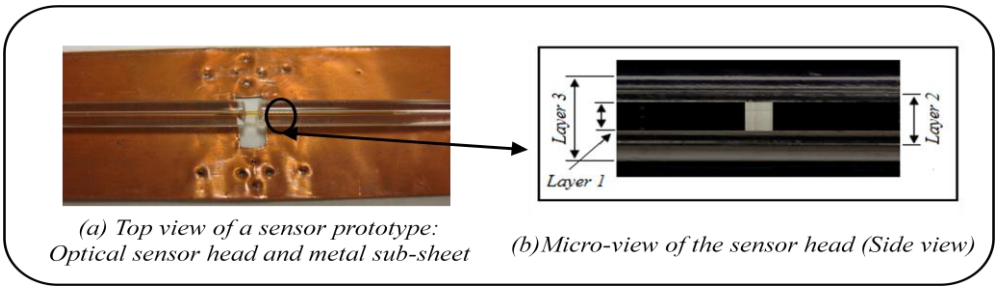

Figure 2.2 Sensor prototype

2.2.2. Signal Processing Algorithms. To simultaneously achieve a large dynamic range and high resolution in strain measurements, three data processing methods are introduced and studied to characterize their performance. These methods include 1) interference frequency tracking of the Fourier transform of a spectral interferogram, 2) period tracking and 3) phase tracking of the spectral interferogram.

2.2.2.1. Interference frequency tracking method. A low finesse EFPI can generally be modeled by a two-beam interference theory [96]. The spectral interferogram of an EFPI typically represents a harmonic function of wavenumber with a dominant frequency known as the interference frequency. By taking the Fourier transform of such an interferogram, an approximate delta function of cavity length corresponding to the interference frequency is obtained [88]. The cavity length of the EFPI, *l*, can be calculated by Eq. (1):

$$l = \frac{n\pi}{\left(v_E - v_S\right)} \tag{1}$$

in which v_S and v_E are the wavenumbers of the starting and ending points of an observation bandwidth, respectively, and n is an integer representing the Fourier series index.

It can easily be observed from Eq. (1) that the minimum detectable cavity length change of an EFPI large strain sensor is $\pi/(v_E - v_S)$ when n=1. For a light source with a spectrum width of 100 nm, the detectable cavity length change is approximately 12 μm. This corresponds to strain resolution of approximately 6,000 με when a gauge length of 2 mm is used. As indicated by Eq. (1), the strain resolution is inversely proportional to the bandwidth of the light source. Higher resolution in strain measurement thus requires an optical source with a broader bandwidth, which can only be provided by a limited selection of equipment available in the market.

2.2.2.2. Period tracking method. Due to the interrelation between period and interference frequency, the change in period of the spectral interferogram can also be used to determine the cavity length of an EFPI [96]. The period of a spectral interferogram is defined as the distance between two consecutive valleys on the spectral interferogram. By introducing a wavenumber-wavelength relation ($\nu = 2\pi/\lambda$), the cavity length can be evaluated through Eq. (2):

$$l = \frac{\lambda_1 \lambda_2}{2(\lambda_2 - \lambda_1)} \tag{2}$$

where λ_1 and λ_2 ($\lambda_2 > \lambda_1$) represent the first and second wavelengths of two consecutive valleys on the spectral interferogram that can be directly taken from OSA measurements.

Let S_l be the resolution of a strain sensor, which is defined as the minimum detectable change in cavity length when using the period tracing method. Therefore, when λ_1 and λ_2 are assumed to be two independent random variables, S_l can be derived from Eq. (2) and expressed as Eq. (3):

$$S_l = \sqrt{(\frac{\partial l}{\partial \lambda_1})^2 (S_{\lambda_1})^2 + (\frac{\partial l}{\partial \lambda_2})^2 (S_{\lambda_2})^2} = \sqrt{\frac{{\lambda_1}^4}{4(\lambda_2 - \lambda_1)^4}(S_{\lambda_1})^2 + \frac{{\lambda_2}^4}{4(\lambda_2 - \lambda_1)^4}(S_{\lambda 2})^2} \tag{3}$$

in which $S_{\lambda 1}$ and $S_{\lambda 2}$ represent the OSA measurement resolutions of the two consecutive valleys, respectively. Determined from the performance specifications of a particular

OSA instrument, $S_{\lambda 1}$ and $S_{\lambda 2}$ are equal ($S_{\lambda 1}=S_{\lambda 2}=S_{\lambda}$) since the instrument has a consistent measurement resolution of wavelength within the specified observation bandwidth. In addition, within a relatively small observation spectrum range, both λ_1 and λ_2 can be approximated by the center wavelength of the range, λ_0. As a result, Eq. (3) can be simplified into,

$$S_l \approx S_\lambda \frac{{\lambda_0}^2}{\sqrt{2}(\Delta\lambda)^2} \tag{4}$$

where $\Delta\lambda$ is the wavelength difference between the two consecutive valleys. For the estimation of measurement errors, $\Delta\lambda$ at a given cavity length can be considered to be a constant within the wavelength bandwidth of observation, though $\Delta\lambda$ does increase with wavelength. Eq. (2) and Eq. (4) indicate that the minimum detectable cavity length decreases quadratically with cavity length as $\Delta\lambda$ decreases, resulting in a lower resolution as cavity length increases.

2.2.2.3. Phase tracking method. Based on the two beam interference theory [96], the spectral interferogram reaches its minimum when the phase difference between the two beams satisfies the following condition:

$$\frac{4\pi l}{\lambda_v} = (2m+1)\pi \tag{5}$$

where m is an integer that can be estimated following the procedure as specified in [16], and λ_v is the center wavelength of a specific interference valley. Taking the derivative of the cavity length (l) with respect to λ_v yields

$$\frac{dl}{d\lambda} = \frac{2m+1}{4} \tag{6}$$

Therefore, the change in cavity length can be estimated from Eq. (5) and Eq. (6) as follows:

$$\Delta l = \frac{\Delta \lambda_v}{\lambda_v} l \tag{7}$$

where $\Delta\lambda_v$ is the change in center wavelength of the specific interference valley and Δl is the change in cavity length. As Eq. (7) indicates, the cavity length change is directly proportional to the wavelength shift of the interferogram and to the cavity length of the EFPI. Since the minimum $\Delta\lambda_v$ is represented by the instrument measurement resolution or $S_{\lambda 1}$ and $S_{\lambda 2}$, the resolution of the phase tracking method decreases linearly as the EFPI cavity length increases.

2.2.2.4. Comparison among three processing methods. Figure 2.3 compares the theoretical strain measurement resolutions of three data processing methods when L= 2mm (0.08 in.). To account for the variation in wavelength measurement resolution of different OSA's, assume $S_\lambda = \Delta\lambda_v$ equal to 0.001 nm, 0.01 nm, and 0.1 nm for comparison. It can be clearly observed from Figure 2.3 that the interference frequency tracking method has constant resolution of approximately 6,000 με. The resolution of the period tracking method decreases quadratically as the EFPI cavity length increases. The resolution of the period tracking method is also strongly influenced by the resolution of the OSA system. If $S_\lambda = \Delta\lambda_v = 0.01$ nm, the strain resolution of period tracking method is 600 με. If $S_\lambda = \Delta\lambda_v = 0.1$ nm, the period tracking method has a higher resolution than the interference frequency tracking method for $l < 320$ μm. In addition, the resolution of the phase tracking method decreases linearly as the EFPI cavity length increases. Among the three methods, the phase tracking method has the highest resolution since it represents the local (most detailed information) change of phase. When $l = 320$ μm and the given OSA resolution is 0.1 nm, the strain resolution of the phase tracking method is 10 με in comparison with 6,000 με for the other two methods. However, the phase tracking method can only measure a relatively small change of the cavity length within a 2π phase range to avoid ambiguity. Therefore, its operation range is limited to a change of approximately 0.75 μm in cavity length or a change of 375 με in strain. On the other hand, the other two methods can be used to measure a large change of cavity length.

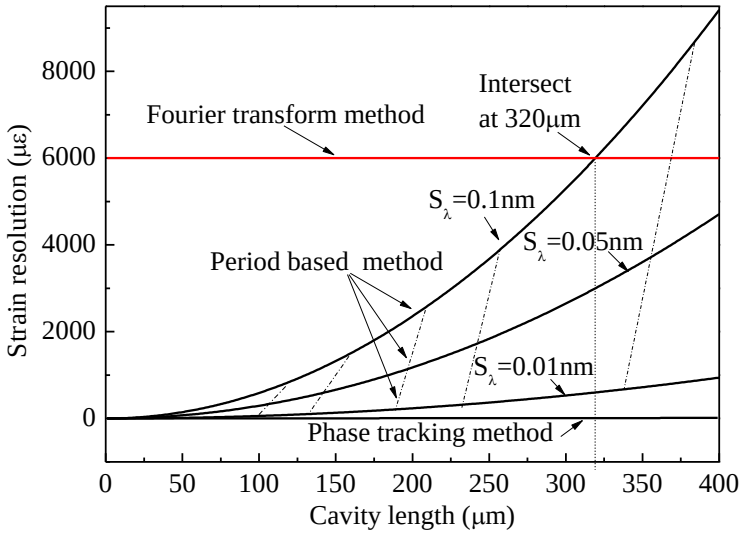

Figure 2.3 Resolution as a function of cavity length

2.3. EXPERIMENTS AND DISCUSSION

To evaluate the performance of the proposed sensor for large strain measurements, an EFPI-based prototype sensor was constructed with transparent glass tubes so that any change in cavity length can be observed in the laboratory by using an optical microscope as shown in Figure 2.2 (b). The lead-in side of the fiber sensor was fixed on an aluminum block and the fiber mirror side of the sensor was attached to a computer-controlled precision stage so that the cavity length could be precisely controlled. The gauge length of the strain sensor was set to 2mm (0.787 in.). The reference strain, which will be further discussed later, was determined by dividing the change in cavity length, directly measured by stage movement, by the gauge length. The strain detected by the EFPI sensor is obtained by dividing the cavity length calculated from an EFPI signal to the gauge length.

Figure 2.4 (a) presents two interferograms of the EFPI sensor prototype with a cavity length of 65 μm and 175 μm, respectively. It can be observed from Figure 2.4 (a) that the interference frequency increases as the EFPI cavity length increases or as more fringes are condensed into a given observation spectrum range. However, the range of interference signal intensities decreases as the EFPI cavity length increases. The signal range is often quantified by a fringe visibility (V) as defined by Eq. (8),

$$V = \frac{I_{max} - I_{min}}{I_{max} + I_{min}} \tag{8}$$

where I_{max} and I_{min} represent the maximum and minimum intensities of an interference signal, respectively. The fringe visibility determined from Eq. (8) is plotted in Figure 2.4 (b) as a function of cavity length. The experiment stopped when the fringe visibility dropped below 20%, corresponding to a maximum cavity length of approximately 265 μm of the prototype sensor. The drop in fringe visibility as a function of cavity length was mainly caused by the divergence of the output beam from the lead-in fiber, which was governed by the numerical aperture (NA) of the fiber [97]. Other potential factors such as misalignment are negligible in this study since the glass tubes of the three-layer sensor prototype were assembled with a tight tolerance.

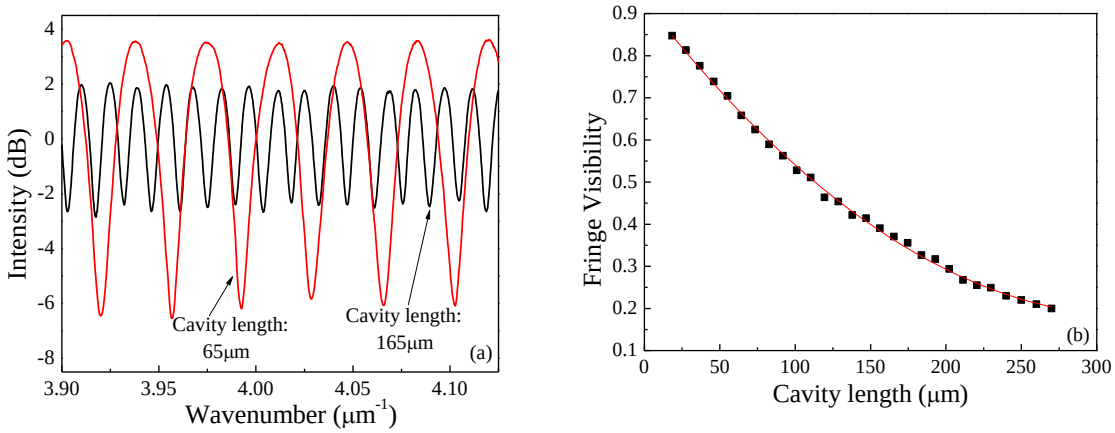

Figure 2.4 Characteristics of an EFPI sensor: (a) interferograms with a cavity length of 65 μm and 175 μm and (b) fringe visibility as a function of cavity length

To investigate the measurement resolution of the interference frequency tracking method, large strain measurement experiments were designed and operated. During various tests, the cavity length of the sensor prototype ranged from 15 μm to 265 μm at 10 μm intervals. The maximum change of cavity length was approximately 250 μm, corresponding to a dynamic strain range of 12%. Figure 2.5 relates the reference strain measured by the change in stage movement to the strain measured by the change in cavity length of the EFPI sensor. The theoretic values were directly calculated based on

the stage movement; they follow a straight line with a slope of 1:1 as represented by the solid line in Figure 2.5. The experimental data points demonstrated only slightly fluctuations with respect to the theoretic line. To compare the measurement resolutions of the interference frequency tracking method and the period tracking method, refined experiments were conducted within a strain range of 11,000 με to 21,000 με. In this case, the precision stage was moved at 2 μm intervals, giving rise to a strain change of 1,000 με between two consecutive measurements. The results from the refined experiments processed with both the interference frequency tracking and period tracking methods are presented as an inset in Figure 2.5. It can be seen from Figure 2.5 that the theoretical prediction strongly agrees with the test data points that were processed with the period tracking method and the measured strains processed with the interference frequency tracking method follow a zig-zag trend with respect to the theoretic prediction. This comparison indicates that the interference frequency tracking method is unable to resolve a strain difference within an interval of 12 μm in cavity length. This length resolution corresponds to a strain measurement of approximately 6,000 με, which agrees with the calculated strain resolution that is limited by the light source bandwidth of 100 nm.

The relative accuracy between the interference frequency method and period tracking method is supported by Figure 2.3 since the cavity length observed during the refined experiments was significantly less than 320 μm when the two methods had the same resolution. The interference frequency tracking method is advantageous over the other two methods in terms of computational efficiency and constant resolution over the entire dynamic range. In addition, it is immune to localized spectrum distortions that could potentially result in large errors when waveform based signal processing methods are used.

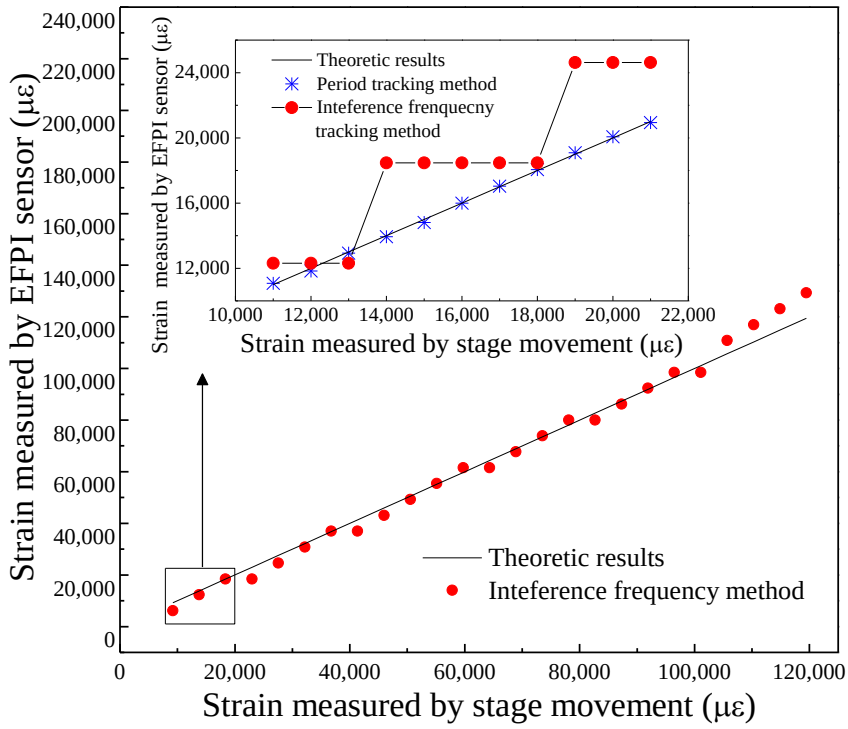

Figure 2.5 Measured stains processed with the interference frequency tracking method (Inset: comparison between the frequency and period tracking methods)

To verify the accuracy of the phase tracking method, more refined experiments were performed with a smaller stage movement interval of 0.1 μm. The cavity length of the EFPI sensor was set to range from 15 μm to 30 μm, which corresponded to a strain of 7,500 με. Figure 2.6 (a) shows two representative spectral interferograms of the EFPI sensor at two consecutive stage positions with a cavity length difference of 0.1 μm. Figure 2.6 (b) compares the measured strains processed with the phase tracking and the period tracking methods. It can be observed from Figure 2.6 (b) that the theoretically predicted strain is in agreement with the strain data points processed with the phase tracking method and that of the period tracking method shows notable deviations from the theoretic prediction based on the reference strains. This comparison indicates that refined resolution can be achieved with the use of the phase tracking method. The maximum deviation of the period tracking method was estimated to be 50 με at an EFPI cavity length of 30 μm, which is consistent with the theoretic prediction given in Figure 2.3. The deviation is expected to a further increase as the EFPI cavity length increases. However, it is worth noting that the period tracking method can measure a large range of

strain while the phase tracking method is limited to a strain measurement range of approximately 375 με, which corresponds to a phase shift of 2π.

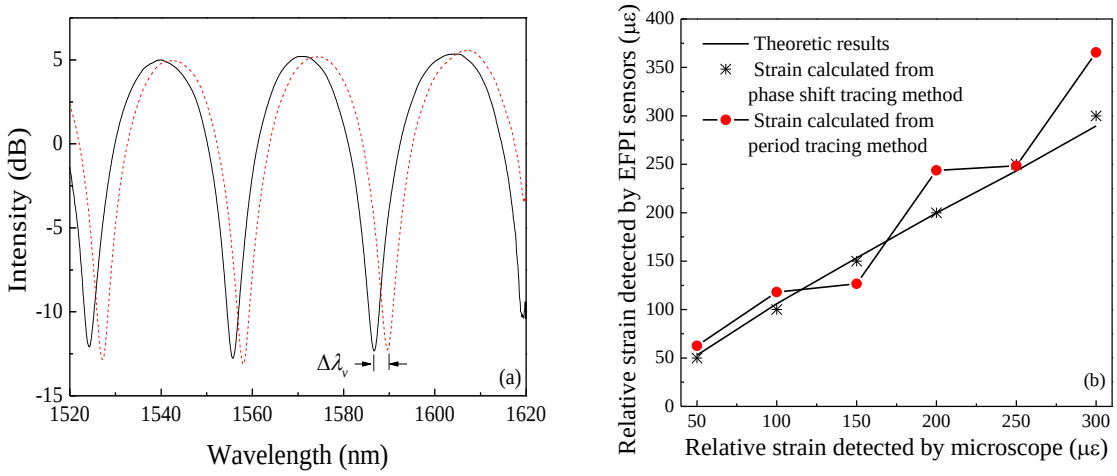

Figure 2.6 Phase tracking method: (a) typical spectral interferograms and (b) comparison with the period tracking method

2.4. SELECTION CRITERIA OF STRAIN RESOLUTION

For structural health monitoring with a wide range of strain measurements, for example, 10% or higher, a reasonable value of strain resolution must be selected accordingly or adjustable strain resolution is required at multiple strain levels. Therefore, selection criteria for strain resolution need to be developed to correspond to various large strain measurements. In this study, the proposed movable EFPI large strain sensor is considered for the development of selection criteria for strain resolution. Based on the previous experimental experiences, the recommended selection criteria are given in Table 2.1. Here, IFT represents the interference frequency tracking method, PET represents the period tracking method, and PHT represents the phase tracking method. When a strain measurement ε is less than 6,000 με that is approximately three times as high as the yielding strain of Grade 60 steel, and the strain change rate is relatively high, the strain resolution is required to be as low as of 10 με. In this case, it is recommended that the PET and PHT methods be combined to achieve the required strain resolution with the proposed optical fiber sensor. As a strain measurement increases from 6,000 to 20,000

με, which still yields a relatively high strain change rate, strain resolution of as low as 100 με is recommended and the PET method can meet the requirement. When a strain measurement ranges between 20,000 and 50,000 με, the strain change rate is relatively low. In this case, the strain resolution can be increased to 1,000 με and the PET and IFT methods must be combined to provide the required resolution. If a strain measurement increases to over 50,000 με and the strain rate is further reduced, the required strain resolution can be as high as 6,000 με with the IFT data processing method. With the proposed three data processing methods, an optical fiber sensor with adjustable strain resolution can be achieved for strain measurements as large as 120,000 με or 12%.

Table 2.1 Selection criteria for strain resolution

Strain Level (με)	Strain Resolution (με)	Data Processing Methods
$\leq 6{,}000$	10	Combined PET & PHT
$6{,}000 < \varepsilon \leq 20{,}000$	100	PET
$20{,}000 < \varepsilon \leq 50{,}000$	1,000	Combined PET & IFT
>50,000	6,000	IFT

2.5. SUMMARY ABOUT EFPI-BASED SENSOR PROPERTIES

In this chapter, a fiber optic EFPI strain sensor with adjustable strain resolution has been proposed for large strain measurement. The proposed sensor has a large dynamic range of up to 120,000 με or 12%. The well designed three layer structure of the sensor prototype does not only prevent any misalignment between the two end faces of the EFPI but also makes it easy to install and robust to survive various application environments. Three data processing methods, including the interference frequency tracking method, period tracking method, and phase tracking method, have been applied and investigated. The interference frequency tracking method has constant strain resolution of 6,000 με. The period tracking method provides a quadratic decrease in strain resolution as the cavity length increases, reaching 6,000 με at a cavity length of 320 μm with 0.1 nm OSA resolution. The phase tracking method is the most accurate among the three methods; its strain resolution linearly decreases as the EFPI cavity length

increases. At an EFPI cavity length of 320 μm, the strain resolution of the phase tracking method is less than 10 με, given 0.1 nm OSA measurement resolution.

When the three data processing methods are used together to compensate each other, the proposed optical fiber sensor can achieve adjustable strain resolution from 10 με at strategically important locations and 6,000 με for the other locations of a steel structure. As the strain resolution improves from the use of an interference frequency tracking to the phase tracking method, the computational efficiency decreases. The interference frequency tracking method is also superior to the other two methods in that it has constant resolution over the entire dynamic range and is immune to any potential localized spectrum distortion. The interference frequency tracking method and the period tracking method can be used to measure a full range of large strains while the phase tracking method is limited to a specific strain range, i.e., 375 με in this study, which corresponds to a phase shift of 2π. However, by combining the three data processing methods, the proposed sensor can be used in various structural applications to measure large strains with adjustable resolution.

3. SIMULTANEOUS LARGE STRAIN AND HIGH TEMPERATURE MEASUREMENTS WITH OPTICAL FIBER SENSORS

3.1. INTRODUCTION

Buildings are exposed to increasing fire hazards during recent extreme events such as earthquake-induced gasoline ruptures and terrorist threats. In combustion science, three typical types of fire flames exist, including jet fires, pre-mixed flames, and diffuse flames. Jet fires mix the fuel and the oxidant with stoichiometrical proportions. The mixture is followed to be ignited in a chamber with a constant volume. Without capability for expansion in the chamber, the fire flow is driven out from the chamber with a high velocity, which is the case for most jet engines. With such a high speed of fire flow, large amount of heat is generated by the jet fires. For the pre-mixed flames, the same mixture is used as for jet fires and the mixture is ignited when it goes out from a nozzle with a constant pressure. In this case, the pre-mixed fire, for example, produced by oxyacetylene torch or a Bunsen burner does not have a velocity of heat flow as a jet fire did. A diffuse flame, though, does not mix the fuel and the oxidant before ignition. The fuel and oxidant flow together without pre-control and ignite as long as the fuel/oxidant ratio reaches the flammable range, for instance, fire flame in air, as was the WTC fire [1, 97-98]. Among these three fire flame types, although a diffuse flame generates the lowest heat intensity, it is the most important type of flames for structural fire from the view of civil engineers' consideration.

For fire flames, different maximum flame temperatures will be yielded by using various fuel sources. For example, most commonly, the adiabatic combustion temperatures are around 2,200 ℃ (3,992 ℉) for coals, around 2,150 ℃ (3,902 ℉) for oil, and 2,000 ℃ (3,632 ℉) for natural gas. However, the maximum flame temperature is seldom achieved in common conditions because air is used rather than pure oxygen, which will reduce the temperature of the flame at least by two-thirds. The reason for the occurrence of this phenomenon is that to form a molecule of carbon monoxide and a molecule of water, every oxygen molecule releases a small amount of heat. If the pure oxygen is used, only two molecules (carbon monoxide and water) are needed to be heated up; but if the air is used instead, in addition to the two molecules, four molecules of

nitrogen must also be heated. Considering that three times as many molecules must be heated when air is used, fires in air produces only one-third the temperature increase as in pure oxygen. Thus, the maximum flame temperature for fire induced by jet fuel in air is about 1,000 ℃ (1832 ℉) [98].

In addition, for the diffuse flame, which is the most important fire flame in structural fires, it is even more difficult to reach the maximum flame temperature, because the fuel and the air in a diffuse flame are hard to be seen as mixed at the best ratio. In most cases, diffuse flames are rich in fuel, which can drop the temperature twice down again. Thus, the temperatures in a residential fire are usually in a range from 500 ℃ (932 ℉) to 650 ℃ (1202 ℉) [98]. For example, in reference to the collapse investigation of the former World Trade Center towers [97], none of the steel samples recovered from ground zero showed evidence of exposure to temperatures above 600 ℃ (1112 ℉) for as long as 15 minutes. Only three of the recovered samples of exterior panels reached temperatures in excess of 250 ℃ (482 ℉) during the fire or after the collapse. Therefore, a temperature range of up to 700 ℃ (1292 ℉) seems appropriate for building research in fire environments.

For steel, its material properties can be significantly changed at evaluated temperatures. With respect to ambient temperature, the yield strength of steel is reduced to 23% at 700 ℃ (1292 ℉), 11% at 800 ℃ (1472 ℉), and 6% at 900 ℃ (1652 ℉) [1]. In these harsh environments, some of steel components may fail due to their susceptibility to buckling under gravity loads, leading to the progressive collapse of entire structures. Therefore, the behavior of steel buildings in a high temperature environment (e.g. progressive collapse of steel buildings) has thus become a fundamentally important subject that will continue to receive growing interests in the research community. To the best of our knowledge, sensors are presently unavailable for deployment in fire environments even for laboratory experiments. For example, to understand the fundamental physics involved in a fire-structure interaction process, two insulated steel trusses were tested in jet fuel fires [97]. However, no sensor was actually instrumented on the structural members to directly measure temperature and strain inside fire flames, though having these parameters was highly desirable. The fire-structure interaction would

never be fully understood without sensors that can directly measure large strains at high temperature.

Strain measurements at high temperature have been attempted by several researchers with fiber Bragg grating (FBG) sensors [51, 52] and Fabry-Perot (F-P) sensors [53, 54]. For simultaneous strain and temperature measurements, long period fiber grating (LPFG) sensors fabricated with a birefringence fiber [99] and compact LPFG pairs [100] have been investigated. Due to limited deformability of the optical fiber, these sensors can only sustain a strain of less than 4,000 με. Han et al. [101] reported that a dual-LPFGs sensing system with a cladding mode stripper in between can simultaneously measure temperature up to 180 °C (356 °F) and strain up to 8,000 με. However, the weak stripper between the two LPFGs limits the temperature range of the dual sensor within 200 ℃ (392 ℉). Rao et al. [102] presented a hybrid LPFG/micro extrinsic Fabry-Perot interferometric (EFPI) sensor for a simultaneous measurement of strain and temperature up to 650 ℃ (1202 ℉). However, its strain dynamic range is very small.

In an effort to simultaneously measure large strain and high temperature information for structural health monitoring in harsh environments, two types of optical fiber sensors are developed in this chapter. Since the CO_2 laser induced LPFG sensors are generally sensitive to temperature, the first attempt is given to a single LPFG for simultaneous large strain and high temperature measurements. Since the bare fiber (LPFG) is easy to break, the dynamic range of strain measurements is less than 4,000 με. To increase the strain sensing capability of LPFG sensors, a strain transfer mechanism by using the elasticity of adhesive layers between the sensor and the host structure and a gauge length change mechanism are introduced. On the other hand, a hybrid LPFG/movable EFPI sensor is also investigated, considering that the movable EFPI sensor can measure a large displacement between two sides of the cavity. A hybrid sensor combines the LPFG sensor and the movable EFPI sensor proposed in Chapter 2. The LPFG component is used to monitor the temperature change in a large temperature variation range, and the movable EFPI sensor is applied to sense the strain change with adjustable strain resolution in a relatively large strain dynamic range.

3.2. A TEMPERATURE SELF-COMPENSATED LPFG SENSOR

The first long period grating was successfully inscribed on an optical fiber in 1996 [28] and the modulation of a relative effective index change between the core and cladding of a LPFG sensor can be achieved by UV irradiation [30] and CO_2 laser irradiation [31]. With different fabrication methods, LPFG sensors have different properties for strain and temperature measurements. The strain and temperature properties of UV-induced LPFG sensors have been widely investigated in the past few years. UV-induced LPFG strain sensors largely depend on the types of fibers due to their diverse strain-optic coefficients [32]. They exhibited positive strain sensitivity and negative temperature sensitivity with cladding modes lower than LP_{11} [31, 32]. On the other hand, the properties of LPFG sensors induced by CO_2 lasers have not been investigated systematically. The effects of various interrelated physical parameters such as strain and temperature on the sensitivity of LPFG sensors remain unclear in various applications.

The objectives of this study are to design, fabricate, and characterize a CO_2 laser-induced LPFG optic sensor that is packaged with a strain transfer mechanism for large strain measurements at high temperature, and to develop a simultaneous strain and temperature evaluation methodology by using two cladding modes (LP_{06} and LP_{07}) of a single LPFG sensor. The new evaluation methodology does not need a secondary optical fiber sensor for temperature compensation as required by many existing technologies, in which cases a small temperature difference between the se2ondary fiber sensor and the LPFG sensor could result in a significant error in strain measurements. Both strain and temperature sensitivities of the LPFG sensor as well as the efficiency of the strain transfer mechanism are analytically derived and validated with tension tests at elevated temperatures.

3.2.1. Operational Principle and Strain/Temperature Demodulation.

3.2.1.1. CO_2 laser induced LPFG sensor. A schematic view and prototype photo of the CO_2 laser based LPFG fabrication system is presented in Figure 3.1 (a, b). A CO_2 laser (SYNRAD, Inc.) with a free space wavelength of 10.6 μm and a maximum output power of 20 W was used in this study and controlled by the computer through the

laser controller to produce a desired power. The optical fiber (Corning SMF-28) with its buffer stripped is placed on a three-dimensional (3-D) motorized translation stage controlled by a computer, providing a consistent displacement of the translation stage so that the fiber can be precisely moved to the center of the laser beam. The focused laser beam was transversely loaded onto the single mode optical fiber. Controlled by a computer, the translation stage moved the fiber at fixed step for laser exposure, resulting in a periodic refractive index modulation in the fiber core. A microscope video camera was used to visualize the micro-displacement of the optical fiber while the fabrication process is activated. During grating fabrication, a tunable laser (HP81642A) and an optical power meter (HP 81618A) were also used to monitor the grating transmission spectrum [102].

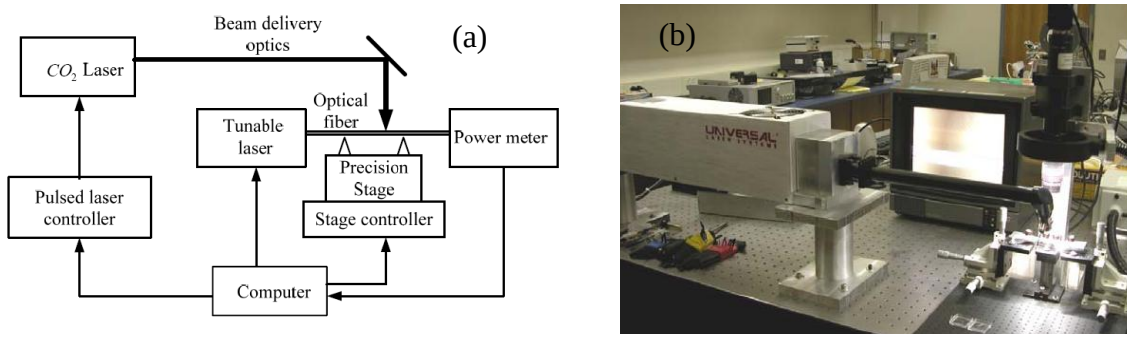

Figure 3.1 LPFG fabrication: (a) a CO_2 laser system and (b) processing units

At a cross section of most single mode optical fibers, a step-profile refractive index can be assumed. To retain the light waveguide property, the refractive index of the core mode must be larger than that of every cladding mode. Since the light waveguide only propagates in the core mode along a certain path LP_{01}, the ray undergoes a total internal reflection at the core-cladding interface and no coupling between the core mode and the cladding mode is observed at an unmodified single mode fiber, as showed in Figure 3.2 (a) outside the grating area. However, during the fabrication process of gratings, some residual stress remains inside the fiber and affects the refractive index of the single mode fiber [103, 104]. Associated with the CO_2 irradiation, the mean values of the effective refractive index change of the core and the cladding mode LP_{0m} can be respectively expressed into:

$$\delta\bar{n}_{eff,co} = s_0\zeta_{co},\ \delta\bar{n}_{eff,cl,m} = s_0\zeta_{cl,m} \tag{9}$$

in which $\delta\bar{n}_{eff,co}$ and $\delta\bar{n}_{eff,cl,m}$ represent effective index changes of the core and cladding mode LP_{0m}, respectively; s_0 is the DC modulation coefficient and it was determined to be approximately -3×10^{-4}; ζ_{co} and $\zeta_{cl,m}$ are the self-coupling coefficients of the core and cladding mode LP_{0m}, respectively [105, 106]. Thus, the transmission spectrum of the LPFG shows various dips for multiple cladding modes LP_{0m} as seen in Figure 3.2 (b) for a LPFG with 5 different cladding modes displayed in a wavelength range of 800nm.

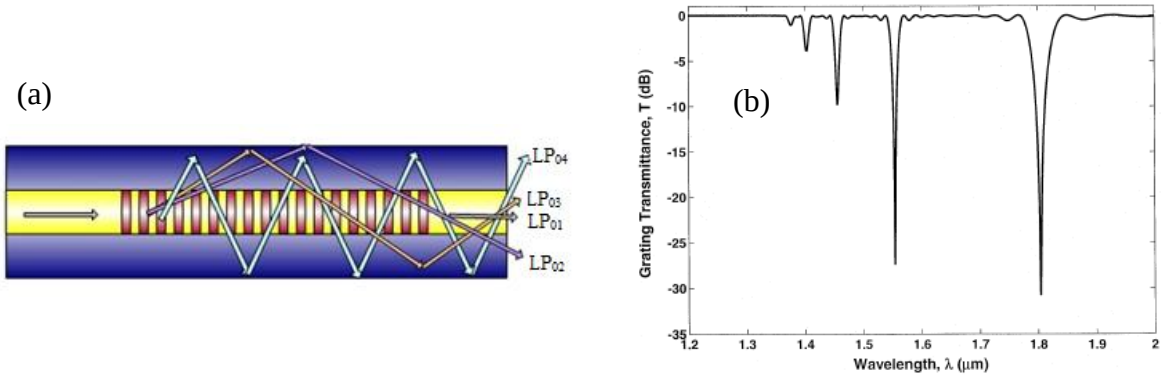

Figure 3.2 CO_2 laser-induced LPFG: (a) core and cladding modes and (b) transmission spectra

3.2.1.2. Theoretic analysis of temperature sensitivity. The resonant wavelength ($\lambda_{D,m}$) of a LPFG sensor can generally be expressed as a linear function of its grating period (Λ) and effective refractive indices of the core ($n_{eff,co}$) and the cladding mode LP_{0m} ($n_{eff,cl,m}$) as follows [32]:

$$\lambda_{D,m} = (n_{eff,co} - n_{eff,cl,m})\Lambda \tag{10}$$

Taking into account the induced DC effective refractive index change ($\delta\overline{n}_{eff,co}$ and $\delta\overline{n}_{eff,cl,m}$) as shown in Eq. (10), the resonant wavelength ($\lambda_{re,m}$) can, therefore, be expressed into:

$$\lambda_{re,m} = [(n_{eff,co} + \delta\overline{n}_{eff,co}) - (n_{eff,cl,m} + \delta\overline{n}_{eff,cl,m})]\Lambda \tag{11}$$

Eq. (11) can be related to Eq. (10) by [107]:

$$\lambda_{re,m} = \lambda_{D,m}(1 + \frac{\gamma_m \, \delta\overline{n}_{cm}}{n_{eff,co} - n_{eff,cl,m}}) \tag{12}$$

after the fiber waveguide refractive coefficient and the relative change of average effective refractive indices between the core and cladding mode LP_{0m} are respectively defined by:

$$\gamma_m = \frac{d\lambda_{D,m} / d\Lambda}{(n_{eff,co} - n_{eff,cl,m})} \;, \delta\overline{n}_{cm} = \delta\overline{n}_{eff,co} - \delta\overline{n}_{eff,cl,m} \tag{13}$$

Thus, the induced center wavelength shift for the LPFG sensor under a temperature change can be obtained from Eq. (11) as:

$$\frac{d\lambda_{re,m}}{dT} = (1 + \gamma_m \chi_m)\frac{d\lambda_{D,m}}{dT} + \lambda_{D,m}\frac{d}{dT}(1 + \gamma_m \chi_m) \tag{14}$$

in which the effective refractive index change coefficient (χ_m) is defined as:

$$\chi_m = \frac{\delta\overline{n}_{cm}}{(n_{eff,co} - n_{eff,cl,m})} \tag{15}$$

Under a temperature variation, the changes in effective refractive index of the fiber core and cladding mode result from the changes of their thermo-optic coefficients (ρ_{co} for core and $\rho_{cl,m}$ for cladding modes). Their relations are assumed as follows:

$$\frac{dn_{eff,co}}{dT} = \rho_{co} n_{eff,co}, \quad \frac{dn_{eff,cl,m}}{dT} = \rho_{cl,m} n_{eff,cl,m}, \quad \frac{d\delta\overline{n}_{cm}}{dT} = \rho_{co}\delta\overline{n}_{eff,co} - \rho_{cl,m}\delta\overline{n}_{eff,cl,m} \tag{16}$$

The first derivative on the right side of Eq. (12) can be derived and expressed into:

$$\frac{d\lambda_{D,m}}{dT} = \lambda_{D,m}(\varsigma_{T,m} + \alpha) \tag{17}$$

in which the fiber temperature sensitivity coefficient and the thermal sensitivity are respectively defined as:

$$\varsigma_{T,m} = \frac{\rho_{co} n_{eff,co} - \rho_{cl,m} n_{eff,cl,m}}{n_{eff,co} - n_{eff,cl,m}} \text{ and } \alpha = \frac{1}{\Lambda}\frac{d\Lambda}{dT} \tag{18}$$

Since the effective refractive index reduction of cladding is much less than that of core, $\delta\overline{n}_{eff,cl,m} \approx 0$ is introduced and the parameter $\psi_{T,m}$ is defined by:

$$\psi_{T,m} = \frac{\lambda_{D,m}}{n_{eff,co} - n_{eff,cl,m}}[(\rho_{co} - \varsigma_{T,m})\frac{dn_{eff,co}}{d\lambda_{D,m}} - (\rho_{cl,m} - \varsigma_{T,m})\frac{dn_{eff,cl,m}}{d\lambda_{D,m}}] \tag{19}$$

The second derivative on the right side of Eq. (12) can be derived and expressed into:

$$\frac{d}{dT}(1 + \gamma_m \chi_m) = -\frac{\gamma_m(\alpha + \psi_{T,m} + \rho_{co} - \varsigma_{T,m})\delta\overline{n}_{eff,co}}{n_{eff,co} - n_{eff,cl,m}} \tag{20}$$

As a result, Eq. (12) can be simplified into:

$$\frac{d\lambda_{re,m}}{dT} = \lambda_{D,m}\xi_{T,m} \tag{21}$$

in which $\xi_{T,m}$ is the temperature sensitivity coefficient of the LPFG sensor that is determined by:

$$\xi_{T,m} = \alpha + \varsigma_{T,m} + \gamma_m \chi_m (2\alpha + \psi_{T,m} + \rho_{co}) \tag{22}$$

Consider a SMF-28 optic fiber inscribed with CO_2-laser induced long period gratings. In this case, $\rho_{co} = 8\times10^{-6}/^{o}C$ ($1.44\times10^{-5}/$℉), and $\rho_{cl,m} = 7.8\times10^{-6}/^{o}C$ ($1.4\times10^{-5}/$℉) [31, 32]. The corresponding temperature sensitivity coefficient can then be presented in Figure 3.3. From the mode coupling theory [107], γ_m is greater than zero for cladding modes lower than LP_{09} and less than zero otherwise. The parameter $\varsigma_{T,m}$ is always greater than zero for cladding modes lower than LP_{09}. On the other hand, χ_m is always negative for negative s_0. Thus, their combined effects, shown in Figure 3.3 (a, b), indicated that the temperature sensitivity coefficient is always positive.

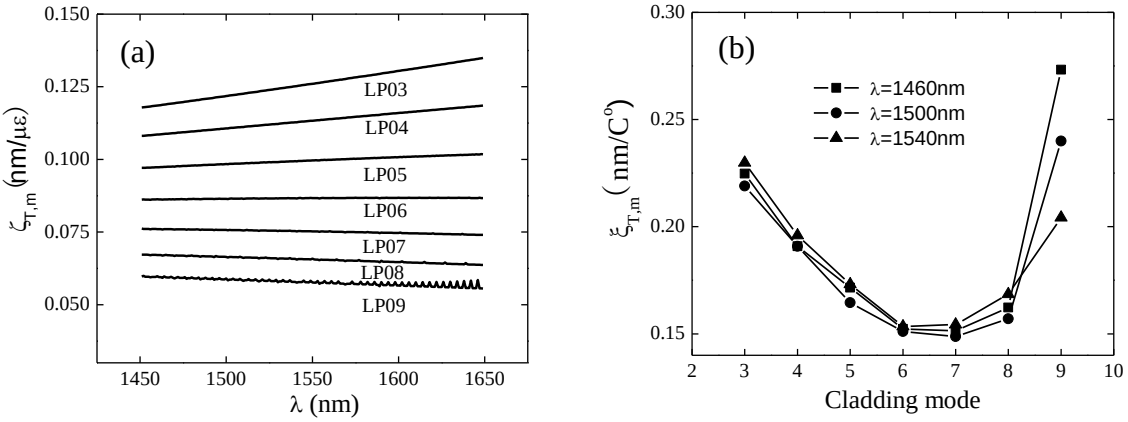

Figure 3.3 Temperature sensitivity $\varsigma_{T,m}$: (a) function of center wavelength and (b) relation with cladding mode

3.2.1.3. Theoretic analysis of strain sensitivity. Similar to the derivation for temperature sensitivity, the center wavelength shift of a LPFG sensor induced by an axial strain can be derived and expressed into:

$$\frac{d\lambda_{re,m}}{d\varepsilon} = \lambda_{D,m}\xi_{\varepsilon,m} \tag{23}$$

in which $\xi_{\varepsilon,m}$ is the strain sensitivity coefficient of the LPFG sensor. It can be written as:

$$\xi_{\varepsilon,m} = 1 + \varsigma_{\varepsilon,m} + \gamma_m \chi_m (2 + \psi_{\varepsilon,m} + \eta_{co}) \tag{24}$$

$$\varsigma_{\varepsilon,m} = \frac{\eta_{co} n_{eff,co} - \eta_{cl,m} n_{eff,cl,m}}{n_{eff,co} - n_{eff,cl,m}} \tag{25}$$

$$\psi_{\varepsilon,m} = \frac{\lambda_{D,m}}{n_{eff,co} - n_{eff,cl,m}} [(\eta_{co} - \varsigma_{\varepsilon,m}) \frac{dn_{eff,co}}{d\lambda_{D,m}} - (\eta_{cl,m} - \varsigma_{\varepsilon,m}) \frac{dn_{eff,cl,m}}{d\lambda_{D,m}}] \tag{26}$$

where η_{co} and $\eta_{cl,m}$ are the elastic-optic coefficients of the core and cladding mode LP_{0m} of the LPFG sensor.

For a single mode fiber (SMF-28), the elastic-optic coefficients of its core and cladding mode can be assumed to be $\eta_{co} = -0.2219$ and $\eta_{cl,m} = -0.22$ [31, 32]. In this case, $\varsigma_{\varepsilon,m}$ is always less than zero for cladding modes lower than LP_{09}, $\psi_{\varepsilon,m}$ is greater than zero for cladding modes LP_{05} or lower, and less than zero for cladding modes LP_{06} or higher. It fluctuates dramatically with wavelength in the interested range. Their combined effect on the strain sensitivity coefficient is presented in Figure 3.4 (a) as the wavelength changes. At the specified wavelengths, the strain sensitivity with various cladding modes is shown in Figure 3.4 (b). It can be seen from Figure 3.4 (b) that the LPFG sensors have a negative strain sensitivity for cladding modes LP_{02} through LP_{05} and positive strain sensitivity for cladding modes LP_{06} through LP_{09}.

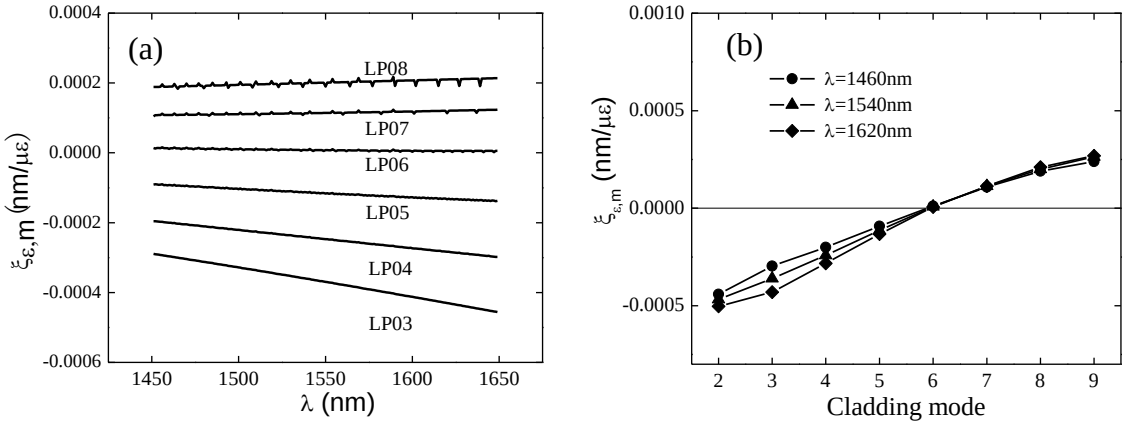

Figure 3.4 Strain sensitivity $\xi_{\varepsilon,m}$: (a) function of center wavelength and (b) relation with cladding mode

3.2.1.4. Simultaneous temperature and strain solution. When a LPFG sensor is subjected to both strain and temperature changes, the shift in its center wavelength can be determined from Eqs. (17) and (19), which can be experssed into:

$$\frac{d\lambda_{re,m}}{\lambda_{D,m}} = \xi_{\varepsilon,m} d\varepsilon + \xi_{T,m} dT \tag{27}$$

By considering two cladding modes, i and j, the strain and temperature changes from the calibration condition can be determined from the measured wavelength shifts by:

$$\begin{Bmatrix} d\varepsilon \\ dT \end{Bmatrix} = \frac{1}{D} \begin{bmatrix} \xi_{T,j} & -\xi_{T,i} \\ -\xi_{\tau,j} & \xi_{\tau,i} \end{bmatrix} \begin{Bmatrix} d\lambda_{re,i} / \lambda_{D,i} \\ d\lambda_{re,j} / \lambda_{D,j} \end{Bmatrix} \tag{28}$$

in which $D = \xi_{\tau,i}\xi_{T,j} - \xi_{\tau,j}\xi_{T,i}$.

3.2.2. Hybrid Strain Transfer Mechanism. Bare optical fibers in tension can typically survive a strain of approximately 0.4% or 4,000 με. To measure large strains, various strain transfer mechanisms have been investigated for embedded optical fiber sensors in recent ten years [108, 109]. However, LPFG is sensitive to its surrounding

environment so that it is not suitable to be embedded into any host structure without packaging and/or any protection. In this section, two basic mechanisms are proposed to increase the dynamic range of strain measuerements.

3.2.2.1. Shear lag effect. Consider an LPFG optical fiber attached to a host material/structure and a small section of the fiber with coating as illustrated in Figure 3.5 [109]. Between the coated fiber (h_p thick) and the host material is an adhesive layer (h_a=h_0 thick) that is used to transfer strain based on the shear lag effect from the host material to the optical fiber. A strain transfer rate (STR<1.0) is defined as the strain ratio between the fiber and the host material.

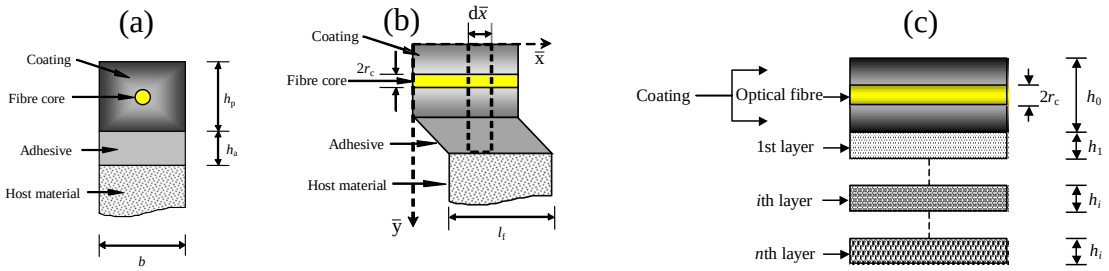

Figure 3.5 Strain transfer model with shear lag effect: (a) cross section, (b) strain distribution, and (c) multi-layer strain transfer

For a general multi-layer system as shown in Figure 3.5 (c), the strain transfer rate can be derived as [109]:

$$STR = \frac{\bar{\varepsilon}_c}{\bar{\varepsilon}_h} = 1 - \frac{\cosh(\lambda l_f) - 1}{\lambda l_f \sinh(\lambda l_f)} \text{ and } \frac{1}{\lambda^2} = E_c h_0 [\frac{(3h_0 - 2r_c)(h_0 + 2r_c)}{8h_0 G_0} + \sum_{i=1}^{n} \frac{h_i}{G_i}] \quad (29)$$

where $\bar{\varepsilon}_c$ and $\bar{\varepsilon}_h$ are the average strains of the optical fiber and the host material, respectively; l_f is the attachment length of the optical fiber; λ is an eigenvalue related to the adhesive layers as given in Eq. (29) [109]; E_c and G_0 are the Young's modulus and shear modulus of the optical fiber, G_i is the shear modulus of the ith adhesive layer of h_i thick.

Since LPFG is highly sensitive to the environment and its transmission spectrum can be severely distorted by the adhesive coating, an LPFG sensor must be attached on its host structure at two points on two sides of the grating as indicated in Figure 3.6 so that the grating is not in direct contact with the host structure. A specially designed adhesive layer can be introduced to transfer strain from the host structure to the LPFG sensor.

3.2.2.2. Gauge length change. From the mechanics of materials [110], it is well known that the average strain of a tension member is inversely proportional to the gauge length between two observation points. As such, by introducing a gauge length change mechanism, the strain in an LPFG attached on a structure can be significantly smaller than that of the structure, achieving a small STR value. As illustrated in Figure 3.7, consider the two rigid blocks of a host structure move apart, resulting in deformation in LPFG1 and LPFG2 sensors. The LPFG1 measures the strain over a length, L, representing the structural strain in practical applications, while the LPFG2 measures the strain over a length of L+2s. Therefore, the STR can be represented by

$$STR = \frac{\varepsilon_{LPFG2}}{\varepsilon_{structure}} = \frac{L}{L+2s} \tag{30}$$

When $s=L/2$, Eq. (30) gives rise to STR=0.5. For example, if the structure is subjected to 3,000 $\mu\varepsilon$, the LPFG2 will measure 1,500 $\mu\varepsilon$ only as a result of reduced deformation on the optical fiber.

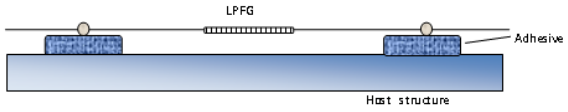

Figure 3.6 Shear lag effect mechanism

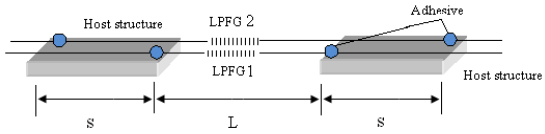

Figure 3.7 Gauge length change

3.2.2.3. Large strain LPFG sensors with a hybrid transfer mechanism. The two basic strain transfer mechanisms discussed in the previous sections can be combined to develop a hybrid transfer mechanism as illustrated in Figure 3.8. This novel LPFG sensor has multi-layer adhesives at each end of the optical fiber that is placed inside a

stiff structural member such as a steel tube that can be welded or a glass tube that can be attached with adhesive to the host structure at two points of L distance apart. The tube consists of two parts with a sleeve joint between the two supports on the host structure to facilitate their relative axial elongation. The steel or glass tube can protect the sensor from damage, environmental disturbance, and bending effect. The strain measured with the LPFG sensor over the length (L+2s) is first converted to the strain between the two sensor attachment points of the tube, which is then converted to the average strain over the length (L). Therefore, the STR of the hybrid mechanism is actually equal to the multiplication of Eq. (29) and Eq. (30), as shown in Eq. (31):

$$STR = \left(1 - \frac{\cosh\left(\beta\left(l-x\right)\right)-1}{\beta\left(l-x\right)\sinh\left(\beta\left(l-x\right)\right)}\right)\left(1-\frac{2y}{L+2y}\right) \tag{31}$$

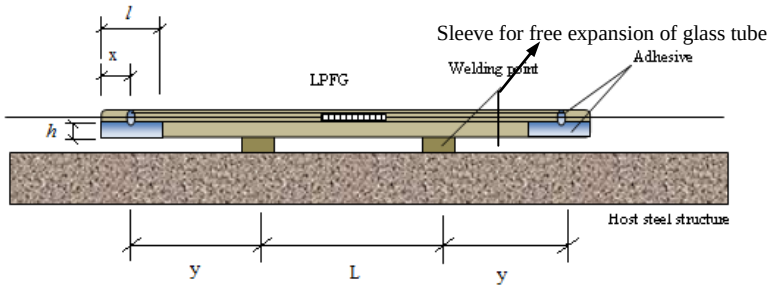

Figure 3.8 A novel LPFG sensor with hybrid strain transferring

The hybrid strain transfer based LPFG sensor combines the two basic mechanisms whose individual effectiveness has been demonstrated in Figures 3.6 and 3.7. Since the limitation of the shear lag and gauge length based LPFG are 50% and 25% respectively, the maximum strain sensitivity adjustment of the hybrid mechanism based LPFG sensor is 12.5% as shown in Figure 3.9. Figure 3.9 compares the strain felt by an LPFG with the strain in the host structure for four cases: without strain transfer effect, with shear lag effect, with gauge length change, and with shear lag and gauge length change (hybrid mechanism). In comparison with the benchmark without strain transfer, the slopes in Figure 3.9 corresponding to the three mechanisms or STR values decreases in order with the use of shear lag, gauge length change, and hybrid mechanism. The

calibration sensitivity without strain transfer is the highest. The effect of the hybrid mechanism is approximately equal to the combined effects of both shear lag and gauge length change. As a result, the LPFG sensor with the hybrid mechanism can measure a level of strains in structures, 24,000 με. This level is approximately 8 times the usable strain of the LPFG optical sensor.

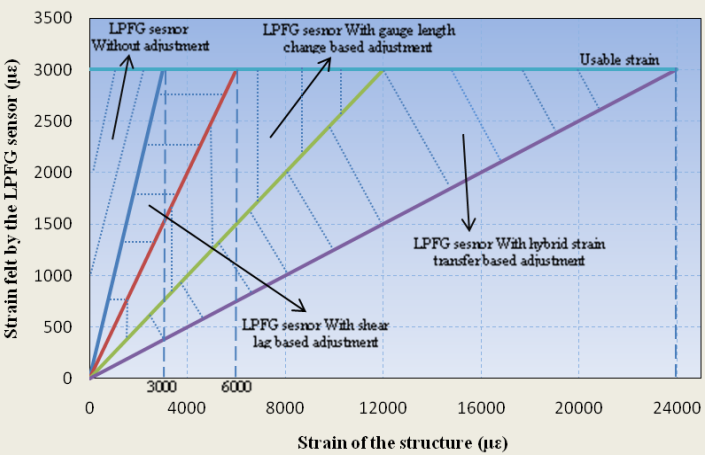

Figure 3.9 Effects of various strain transfer mechanism

3.2.3. Experiments and Discussion.

3.2.3.1. Performance of unpackaged LPFG sensors. A series of tests were conducted for temperature effects. The center wavelength of a LPFG sensor was determined and plotted in Figure 3.10 (a) as a function of the applied temperature. It is observed from Figure 3.10 (a) that the resonant center wavelength of the tested LPFG sensor with a cladding mode from LP_{04} to LP_{07} linearly increases with temperature. The theoretic predictions are compared with the experimental results in Figure 3.10 (b) and Table 3.1. It can be seen that the theoretic prediction underestimated the temperature sensitivity by less than 12% but was in general agreement with the test data. This comparison validates the analytical results presented in Figure 3.10 (b).

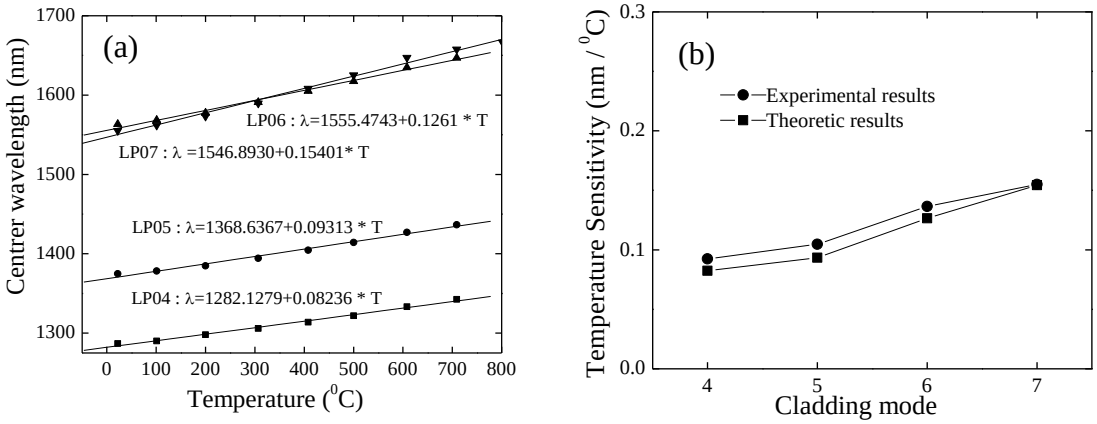

Figure 3.10 Sensor validation: (a) temperature sensitivity and (b) cladding mode effect

Table 3.1 Comparison between experimental and theoretic results of LPFG sensors

Cladding mode	Initial center wavelength (nm)	Experimental Strain sensitivity (nm/με)	Theoretic strain sensitivity (nm/με)
4	1282.128	0.08236	0.09237
5	1368.578	0.09343	0.10470
6	1555.392	0.12660	0.13650
7	1546.920	0.15440	0.15500

Another series of tension tests were conducted with a LPFG sensor at room temperature (22 ℃). All tension tests were performed both in loading and unloading cycles to verify the repeatability of sensor readings. The center wavelength of each transmission spectrum was determined and plotted in Figure 3.11 (a) as a function of the applied strain and summarized in Table 3.2. The strain sensitivities of the LPFG sensor for different cladding modes are presented in Figure 3.11 (b) and also included in Table 3.2. It is observed from Figure 3.11 (a) that the resonant wavelength of the sensor linearly increases with the applied strain for cladding modes LP_{06} through LP_{08} and decreases for cladding modes LP_{04} and LP_{05}. The cladding modes LP_{04} and LP_{05} have "negative" sensitivities as clearly seen in Figure 3.11 (b) and summarized in Table 3.2. Figure 3.11 (b) also indicates that the theoretical and experimental results follow the same trend.

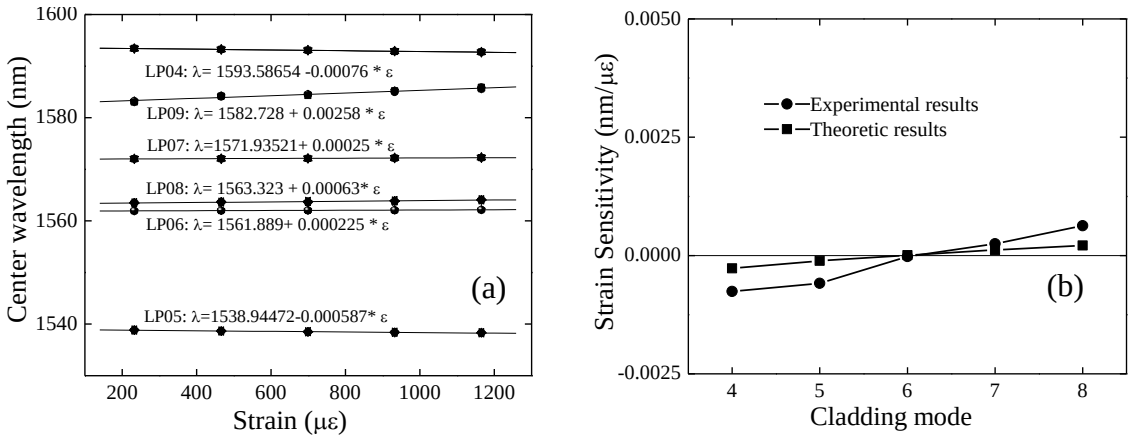

Figure 3.11 Sensor validation: (a) strain sensitivity and (b) cladding mode effect

Table 3.2 LPFG sensor calibration for strain measurement

Cladding mode	Initial center wavelength (nm)	Experimental strain sensitivity (nm/με)	Theoretic strain sensitivity (nm/με)	Break strain (με)
4	1593.689	-0.000760	-0.00027	2800
5	1538.845	-0.000587	-0.00011	3000
6	1561.969	+0.000225	+0.00005	3250
7	1571.935	+0.000250	+0.00021	3500
8	1563.323	+0.000630	+0.00023	3600

Before a large strain packaged LPFG sensor prototype had been fabricated, a new SMF-28 bare LPFG sensor was tested to obtain its calibration strain and temperature sensitivities simultaneously. Figures 3.12 (a) and (b) show a spectrum change of the LPFG sensor under various strains and its corresponding strain sensitivities at 20 ^{0}C (68 ℉) for two cladding modes, LP_{07} and LP_{06}. The strain sensitivities of cladding mode LP_{07} and LP_{06} are 3.064×10^{-4} nm/με and -2.547×10^{-4} nm/με, respectively. Figures 3.12 (c) and (d) demonstrate a spectrum change of the LPFG under various temperatures and its corresponding temperature sensitivities at zero strain for the two cladding modes. The temperature sensitivities of cladding mode LP_{07} and LP_{06} are 0.1634 nm/℃ and 0.0978 nm/℃, respectively. The center wavelength of the LPFG sensor is related to both the applied strain and the applied temperature linearly, indicating a well-behaved LPFG sensor. With the calibration sensitivities, all the parameters in Eq. (27) and (28) can be

determined. The strain and temperature effects can then be obtained simultaneously from the measured center wavelength change of two cladding modes of the tested LPFG sensor.

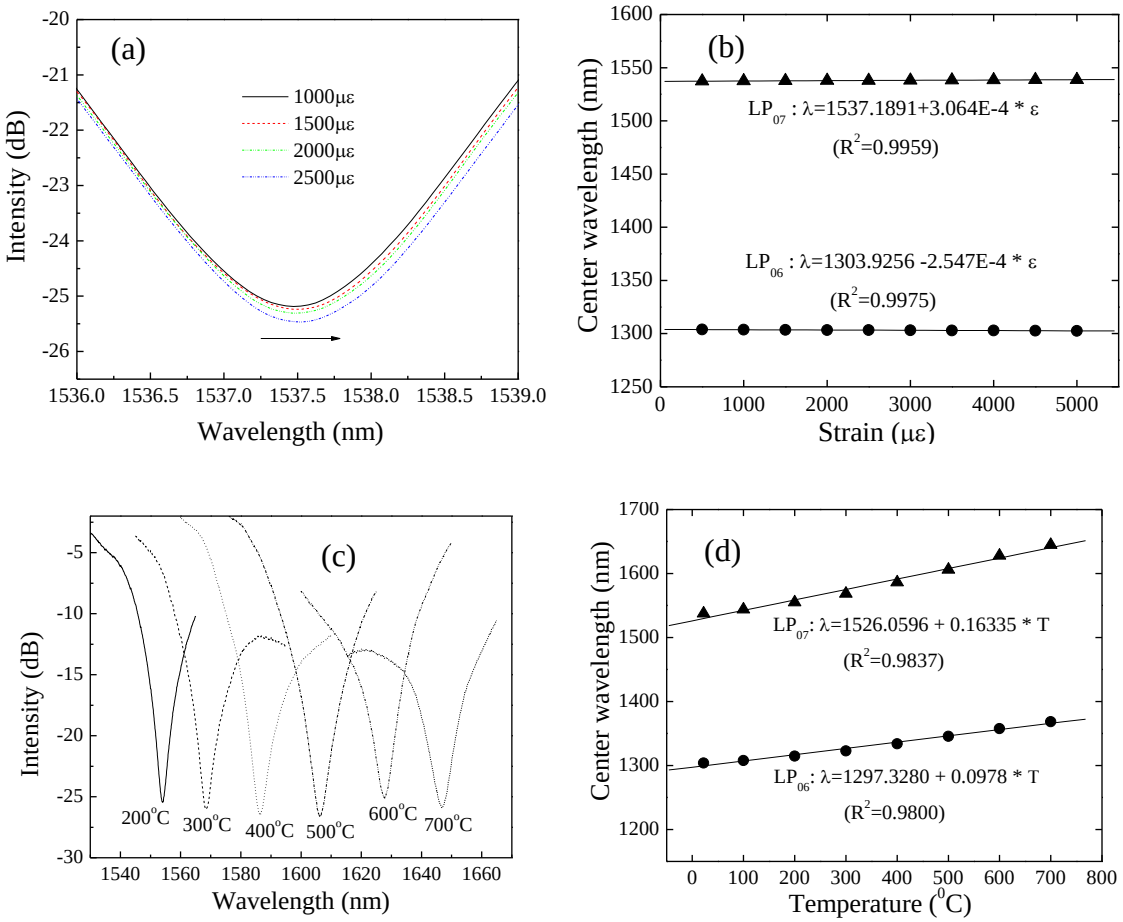

Figure 3.12 LPFG sensor calibration for simultaneous strain and temperatuer measurements: (a) spectral change with increasing strains: LP_{07}, (b) strain sensitivity for two cladding modes: LP_{06} and LP_{07}, (c) spectral change under various temperatures: LP_{07}, and (d) temperature sensitivity for two cladding modes: LP_{06} and LP_{07}

3.2.3.2. Performance of the hybrid strain transfer machanism.

3.2.3.2.1. <u>Shear lag effect.</u> A comparative experiment was designed with three attachment schemes of LPFG sensors as illustrated in Figure 3.13. LPFG1 was placed at the center points of two adhesive blocks; LPFG2 and LPFG3 were attached to two inner and outer points of the adhesive blocks, respectively. As shown in Figure 3.14, the host structure is a tapered steel beam with 1.9 cm (¾ in.) thickness, 30.48 cm (12 in.) length

and end width of 12.7 cm (5 in.) that was cantilevered and subjected to uniform strains under a concentrated load at the tip of the tapered beam.

The transmission spectra of the LPFG1 sensor with cladding mode LP_{07}, Figure 3.13 (a), are plotted as a function of the applied load in Figure 3.15 (a). The center wavelengths at various loads are plotted as a function of the applied strain in Figure 3.15 (b). The strain sensitivities of all three cases are summarized in Table 3.3. It can be observed from Table 3.3 that the strain sensitivity varies with the attachment points of the LPFG sensor. In comparison with the calibration sensitivity (+0.00401 nm/με), the strain sensitivity (+0.00325 nm/με) remains high through multi-layer adhesives for the sensor attached at the center of adhesives. When attached at two inner points, the tension effect on the optical fiber is increased so that the strain sensitivity (negative) loses almost half of its corresponding calibration sensitivity. The opposite case is also true so that the strain sensitivity increases more than twice its corresponding calibration sensitivity. In addition, the multi-layer adhesives not only change the strain sensitivity of the LPFG sensor but also reduce the bending effect on the LPFG. Although the LPFG with cladding mode LP_{07} loses its strain sensitivity by approximately 20% due to bending effect, it generally works well under bending. For LPFG sensors with cladding mode lower than LP_{06}, the bending effect has increased the strain sensitivity to certain extent.

For large strain LPFG sensors, multi-layer adhesives with a certain length can be a promising mechanism for civil engineering applications. Engineers can use Eq. (27) to choose adhesive material, layer thickness, and anchorage length in order to achieve various strain sensitivities in their applications. Due to the limited size of steel tubes and the Young's Modulus of the adhesive, the maximum strain sensitivity by shear lag effects is approximately 50% as shown in Figure 3.9.

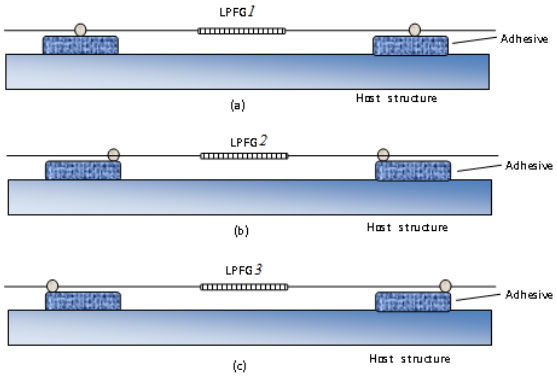

Figure 3.13 LPFG attachment schemes

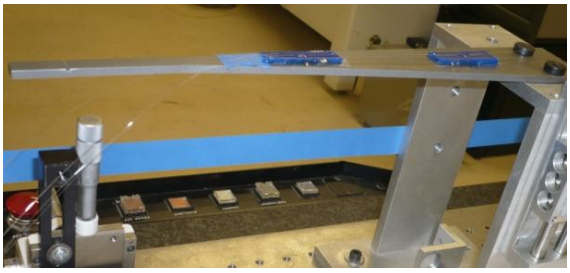

Figure 3.14 Testing of cantilevered beam

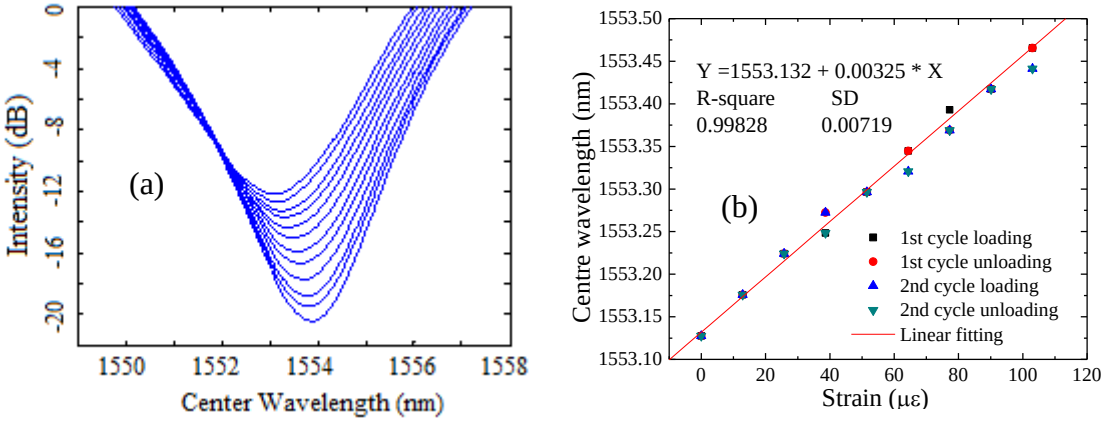

Figure 3.15 Shear lag effect on strain transfer: (a) LFPG1 transmission spectra with cladding mode LP_{07} and (b) measured strain from LPFG1 with mode LP_{07}

Table 3.3 Characteristic properties of LPFG sensors with multi-layer adhesives

Sensor designation	Support location	Cladding mode	Initial center wavelength (nm)	Strain sensitivity (nm/με)	Calibration sensitivity (nm/με)
LPFG1	Center	LP_{07}	1553.132	+0.00325	+0.00401
LPFG2	Inner	LP_{05}	1547.380	-0.00032	-0.00059
LPFG3	Outer	LP_{05}	1551.855	-0.00148	-0.00059

3.2.3.2.2. <u>Gauge length change.</u> A simple test as shown in Figure 3.16 was set up to study the feasibility of strain transfer by gauge length changes. In this case, two

sensors (LPFG1 and LPFG2 in cladding mode LP_{04}) were subjected to axial deformation. The center wavelength is related to the applied strain as presented in Figure 3.16 (a, b) for two LPFGs. The sensing properties of the two sensors are summarized in Table 3.4. It is clearly seen from Table 3.4 that the strain sensitivity of the LPFG2 reduces more than half of its corresponding calibration value as the sensing gauge length increases by two times. This result verifies the strain transfer mechanism. Considering the installation convenience and the sensing property requirement, it is recommended that the maximum strain sensitivity that can be achieved with the gauge length change mechanism is approximately 25% as shown in Figure 3.9.

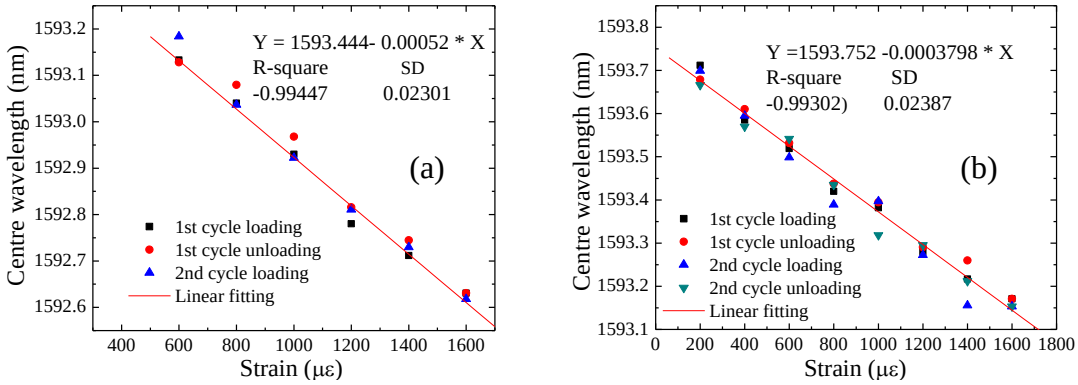

Figure 3.16 Effects of gauge length change (LP_{04}): (a) LPFG1 and (b) LPFG2

Table 3.4 Characteristic properties of LPFG sensors with gauge length changes

Sensor designation	Cladding mode	Initial center wavelength (nm)	Strain sensitivity (nm/με)	Calibration strain sensitivity (nm/με)
LPFG1	LP_{04}	1593.444	-0.000521	-0.00053
LPFG2	LP_{04}	1593.752	-0.000380	-0.00072

3.2.3.2.3. <u>Hybrid strain transfer mechanism.</u> Based on the strain transfer theory, large strain sensors have been developed and their strain sensitivity and sensing properties have been investigated by tensile tests, as shown in Figure 3.17. The large strain sensor based on gauge length change only is shown in Figure 3.17 (a). LPFG is packaged in a small steel tube with gauge length 10 mm (0.4 in.) to ensure that the LPFG

can move smoothly with the deformation of the host structure. The small steel tube is then enclosed by a larger steel tube to allow for free sliding. The large strain sensor based on the hybrid strain transfer is shown in Figure 3.17 (b). The LPFG is also packaged in a small steel tube, and the small steel tube is installed into two larger steel tubes. Parts of the larger steel tubes have been cut into half tubes so that the adhesive can be put into the tube with exact length and thickness. LPFG is adhered to the larger steel tube by two points with 15 mm (0.6 in.) gauge length on the adhesive blocks with a length of 3 mm (0.12 in.) and a thickness of 1mm (0.04 in.). Both packaged LPFG sensors are installed on an aluminum sheet by adhesive. LPFG1 sensor has a gauge length of 5 mm (0.2 in.) and LPFG2 sensor has a gauge length of 6 mm (0.24 in.).

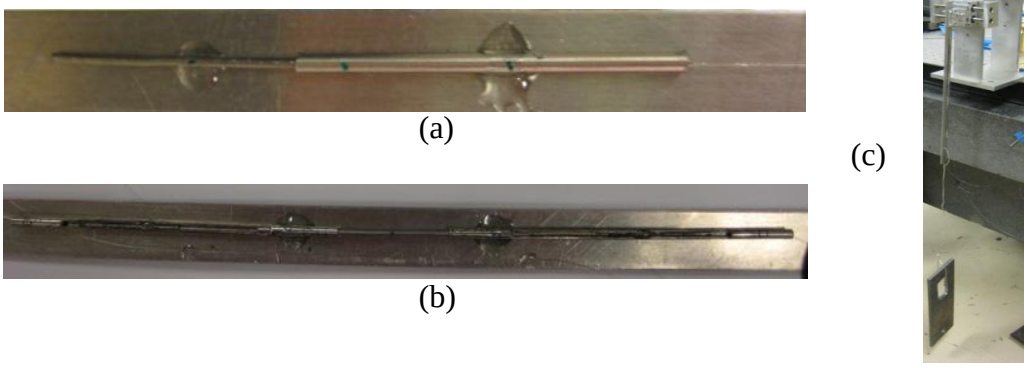

Figure 3.17 Sensor structure and test setup: (a) gauge length change mechanism with LPFG1, (b) hybrid strain transfer: LPFG2, and (c) test setup

The test results are presented in Figure 3.18 and the comparison of the sensors are shown in Table 3.5. It is shown from the test results that the linearity and repeatability of the LPFG sensors are good enough for application. The results also show that if the strain of the host structure is approximately 16 με, the strain felt by LPFG1 is about 9 με and that of LPFG2 is approximately 6 με. The strain transfer rate of LPFG1 is around 60% and that of LPFG2 is about 23%, whereas the theoretic strain transfer rates are 50% and 28%. Experimental results and theoretic results are compared. This test verified the applicability of these kinds of LPFG large strain sensors.

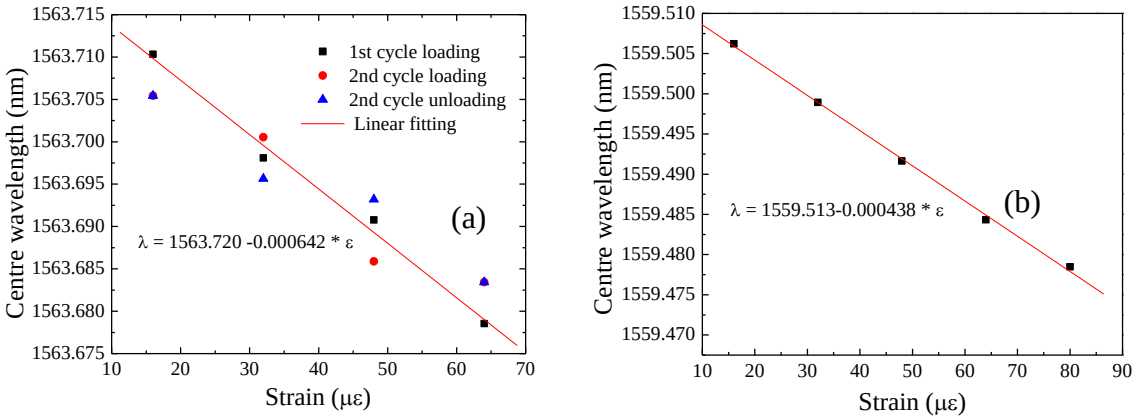

Figure 3.18 LPFG large strain sensor test results: (a) LPFG1 and (b) LPFG2

Table 3.5 Strain measurement of LPFG sensors with hybrid mechanism

Sensor	Cladding mode	Initial center wavelength (nm)	Strain sensitivity (nm/με)	Calibration sensitivity (nm/με)	Actual STR (%)	Theoretic STR (%)
LPFG1	LP_{05}	1563.720	-0.000642	-0.00105	61.1	50
LPFG2	LP_{05}	1559.613	-0.000438	-0.00192	22.8	28

3.2.3.3. Performance of a packaged prototype LPFG sensor.

3.2.3.3.1. <u>Large strain sensor prototype.</u> For large strain measurements, the bare LPFG sensor used for calibration tests was packaged with a strain transfer mechanism to form a packaged LPFG sensor prototype as shown in Figure 3.19. Two steel channels were fixed on two computer controlled precise stages. The packaged LPFG sensor was attached on the two steel channels with one high temperature adhesive pad on each channel, similar to Figure 3.14. In this study, y = 0.5L and L = 10 cm (3.94 in.). A furnace made by Thermo Electron Corporation was placed between the two precise stages to provide the required high temperature environment. According to Eq. (31), the theoretic strain sensitivity of the LPFG should be 25% of the calibration sensitivity. For example, if the separation between the two steel channels corresponds to a strain of 5000 με, the LPFG sensor registers only 1250 με.

Figure 3.19 LPFG lager strain sensor prototype based on the hybrid strain transfer

3.2.3.3.2. <u>Strain sensitivities of various cladding modes.</u> Figures 3.20 (a, b) show the center wavelength change of the cladding modes LP_{06} and LP_{07} under various strains, respectively, when the sensor measurements are taken at room temperature (22 ℃). A strain sensitivity of -6.035×10^{-5} nm/με for cladding mode LP_{06} corresponds to 24% of the calibration strain sensitivity. A strain sensitivity of 5.974×10^{-5} nm/με for cladding mode LP_{07} represents 20% of the calibration strain sensitivity. The strain sensitivities of the developed large strain sensor prototype at various temperatures are presented in Figures 3.20 (c, d) for LP_{06} and LP_{07}, respectively. When the applied temperature is below 700 ℃ (1292 ℉), the strain sensitivity of the packaged LPFG sensor with cladding mode LP_{06} ranges from -5×10^{-5} to -8×10^{-5}nm/με as illustrated in Figure 3.20 (c), resulting in 20% to 32% of that of the bare LPFG sensor. With the cladding mode LP_{07}, the strain sensitivity of the packaged LPFG sensor ranges from 5×10^{-5} to 7×10^{-5} nm/με as illustrated in Figure 3.20 (d), which is 17% to 22% of that of the bare LPFG sensor. The overall strain transfer rate based on various measurements at temperature below 700 ℃ (1292 ℉) changes from 17% to 32% of that of the calibrated bare LPFG sensor, which is approximately centered at the theoretic value of 25%.

At 700 ^{0}C (1292 ℉), the strain sensitivity of the tested LPFG sensor increased nearly twice of that at room temperature. This dramatic change was mainly attributed to the breakdown of adhesives and the degradation of gratings at the elevated temperature. In this case, the strain transfer mechanism came from the gauge length change only. At 800 ℃ (1472 ℉), the sensor became mal-functional. At 700 ℃ (1292 ℉) or higher, other temperature-tolerant adhesives must be used to package the LPFG sensor and ensure its satisfactory performance if gratings can survive the high temperature environment. During tests, it was observed that, as the applied temperature increased, it became a challenge to accurately measure the strain sensitivities mainly due to high temperature sensitivity and difficulty in maintaining a stable high temperature environment. A slight change in temperature greatly affected the strain sensitivity.

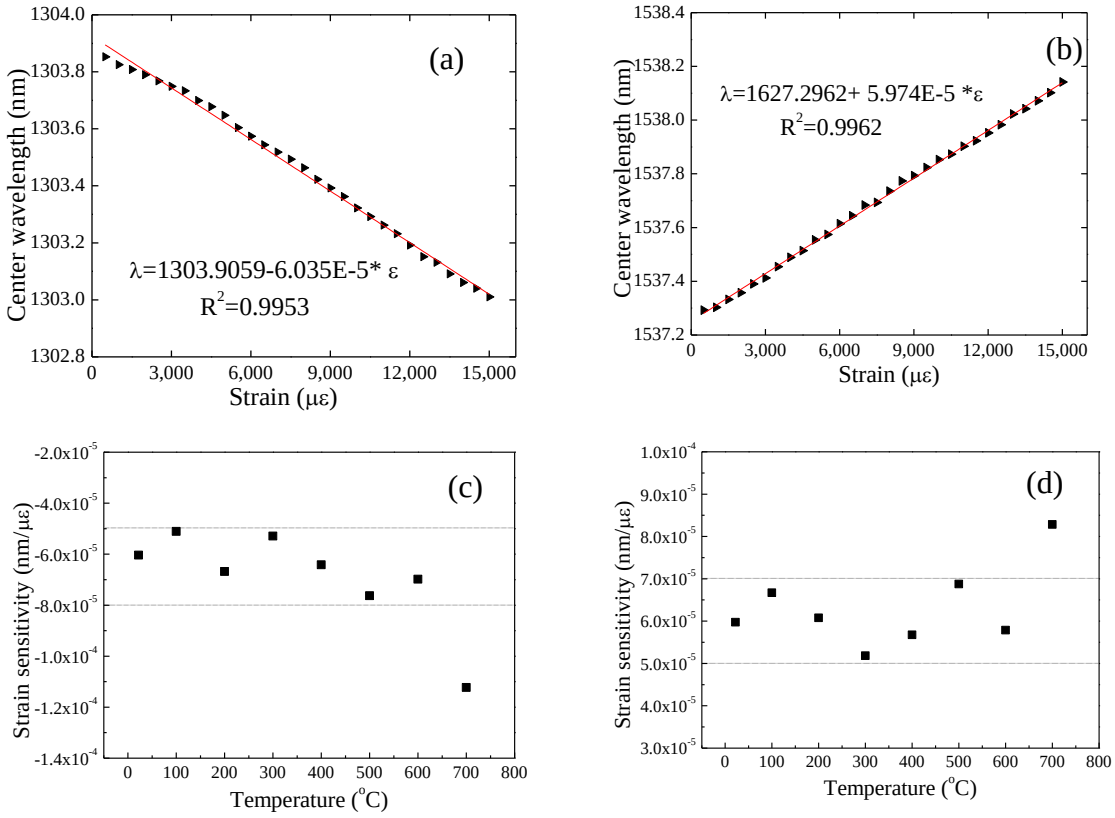

Figure 3.20 Strain sensitivity of LPFG sensors at various temperatures: (a) strain sensitivity for LP_{06} at room temperature, (b) strain sensitivity for LP_{07} at room temperature, (c) strain sensitivity for LP_{06} at various temperatures, and (d) strain sensitivity for L

3.2.3.3.3. <u>Strain transfer effect.</u> The applied strain and temperature can be simultaneously evaluated from Eq. (31) with the use of two cladding modes of a packaged LPFG sensor. To understand the strain transfer effect, two sets of calibration strain sensitivities were used: one for the packaged sensor and the other for its corresponding unpackaged/bare optical sensor. The calibration condition considered in Eq. (31) was zero strain and room temperature (20 ^{0}C or 68 ℉). The application condition in this study was 600 ^{0}C (1112 ℉) and a structural strain of 4,000 με. The center wavelength differences of the two cladding modes applied for strain and temperature determination were differences of the measured center wavelengths between the calibration and application conditions for the packaged LPFG sensor. Table 3.6 lists the determined strain and temperature of the bare LPFG sensor using its calibration

sensitivities as shown in Figures 3.12 (b, d), which are the temperature sensitivity at zero strain and the strain sensitivity at room temperature (20 ^{0}C or 68 ℉). Table 3.7 gives the separated strain and temperature of the packaged sensor or a substructure (represented by two separate channels in various experiments) evaluated from the same measured center wavelengths as used in Table 3.6. However, the calibration strain sensitivities for both cladding modes in Table 3.7 were measured from the packaged LPFG sensor as shown in Figure 3.21 (a, b), including the package effect. The overall errors for both strain and temperature likely result from the use of calibration sensitivities obtained at a temperature different from the application temperature, which implies the existence of potential cross coupling between the strain and the temperature [111].

Table 3.6 Strain and temperature based on calibration sensitivities of the bare LPFG

LPFG cladding mode j	$d\lambda_{re,j}$ (nm)	Calibration sensitivities		Strain (με)			Temperature (^{0}C)		
		Strain ($\times10^{-4}$ nm/με)	Temperature (nm/ ℃)	Measured	Theoretic	Error	Measured	Exact	Error
7	90.23	3.064	0.1634	895	4000 ×25%	-11%	573	600	-5%
6	53.62	-2.547	0.0978						

Table 3.7 Strain and temperature based on calibration sensitivities of the packaged sensor

LPFG cladding mode j	$d\lambda_{re,j}$ (nm)	Calibration sensitivities		Strain (με)			Temperature (^{0}C)		
		Strain ($\times10^{-5}$ nm/με)	Temperature (nm/ ^{0}C)	Measured	Exact	Error	Measured	Exact	Error
7	90.23	5.974	0.1634	4082	4000	2%	573	600	-5%
6	53.62	-6.035	0.0978						

The strain in Table 3.7 was evaluated with the calibration strain sensitivities that were obtained with the packaged sensor. It is only 2% overestimated from its exact value. In comparison with Table 3.6, Table 3.7 shows a significantly higher error in strain measurement applied on the optical fiber due to additional uncertainties in the strain transfer mechanism, such as adhesive pads. The measured exact strain from the packaged sensor is transferred to its corresponding strain applied on the optical fiber by a 0.25

factor, a theoretic strain transfer ratio discussed previously. In fact, the ratio between the measured strains in Tables 3.6 and 3.7 is 22%, which is close to the theoretical prediction of 25%. The above experimental results verified the workability and general reliability of the sensor design and configuration for simultaneous large strain and high temperature measurements.

3.2.4. Main Findings with LPFG Sensors. A packaged LPFG sensor has been developed for simultaneous large strain and high temperature measurements. Based on extensive tests and analyses, the following conclusions can be drawn:

(1) Unlike UV fabrications, CO_2-laser induced irradiations result in a bare LPFG sensor that has various strain sensitivities from negative for cladding mode LP_{06} or lower to positive for LP_{07} or higher. The switch in sign of the strain sensitivity coefficient is attributed to the two competing factors: grating period and refractive index changes as a result of strain increase. The temperature sensitivity of the LPFG sensor is always positive up to LP_{09}.

(2) The proposed hybrid strain transfer mechanism for large strain measurement combines both gauge length change and shear lag effects. It enables strain measurements up to four times the breaking point of a bare LPFG sensor. A single mode SMF-28 optical fiber with long period gratings breaks at approximately 4,000 με. With the proposed packaging method, it can be used to measure strains of as high as 15,200 με. This packaging method has been demonstrated to work well up to 700 ℃ (1292 ℉) beyond which different adhesives must be used to bond the optical fiber, the steel channel, and the substrate.

(3) The temperature sensitivity of a LPFG sensor is significantly higher than the strain sensitivity. For a given change of center wavelength, 1 ℃ (1.8 ℉) increase in temperature is equivalent to over 1,000 με increase in strain.

(4) Both strain and temperature can be measured simultaneously with a single LPFG sensor using two different cladding modes, particularly those with positive and negative sensitivities. This solution process works well both at room and elevated temperatures.

Even with the hybrid strain transfer mechanism, the maximum strain that a packaged LPFG sensor can reach is limited to 2.5%. This level of strain measurement is

insufficient for the structural behavior monitoring of steel structures in harsh environments such as fire, post-earthquake fire, explosion, and impact effects. Therefore, an alternative strategy referred to as a hybrid LPFG/EFPI sensor is introduced in the following section.

3.3. A HYBRID EFPI/LPFG SENSOR

Rao et al. [112, 113] presented a system combining extrinsic Fabry-Perot interferometric sensor (EFPI) and a chirped in-fiber Bragg grating (chirped FBG), an improved EFPI/FBG system and a FBG/EFPI/LPFG system for simultaneous strain and temperature measurement. Nguyen et al. [114] incorporated a fiber Bragg grating (FBG) sensor into a Lyot fiber filter (LFF) by fusion splicing the FBG and a section of high birefringence fiber (PM fiber), which is an elliptical core side-hole fiber, and then placing them between two polarizers. However, normal FBG sensors cannot sustain extremely high temperature exceeding 300 ℃ (572 ℉). Han et al. [115] reported that by using two LPFGs induced by UV irradiation with positive and negative temperature sensitivities, the peak of the two LPFGs separated with the temperature change and since the two LPFGs had similar strain sensitivity, the resonant peak shift can be obtained with the strain change. In some cases, the gauge length of one of the two LPFGs was too long for field applications. Frazao et al. [116] introduced two cascaded high-birefringence fiber loop mirrors (HiBi-FLM) for simultaneous measurements of strain and temperature. For the two cascaded FLMs approach, only the FLM containing a section of the fiber with elliptical inner cladding acts as the sensor head. The separation of strain and temperature was achieved by simultaneously monitoring the wavelength and the optical power variation of one peak in the transmitted spectrum of the cascaded FLM system. Zhao et al. [117] presented a new design for a simultaneous strain and temperature measurement using a HiBi-FLM concatenated with a temperature-insensitive long-period FIBER grating written in a photonic crystal fiber (PCF). The FLM acts as a sensor head, while the LPFG in PCF serves as a filter to convert the wavelength variation to optical power change. By measuring the wavelength variation and the power difference of two near peaks in the spectral response of this configuration, simultaneous strain and temperature

measurements are obtained. Rao et al. [118] reported a hybrid fiber-optic sensor consisting of a LPFG and a micro EFPI which can achieve a reasonable measurement of strain under high temperature. However, there are no further research and applications done to optimize the system thus far.

The previous works on hybrid optical fiber systems were intended to search for a cost-effective way of simultaneous strain and temperature measurements. In practical applications, however, one needs not only a hybrid sensor but also a multiplexed sensor network. To monitor the behavior of a large-scale civil engineering structure, a significant number of optical fiber sensors must be installed on the structure, which could amount the cost of a sensor network system to be sizable. Ideally, a multiplexed hybrid sensor system or network is addressed by one input and one output fiber. Each sensor encodes the optical carrier with the information of sensed physical parameters, and the total optical output is conveyed to a detector and de-multiplexer that separate the encoded information relevant to each sensor into an appropriate number of channels for subsequent sensor demodulation and additional processing. However, in practice, more than one input and output fibers or a fiber sensor array may be required to address urgent civil engineering issues. In this section, an emphasis is placed on the development of a hybrid LPFG and movable EFPI sensor system for large strain and high temperature measurements.

3.3.1. Sensor Structure and Operational Principles. A hybrid sensor of movable EFPI and LPFG components (EFPI/LPFG) was designed and fabricated by combining a CO_2 laser induced LPFG sensor with the movable EFPI developed in Chapter 2. Due to its two-order (100 times) lower strain sensitivity than temperature sensitivity, the LPFG component of the hybrid sensor is regarded as a temperature sensing component in the proposed hybrid sensor. On the other hand, the EFPI component whose temperature sensitivity depends upon the thermal coefficient of the optical fiber and the glass tube, 0.5×10^{-6} strain/℃. The cross effect of temperature on strain measurement can be neglected. Therefore, the movable EFPI component of the hybrid sensor worked as the strain sensing component [55]. Figure 3.21 (a) shows the schematic of a hybrid EFPI/LPFG sensor structure. The structure of the movable EFPI is

identical to the one introduced in Chapter 2 and all the components are bound with high temperature tolerable adhesives [55].

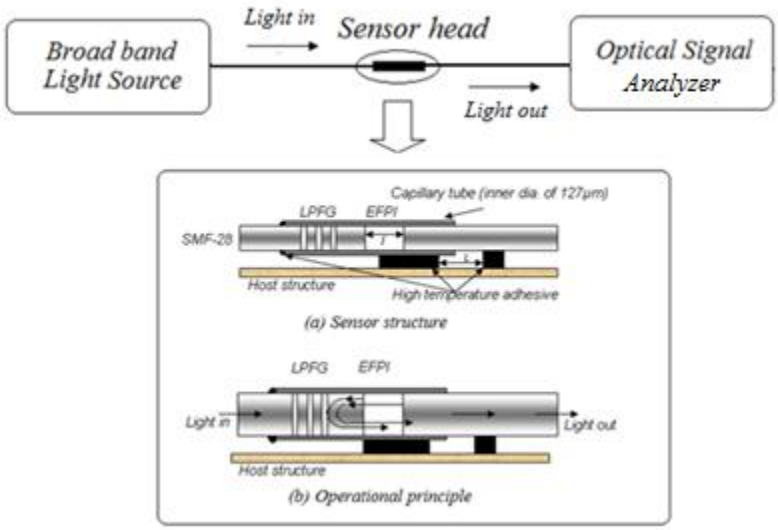

Figure 3.21 Schematic of a network system based on hybrid EFPI/LPFG sensors

As shown in Figure 3.21, light coming through the input fiber will transmit through the two end faces of the EFPI cavity. Since the distance between the LPFG and the EFPI end-face is short, typically less than 5 cm (1.97 in.), the reflected light from the near-end face of the EFPI will be reflected by the LPFG mirrors. Thus, the two branches of secondly reflected lights (by the LPFG mirrors) form an interferometer at the optical signal analyzer (OSA) output spectrum together with the spectrum of the LPFG. The spatial frequency of the interferometer is only a function of the EFPI cavity length and its refractive index change which will not affect the transmission signal of the LPFG itself as a sensor component. The typical output of the OSA can be seen in Figure 3.21.

3.3.2. Decomposition of the Signal from a Hybrid EFPI/LPFG Sensor. To measure temperature and strain at the same structural location, the distance between LPFG and EFPI components must be short, say less than 5 cm. With such a short distance between two sensor components, the transmission signal of a hybrid sensor represents a combined effect of individual LPFG and EFPI components. That is, one transmission measurement contains all the information from both LPFG and EFPI sensors. Figure 3.22

(a) illustrates a typical optical spectrum of the hybrid EFPI/LPFG sensor and Figure 3.22 (b) shows the Fast Fourier Transform (FFT) of the spectral interferogram. It can be seen from Figure 3.22 (b) that the frequency components of the LPFG are low and with a cavity length of over 20 μm, the frequency component of the EFPI is higher than that of the LPFG. Thus, to multiplex the signals from the LPFG and EFPI components, a low-pass spectral Fourier transform filter was applied. After filtering, the spectrum of the LPFG and its spectral Fourier transform can be seen in Figures 3.22 (c, d). As shown in Figure 3.22 (e), the spectrum of the EFPI was then obtained by subtracting the spectrum in Figure 3.22 (c) from the spectrum in Figure 3.22 (a). The resulted Fourier spectrum is presented in Figure 3.22 (f). With the multiplexed signal from LPFG and movable EFPI components, the temperature and strain information can be correlated based on the data processing methods discussed in Chapter 2 and Section 2 of Chapter 3.

3.3.3. Experimental Validation and Discussion.

3.3.3.1. Strain sensing. A hybrid EFPI/LPFG sensor was fixed on two movable stages with a gauge length of 2 mm (0.08 in.). The experimental results of the sensor are presented in Figure 3.23. As the cavity length of the EFPI increases, the signal from the EFPI/LPFG changes significantly. Figure 3.23 (a) shows the transmission spectra of a hybrid EFPI/LPFG sensor at various EFPI cavity lengths. It can be observed from Figure 3.23 (a) that the spectral signal significantly changes with the EFPI cavity. Figure 3.23 (b) illustrates the transmission spectra of the EFPI component and its FFT spectra in wavenumber space. As the cavity length increases from 20 to 260 μm, the spatial frequency of the EFPI signal increases. By considering an EFPI cavity length change from 20 to 260 μm, the gauge length and the initial cavity length of the EFPI part can be selected for a proper measurement of strain in various ranges. With the same initial cavity length of the EFPI (20 μm) and a gauge length of the EFPI of 2 mm, the maximum strain that can be measured is approximately 12%. As such, the hybrid EFPI/LPFG sensor can provide a viable solution for large strain measurement with a simple sensor structure. Figure 3.23 (c) and Figure 3.23 (d) respectively compare the cavity length and its corresponding strain between the measured from the spectral signal and the exact value from the two movable stages.

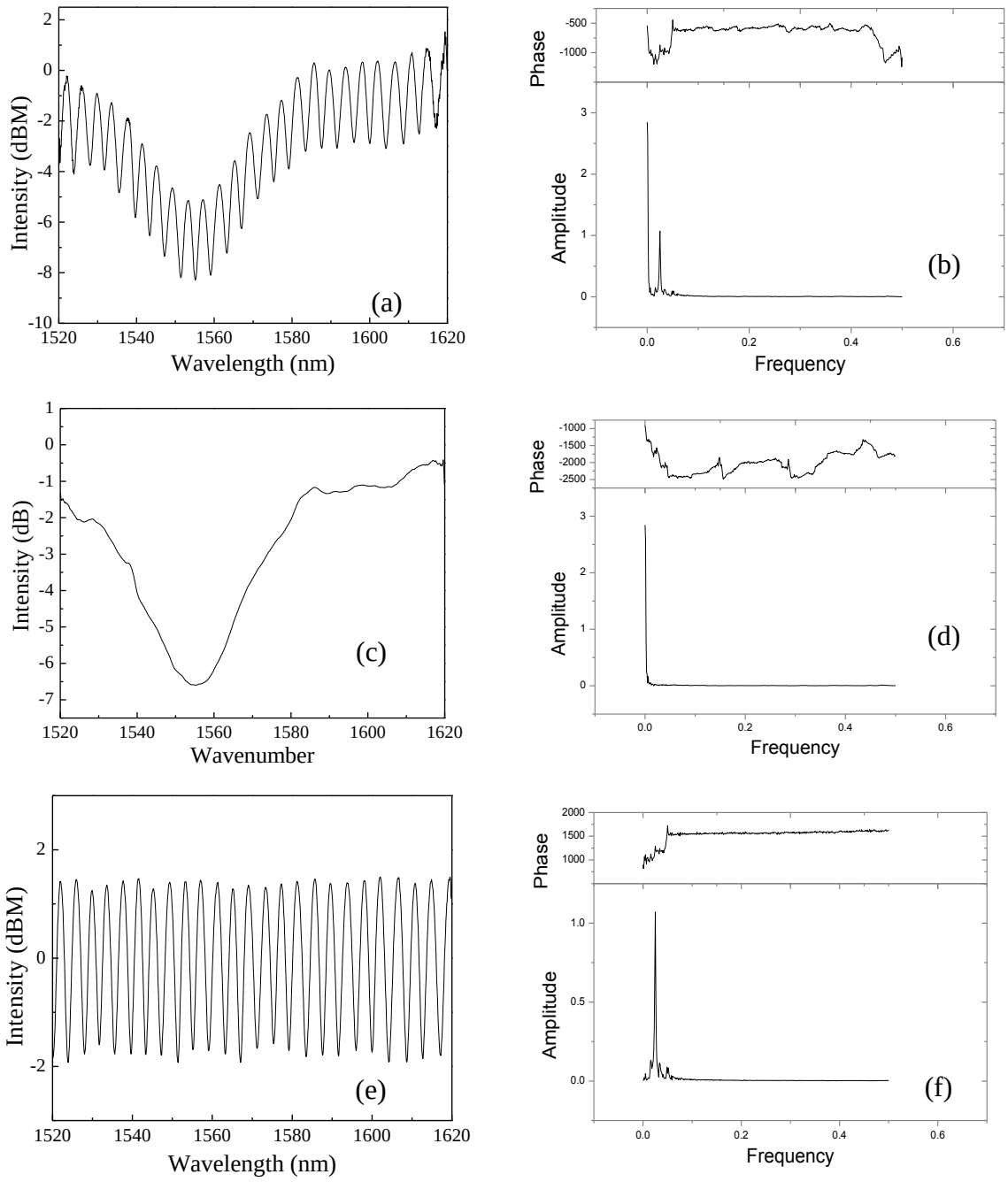

Figure 3.22 A hybrid EFPI/LPFG sensor with an EFPI cavity of 265 μm and its FFT prior to and after the use of a low-pass filter: (a) transmission spectrum, (b) FFT of the transmission spectrum in wave-number space, (c) LPFG spectrum after low-pass filtering, (d) FFT of the LPFG spectrum, (e) EFPI spectrum after high-pass filtering, and (f) FFT of the EFPI spectrum

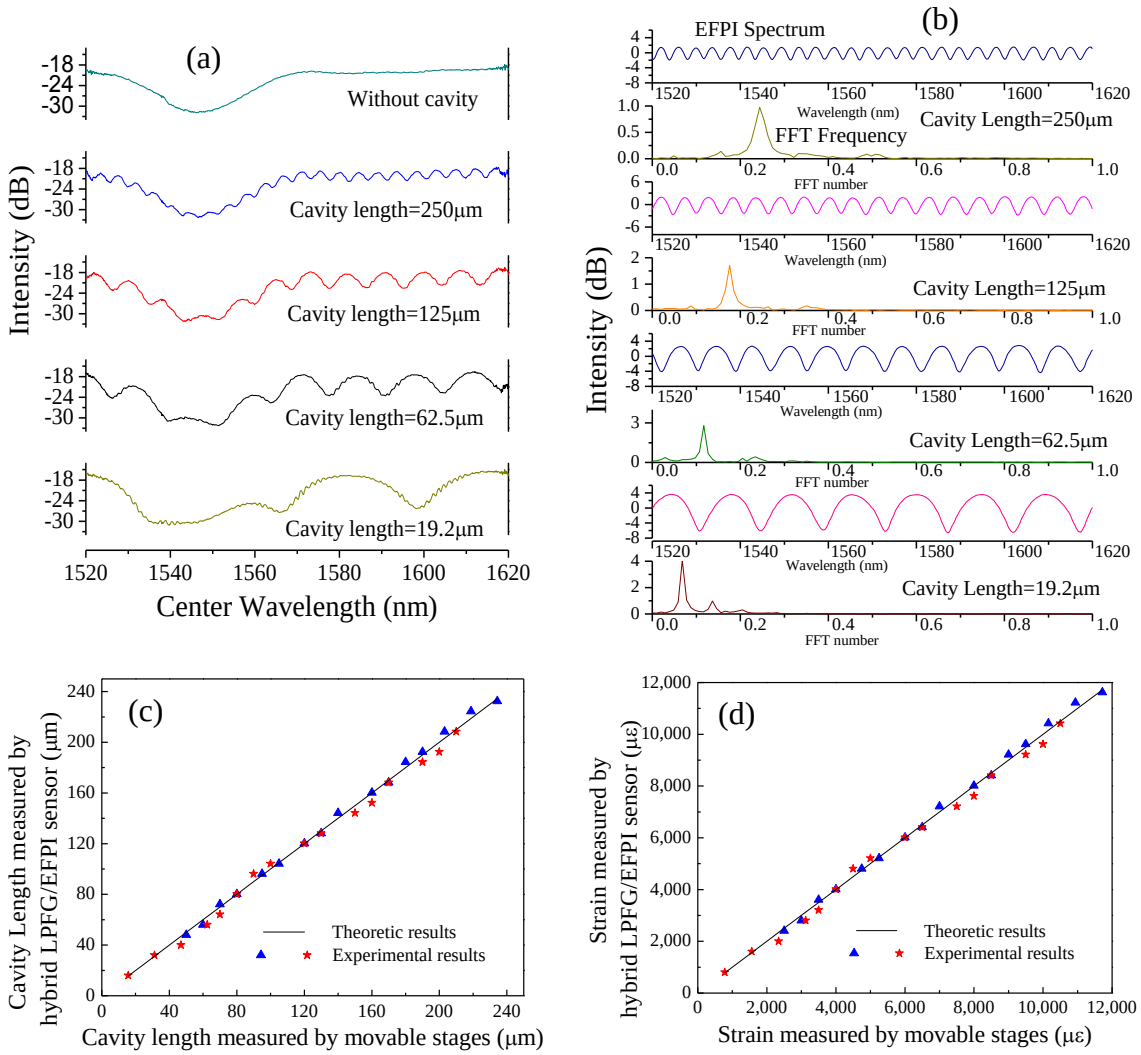

Figure 3.23 Strain measurement with a hybrid EFPI/LPFG sensor: (a) EFPI/LPFG spectra at various EFPI cavity lengths, (b) EFPI spectra and corresponding FFT spectra, (c) measured versus exact cavity length from spectral change and two movable stages, (d) measured versus exact strain from spectral change and two movable stages

3.3.3.2. Temperature sensing. To understand the temperature sensitivity of hybrid EFPI/LPFG sensors, a hybrid sensor prototype was tested for various temperatures up to 250 ℃ (482 ℉) under an unchanged cavity length of 200 μm. Temperatures were regulated at a gradient of approximately 1~2 ℃/min (1.8~3.6 ℉) with a high temperature furnace that was made by Thermo Electron Corporation. Figure 3.24 (a) shows spectral changes of the hybrid EFPI/LPFG sensor at various temperatures. Figure 3.24 (b) presents the temperature sensitivity of the sensor. As temperature increases, the center

wavelength of the LPFG linearly increases. The temperature sensitivity of the hybrid EFPI/LPFG sensor is approximately 0.041 nm/℃, which is 100 times higher than its corresponding strain sensitivity (5×10^{-4}nm/με [33]). Compared to the high temperature sensitivity, the strain effect on the LPFG can be neglected in high temperature conditions.

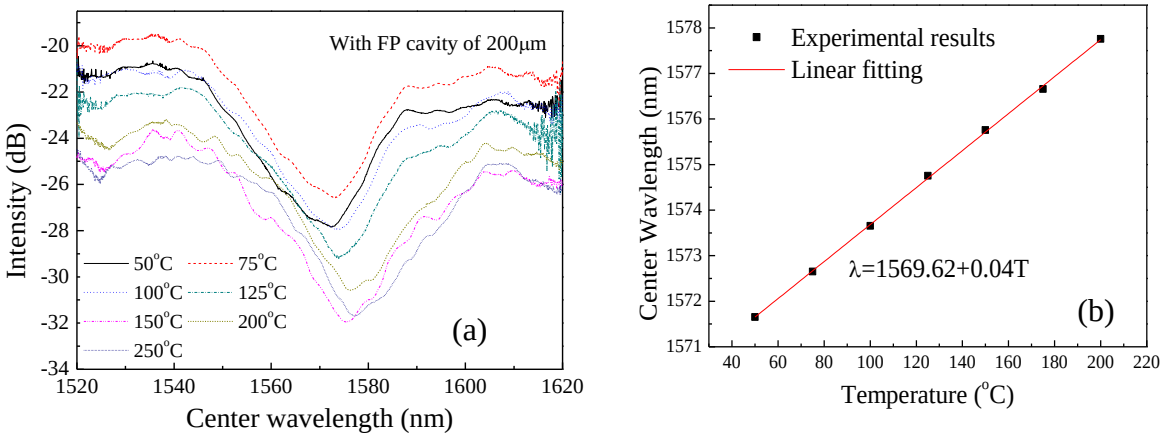

Figure 3.24 Temperature measurement of a EFPI/LPFG sensor: (a) transmission spectral change with temperature and (b) temperature sensitivity

3.3.3.3. Simultaneous large strain and high temperature measurement. The hybrid LPFG/EFPI sensor can measure a cavity length change of up to 260 μm, corresponding to a strain of 12% over a gauge length of 2 mm (0.08 in.), and temperature as high as 700 ℃ (1292 ℉). Experiments were performed on a hybrid EFPI/LPFG for simultaneous strain and temperature measurements. The hybrid sensor was installed on two steel channels of 2 mm apart, which were fixed on two computer controlled precise stages. The steel channels together with the hybrid sensor were placed inside the high temperature furnace for various tests. At a fixed cavity length of 200 μm, the low-pass filtered spectra of the hybrid EFPI/LPFG sensor are presented in Figure 3.25 (a) as temperature increases from 100 to 500 ℃. The corresponding center wavelength of the LPFG component is plotted as a function of temperature in Figure 3.25 (b). As shown in Figure 3.25 (c), the strains determined from the EFPI component of the hybrid sensor are correlated with the exact strains based on the precise distance between the two stages. Overall, the hybrid EFPI/LPFG sensor worked well till 700 ℃ (1292 ℉) and the difference between the strain calculated from the interference FFT frequency method and

that from the movable stages was within 5%, which is acceptable for large strain measurement. Figure 3.25 (c) also illustrates that the temperature effect on the EFPI signal was small and insignificant.

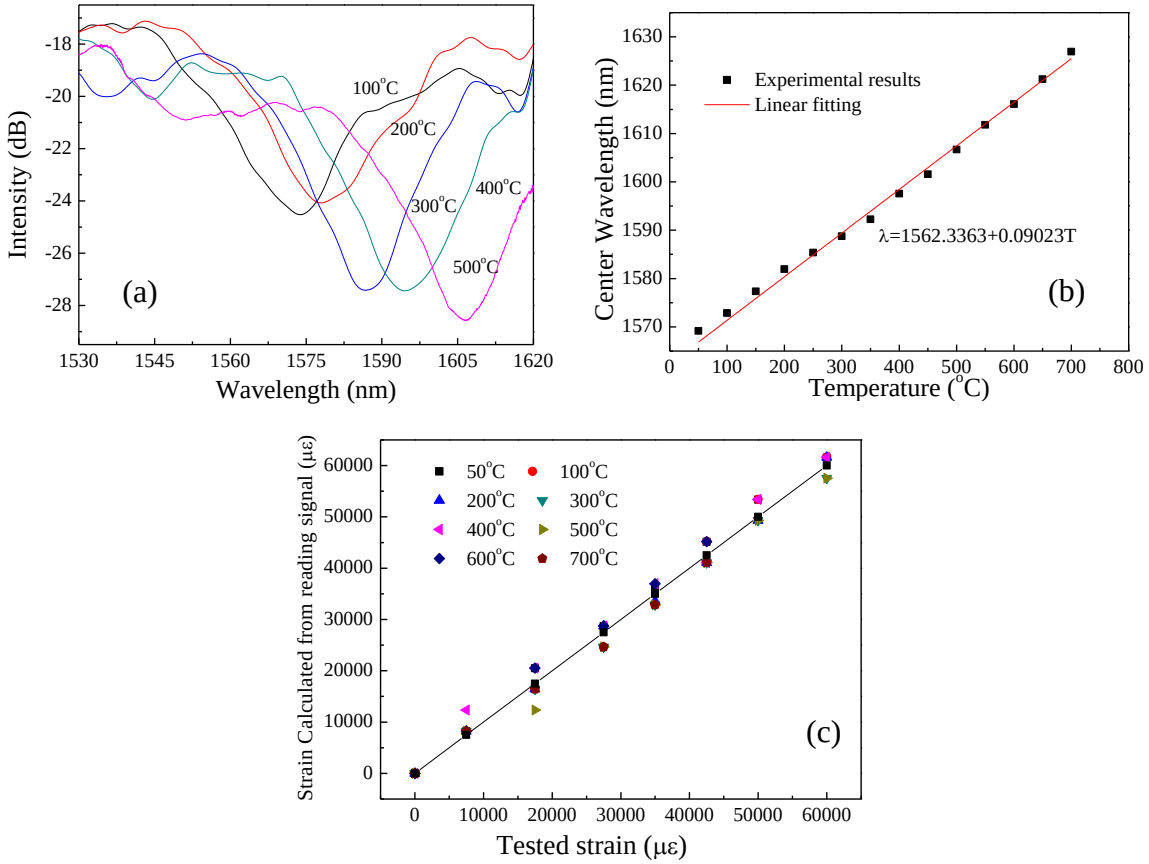

Figure 3.25 Experimental results from a hybrid EFPI/LPFG sensor prototype: (a) spectral change with temperature, (b) correlation between the central wavelength and the applied temperature, and (c) measured versus exact strain at various temperatures

3.4. SUMMARY ABOUT LARGE STRAIN AND HIGH TEMPEATURE MEASUREMENT

In this chapter, efforts were made to develop novel optical fiber sensors for simultaneous large strain and high temperature measurements in harsh environments. Two types of optical fiber sensors have been investigated for this application, including a single LPFG sensor and a hybrid EFPI/LPFG sensor. For each hybrid sensor, the LPFG

component is mainly for temperature measurement and the EFPI component is mainly for strain measurement.

The first type of LPFG sensors engaged with multiple packaging mechanisms for an increased strain measurement range. These mechanisms include the shear lag effect and the gauge length change effect. For the first time, two cladding modes of a LPFG sensor were used for multi-parameter sensing, e.g., for simultaneous strain and temperature measurement. The packaged single LPFG sensor has a dynamic strain range of up to 2.4% and a temperature sensing range of up to 700 ℃ (1292 ℉). However, for structural behavior monitoring of steel structures in harsh environments, such as post-earthquake fire conditions, the required dynamic range of strain measurements often exceeds 2.4%.

The second type of hybrid EFPI/LPFG sensors combines the complementary functions of LPFG and EFPI sensors. To measure temperature and strain at the same location, the distance between LPFG and EFPI components is taken to be less than 5 cm. In this case, the transmission signal of a hybrid sensor represents the coupled effect of its two components. The LPFG sensor information can be demodulated by a low-pass filter from the couple EFPI/LPFG signal. The proposed hybrid sensor can measure a strain of up to 120,000 με at 800 ℃ with strain resolution of 6,000 με, which is considerably superior to the packaged single LPFG sensor. Either LPFG sensors or hybrid EFPI/LPFG sensors can be applied to simultaneously determine strain and temperature with appropriate multiplexing of sensors.

4. SENSOR NETWORKING AND EXPERIMENTAL VALIDATION IN SIMULATED POST-EARTHQUAKE FIRE ENVIRONMENTS

4.1. INTRODUCTION

Fiber optic sensors are characterized by their unique sensitivity, compactness, reliability, electromagnetic immunity, and low cost. They have already become a viable solution for real-world problems from physical to chemical sensing. For cost efficiency, many fiber optic sensors are multiplexed to form a sensor network in practical applications. For example, a number of fiber optic sensors are required for the evaluation of a multitude of structural behaviors in civil infrastructure. Ideally, a multiplexed sensor network should include one input and one output fiber. It registers critical information on the sensing physical parameters of all sensors in various wavelengths, transmits the information from the sensors through the optical fiber to a detector, and demodulates the conveyed information from all sensors into a summation of data from individual sensors. However, multiple input and output fibers in array may be required to make a sensor network more cost effective in engineering practice. In addition, an array sensor network often provides the required redundancy and improves the reliability of the sensing system if some sensors or part of the network are damaged in harsh environments.

Many sensor networks with LPFG, EFPI, and hybrid EFPI/LPFG sensors and their applications have recently been developed for multi-parameter monitoring. Although widely applied for strain, temperature, and chemical measurements, EFPI sensors are difficult to multiplex due to limited cavity lengths that can be used in demodulation. In the past thirty years, more than six multiplexing methods have been investigated for interferometric sensor arrays. These methods include the frequency-division multiplexing (FDM) [119], spatial-frequency multiplexing (SFDM) [120, 121], wavelength-division multiplexing (WDM) [119, 120], time-division multiplexing (TDM) [122], coherence multiplexing (CM) [123], code-division multiplexing (CDM) [124], and their combinations. Table 4.1 compares the multiplexing methods. Good combinations are needed for a perfect sensor networking of EFPI involved sensing system.

Table 4.1 Comparison of available sensor multiplexing methods

Multiplexing Methods	Advantages	Disadvantages	Remarks
FDM	Simple concept, easy data processing, ability to detect same cavity length from various sensors	More than one laser and one detector needed, high cost	Not affordable in most cases
SFDM	Simple concept, cost efficiency, easy data processing, one laser and one detector needed	Different cavity lengths required, Amplification of receiving signals required	Infeasible to achieve different cavity lengths in application
WDM	Simple concept, cost efficiency, easy data processing, one laser and one detector needed, ability to detect same cavity length from various sensors	Relatively broadband light source required, limited number of sensors	Large broadband source limited
Combined SFDM/WDM	One laser and one detector needed, cost efficiency, ability to handle a large number of sensors	Different cavity lengths required, Amplification of receiving signals required, relatively broadband light source required, limited number of sensors	Large broadband source limited, Infeasible to achieve different cavity lengths in application
TDM	One laser and one detector needed, cost efficiency, ability to handle a large number of sensors	Long optical path required, hard to implement	Hard to achieve long optical path differences
Combined TDM/WDM	One laser and one detector needed, cost efficiency, ability to handle a large number of sensors, ability to detect same cavity length from various sensors	Long optical path required, hard to implement, broadband light source required	Large broadband source limited, hard to achieve long optical path differences
Combined TDM/FDM	Simple concept, ability to detect same cavity length from various sensors	More than one laser and one detector needed, high cost, long optical path required	High cost, hard to achieve long optical path differences
CM	One laser and one detector needed, ability to handle a large number of sensors	Coherence light source required	Coherence light source limited
CDM	Access to any frequency channel at any time, more efficient and flexible	Some self-jamming issues in coding, hard to select proper codes, complex data processing	Hard to implement codes in application

On the other hand, LPFG sensors can be multiplexed in line for sufficiently long distance and the WDM method can be readily applied to process test data. Based on the previous studies [101, 125], the cladding mode stripper between any two LPFG sensors must remain to ensure the workability of the LPFG sensors in series. In a high temperature range, e.g. 150 ℃, the initial coating of an optical fiber is about to disappear, which leaves an open area for the development of new bafflers between the LPFG sensors. In addition, TDM [122] can be applied for LPFG sensors as needed.

EFPI and LPFG sensors are conventionally implemented separately with different optical fibers and integrated by optical switches either manually or automatically. In this case, each kind of sensors uses one optical fiber, making the sensor multiplexing complicated and associated network low in efficiency. To simplify a sensor network, Rao et al. (2007) [118] proposed to combine micro EFPI and LPFG sensors by simply assembling each kind of the sensors together. Their experimental results showed that the two kinds of sensors would not affect each other since EFPI is dominated by reflection and LPFG is by transmission. This opens a door for further research on multiplexing of EFPI and LPFG sensors. However, one EFPI and one LPFG sensor in one optical line is insufficient for a network of numerous sensors.

In this study, an effort is made to investigate an alternate network of EFPI and LPFG sensors or integrated EFPI/LPFG sensors. The multiplexed sensors are implemented in laboratory testing of a one-story, one-bay steel frame structure under simulated post-earthquake fire conditions. The test setup, procedure, and results of the networked sensors are discussed in this chapter. Various optical fiber sensors are compared with commercial sensing devices to validate their performance.

4.2. OPTICAL FIBER SENSOR NETWORKING

Built upon the previous multiplexing technologies, a network of hybrid EFPI/LPFG sensors is investigated for simultaneous high temperature and large strain measurements using the SFDM and WDM methods. Preliminary experiments demonstrated that the proposed network of two hybrid EFPI/LPFG sensors can simultaneously measure high temperatures and large strains at two locations. If two 1×N

couplers are used, the number of hybrid EFPI/LPFG sensors can be increased to N, resulting in a cost-effective optical fiber sensing system for structural health monitoring.

4.2.1. Sensor Network Design. Figure 4.1 shows a representative multiplexing network of hybrid EFPI/LPFG sensors. As shown in the insert of Figure 4.1, two EFPI/LPFG sensors are connected by two 1×2 couplers in parallel. Light coming out of the broadband source is first branched into two parts at the first 1×2 coupler to each hybrid sensor and then combined at the second 1×2 coupler to the Optical Signal Analyzer (OSA). The OSA is further connected to a personal computer for data processing to demodulate the recorded signal for the critical information carried by multiple LPFG and EFPI sensors in the multiplexing network. To distinguish the signal components from an LPFG sensor and an EFPI sensor in the network system, the wavelengths among LPFG sensors and the initial cavity lengths among EFPI sensors must be significantly different. With an 8-channel optic switcher, 16 key locations can be monitored on the critical structures for simultaneous large strain and high temperature. If more sensors are needed, two 1×N couplers can be used in the multiplexing system to have 8×N sensors deployed on a critical structure for structural behavior monitoring.

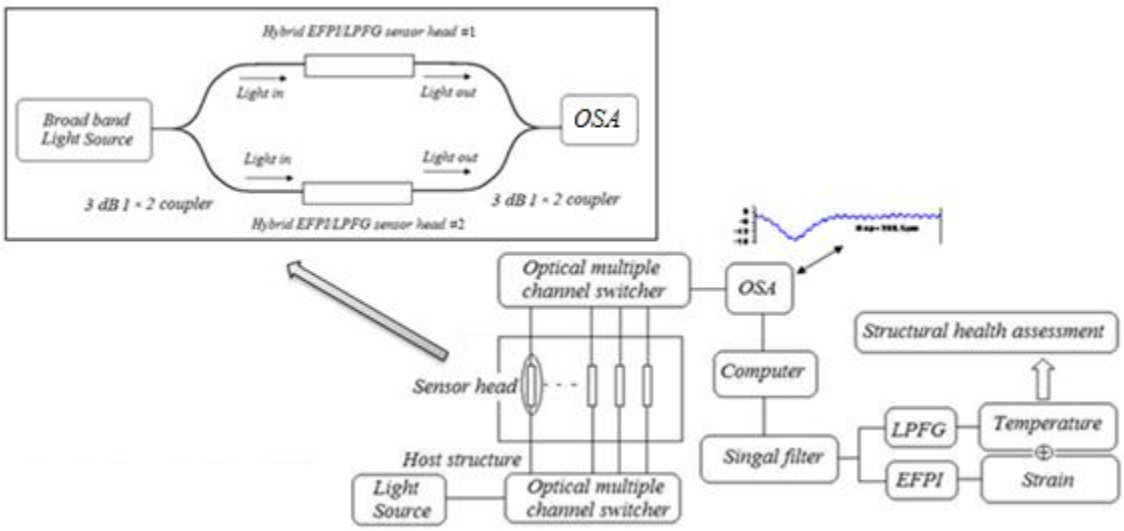

Figure 4.1 Schematic of an optical fiber network of hybrid EFPI/LPFG sensors

4.2.2. Primary Validation Test. To demonstrate the feasibility of the proposed sensor network, two hybrid EFPI/LPFG sensors were connected by two 1×2 couplers as illustrated in Figure 4.1 (insert), each having an LPFG component and an EFPI component. The individual spectra of the two separate hybrid sensors are shown in Figure 4.2 (a) while their combined spectrum is presented in Figure 4.2 (b). The center wavelengths of the two LPFG components were set to differ by 10 nm. The initial cavity lengths of the two EFPI components were set to 20 μm and 60 μm, respectively. The sensors in the network were installed on the same stage as used in the previous tests. When the stage generates a relative displacement of 40 μm on the optical fibers, the measurements from the sensor network are plotted in Figure 4.2 (c). It can be seen from Figure 4.2 (c) that the first peak represents a strain of 2.05% and the second peak gives 1.95%. The sensors provide consistent readings with a less than 5% difference for the same strain imposed by moving the stage. With the known spectral frequencies of both EFPI components, the spectrum of the network system can be filtered by a low-pass filter. The LPFG spectrum after the filtering is presented in Figure 4.2 (d). It can be seen that the LPFG components in the two hybrid sensors can be clearly distinguished and the sensor network is capable of high temperature measurement. Therefore, the proposed quasi-distributed optical network system based on hybrid EFPI/LPFG sensors worked well for simultaneous large strain and high temperature measurements at multiple locations.

Figure 4.2 (d) indicates that the use of two 1×2 couplers has successfully multiplexed two hybrid EFPI/LPFG sensors into the simple sensor network. The tested network can be expanded to include more sensors as needed by combining N hybrid LPFG sensors for simultaneous large strain and high temperature measurements. Such a network can potentially be applied to structural health monitoring under earthquake loads or in earthquake-induced fire environments where few traditional monitoring technologies can survive.

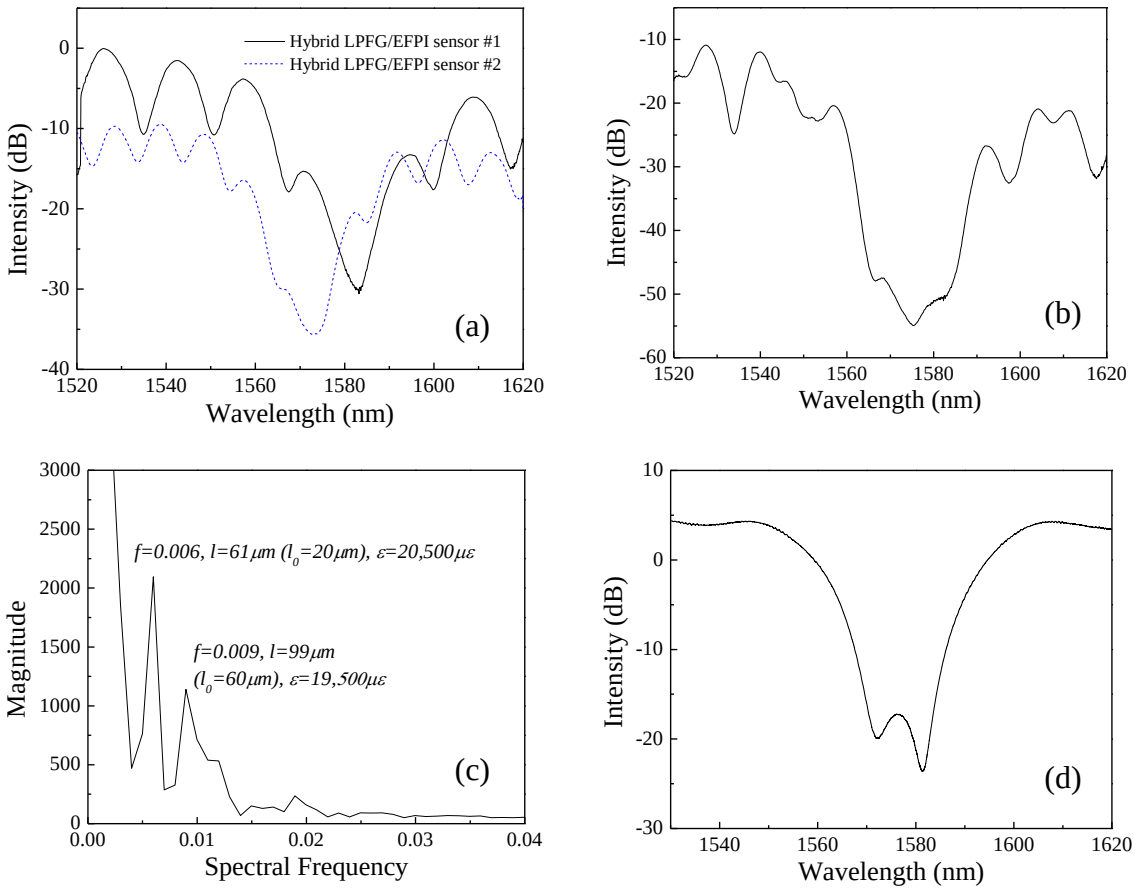

Figure 4.2 Performance of a multiplexed network of hybrid EFPI/LPFG sensors: (a) individual spectra of the two sensors, (b) transmission spectrum of the network, (c) FFT of the transmission spectrum in terms of wavenumber, and (d) LPFG spectrum after low-pass filter

4.3. EXPERIMENTAL VALIDATION UNDER SIMULATED POST-EARTHQUAKE FIRE CONDITIONS

4.3.1. Design of an Idealized Steel Frame. A frame of one top beam and two columns is considered in this study. The frame was made of A36 steel and built with hot-rolled S-shapes as shown in Figure 4.3. To illustrate a potential switch of failure modes from one column to another under earthquake and post-earthquake fire loadings, respectively, a substructure of the frame consisting of one column (#1 in Figure 4.3) and the top beam was tested under a static lateral load to simulate earthquake effects and the

entire frame with two identical columns was tested with the other column (#2 in Figure 4.3) placed in a high temperature environment to represent post-earthquake fire effects. The former is referred to as an L-shaped frame and the latter is referred to as a two-column frame for clarity in the following discussion.

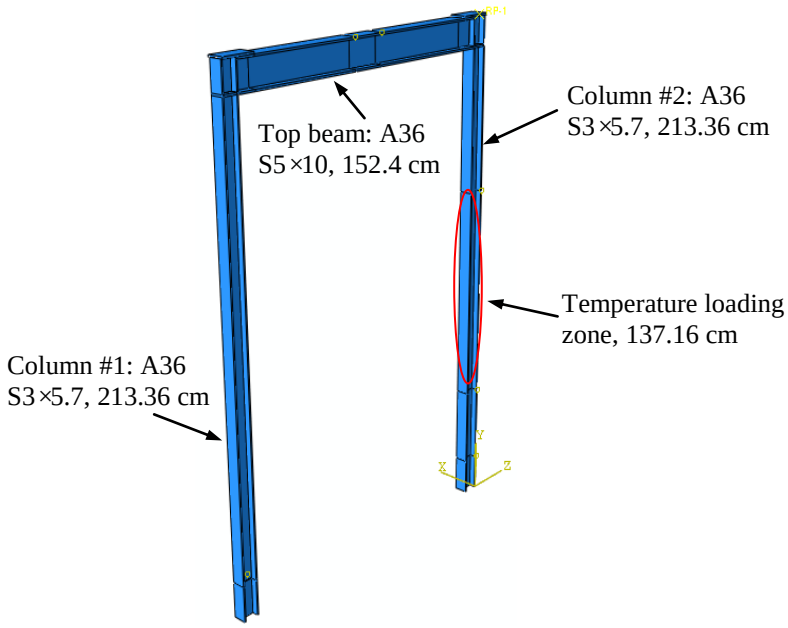

Figure 4.3 Rendering of the steel frame

The dimensions of the steel columns were determined based on the size of an electric furnace (Lindberg/Blue M Tube Furnaces) used to simulate the high temperature effect of post-earthquake fires on the progressive collapse of the frame structure. The overall dimension of the furnace used for testing is 55.9×137.2×66 cm (22×54×16 in.) with an actual heating zone of 91.4 cm (36 in.) in length and an inner diameter of 15.24 cm (6 in.). Considering additional spaces required for the assembling (welding of stiffeners, beam-column joint, and column-tube connection) of the two-column frame after column #2 has been placed through the round furnace, the length of the columns was selected to be 213.4 cm (84 in.). To provide a sufficient space for frame deformation at high temperature, the columns of the steel frame were selected as S3×5.7, which has a flange width of 7.62 cm (3 in.) and a height of 10.16 cm (4 in.). To design a rigid beam, the stiffness of the top beam was set at least 5 times that of each column. As such, a hot-rolled S5×10 beam was selected. Since the anchors on the strong floor in the structures

laboratory are spaced 91.44 cm (36 in.) apart, the length of the top beam was selected to be 142.2 cm (56 in.), which is equal to the anchor spacing plus the width of one bolted plate on the floor and twice the width of an angle stiffener. To ensure a rigid beam-column connection, three stiffeners were provided on each column: a 7.62×30.48×1.27 cm (3×12×0.5 in.) stiffener placed on the top cross section of the column, and two 3.556×9.9×1.27 cm (1.4×3.9×0.5 in.) stiffeners placed between the two flanges of the column on two sides of the column web, extending the bottom flange of the beam. Stiffeners were welded to the steel frame at the beam-column connection. The overall design of the steel frame is shown in Figure 4.3. The column subjected to earthquake effects only is referred to as Column #1 while the other column directly subjected to earthquake-induced fire effects is referred to as Column #2.

4.3.2. L-Shaped Steel Frame and Earthquake-Induced Damage.

4.3.2.1. Test setup and instrumentation under lateral loading. To simulate earthquake damage of the steel frame (Column #1 only), Column #1 and the top beam was placed on the strong floor and subjected to cyclic loading. Figure 4.4 shows the test setup of the L-shaped frame and its prototype in the inset. The L-shaped frame was welded on a steel tube of 15.24×15.24×335 cm (6×6×132 in.) with 1.27 cm (½ in.) wall thickness. In addition, two triangle brackets were individually welded to the two flanges of the column and the square tube to ensure a rigid connection between the column and the tube. The square tube was anchored into the strong floor at four anchor locations. To prevent it from experiencing large deformation, the square tube was stiffened near the base of the column by three stiffener plates of 30.48×13.94×1.27 cm (12×5.5×0.5 in.). The stiffeners were welded on the three sides of the square tube: column base face and two side faces. To approximately represent the two-column frame behaviour, the free end of the top beam was transversely restrained by a roller-type support. A cyclic load was applied to the top of the column or the top beam by means of a hydraulic actuator. The applied load was measured by a 5-kip load cell installed between the actuator and the frame. To monitor the structural behaviour under the cyclic load, 15 conventional strain gauges were deployed and distributed along the column and the beam as located in Figure 4.4. They are designated with a prefix of SG#. For example, SG#1 means the strain gauge

#1 that was deployed to monitor the strain in the column-to-tube connection. Similarly, SG#12 was used to assess the beam-column joint condition. In addition, two linear variable differential transformers (LVDTs) were respectively deployed 20.32 cm (8 in.) above the column base and 35.56 cm (14 in.) below the bottom flange of the top beam. LVDT#1 was deployed at the bottom of the column to ensure that the column is not displaced during testing. LVDT#2 was deployed at this location for convenience.

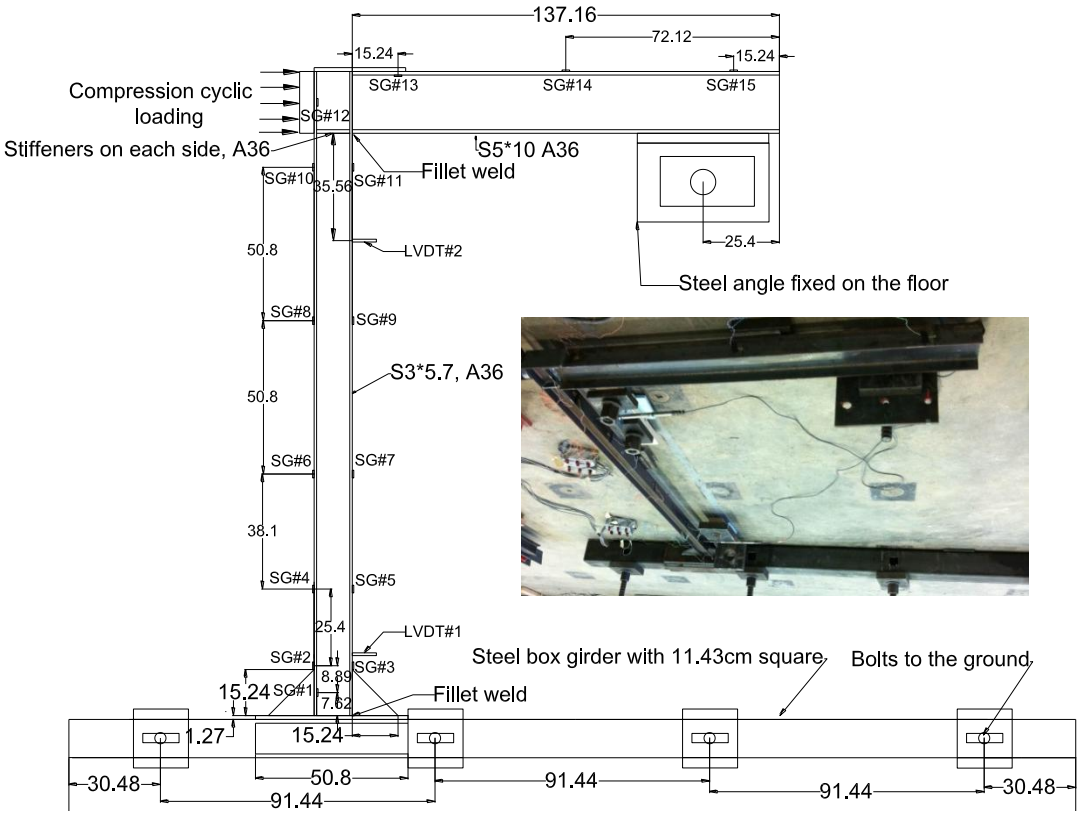

Figure 4.4 Test setup and instrumentation of the L-shaped steel frame with a prototype inset (unit: cm)

4.3.2.2. Loading protocol and simulated earthquake damage. Figure 4.5 presents the cyclic loading protocol, measured strains and displacements of the L-shaped frame structure. As shown in Figure 4.5 (a), five cycles of loading were applied to the frame following a saw-teeth pattern. The first four cycles of loading reached 15.1 kN (3.4 kips) at which the column expects to experience initial yielding, and the last cycle reached 16.9 kN (3.8 kips) to ensure that the column is subject to inelastic deformation.

For all cycles, the frame structure was loaded and then unloaded at a rate of -24.29 N/sec (-5.46 lb/sec) and -48.57 N/sec (-10.92 lb/sec), respectively.

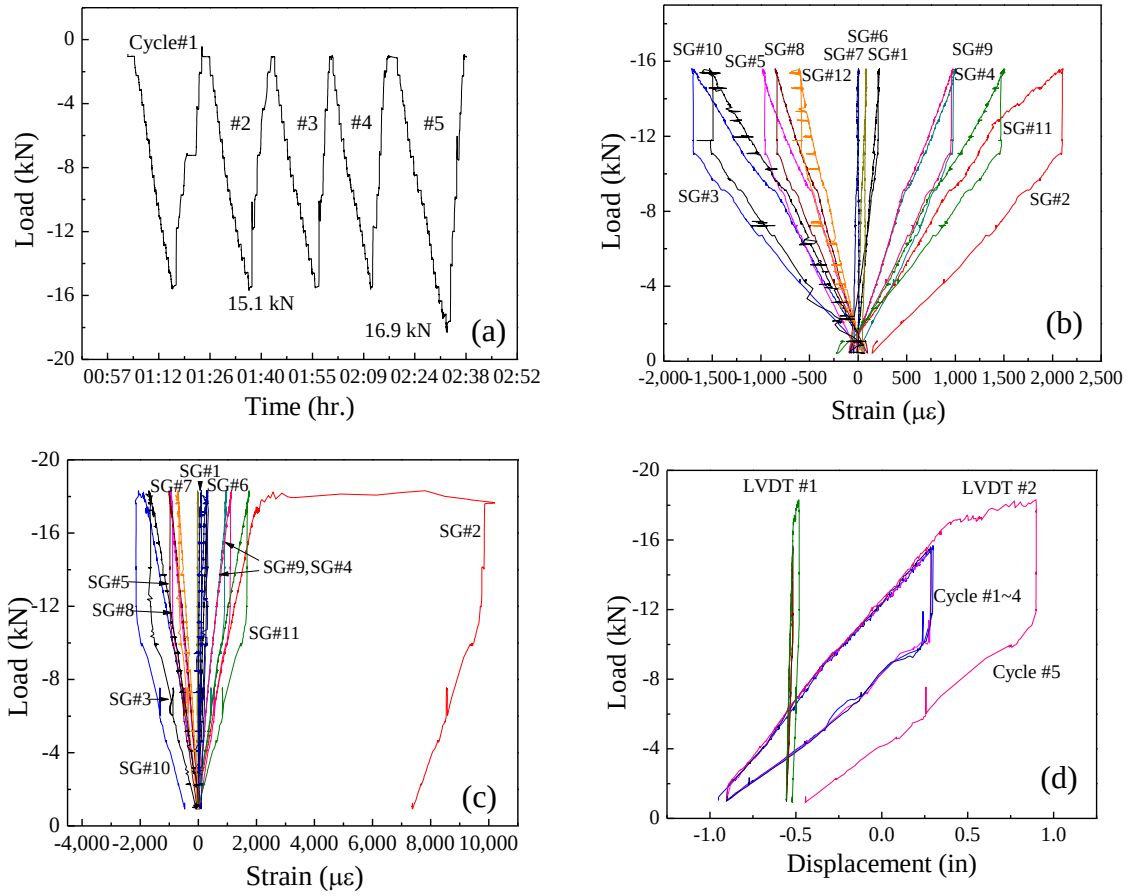

Figure 4.5 Test results: (a) loading protocol, (b) load-strain relations for cycle #1-4, (c) load-strain relations for cycle #5, and (d) load-displacement relations

The measured strains (raw data) of the column are presented as a function of the applied load in Figure 4.5 (b) during the first four cycles of loading and in Figure 4.5 (c) during the last cycle. For the first four loading cycles, the maximum strain at the bottom of the column (SG#2) was approximately 0.2%, indicating initial yielding of the test frame. For the fifth cycle, the strain reached 1% as the load was held at 16.9 kN (3.8 kips) for a few seconds. After unloading, a permanent strain of 0.75% remained at the column base (SG#2). Throughout the tests, the maximum strains in the beam-column and column-tube connection areas are both insignificant due to their significantly stronger

designs than that of the column member. The maximum strains at locations slightly away from the connection areas are the highest as shown in Figure 4.6 for strain distributions along the height of the column (outside face) during the first four cycles and the fifth cycle of loading. It can be clearly observed from Figure 4.6 that Column #1 was subject to double curvatures with a zero strain at 50.8 cm (20 in.) to 76.2 cm (30 in.) above the column base. The extent of inelastic deformation was mainly limited to the bottom portion of the column.

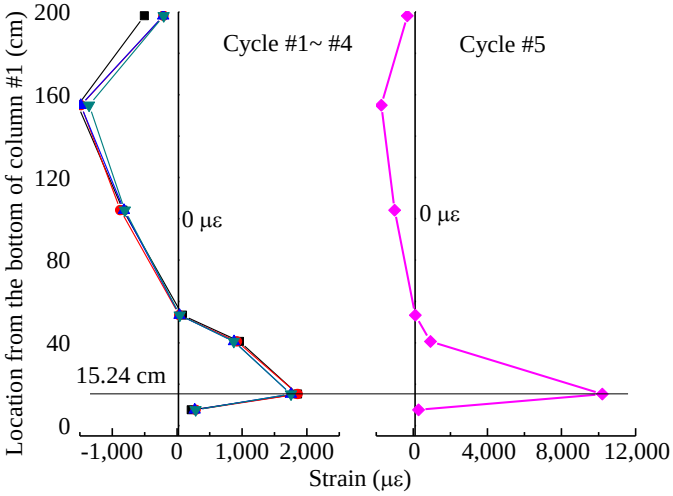

Figure 4.6 Distribution of the maximum strains along the column height

The displacement change with load is presented in Figure 4.5 (d) in various loading cycles. It can be observed from Figure 4.5 (d) that the displacement change from LVDT#1 is negligible, indicating that the frame base was basically fixed to the strong floor. The largest displacement of 4.572 cm (1.8 in.) was observed at the top of the column (location of LVDT#2), leaving behind 1.27 cm (0.5 in.) permanent deformation in the column when unloaded. The permanent plastic strain and deformation introduced by the cyclic loading represented a large strain condition that can be induced by an earthquake event.

4.3.3. Comprehensive Sensing Networks. To closely monitor the structural behavior of the entire steel frame, two comprehensive sensing networks of the developed

novel optical fiber sensors and commercial sensors were applied to the frame structure, as shown in Figure 4.7. The novel optical sensors developed in the Chapters 2 and 3 were deployed on the column that experienced simulated fire heating effects. The optical sensors were placed both inside and outside the furnace for the structural behavior assessment of the steel frame in post-earthquake fire environments. The optical fiber sensor system is composed of long period fiber gratings (LPFG) and fiber Bragg gratings (FBG), and extrinsic Fabry-Perot interferometer (EFPI) based large strain sensors, as well as the improved hybrid EFPI/LPFG sensors for simultaneous measurements of high temperature and large strain. To validate the proposed optical fiber sensing network, commercial sensors were also installed on the steel frame, including both conventional and high temperature endurable strain gauges for strain measurement and thermocouples for temperature measurement as also shown in Figure 4.7.

4.3.3.1. Optical fiber based sensing network. Due to the harsh condition in a post-earthquake fire environment, most conventional strain gauges do not work appropriately. Therefore, optical fiber sensors were proposed to assess the structural behavior of the steel frame under this condition. For large strain sensing in high temperature environments, a movable EFPI sensor was proposed as discussed in Chapter 2. For simultaneous large strain and high temperature measurements, hybrid optical sensors based on movable EFPI and LPFG principles were introduced in Chapter 3. The optical sensing system included two LPFG high temperature sensors, one FBG temperature sensor, five movable EFPI large strain sensors, and two hybrid EFPI/LPFG sensors. Figure 4.8 and Figure 4.9 (a) show the sensor layout on Column #2, on which the majority of optical fiber sensors were attached. In Figure 4.9 (a), blue circles represent the locations of EFPI sensors, red circles represent the locations of hybrid EFPI/LPFG sensors, the purple circle represents the location of the FBG sensor and the yellow circle illustrates the locations of the LPFG sensors. Three movable EFPI sensors were placed on the two ends of the furnace, and the fourth one was placed at the 1/3 length from the bottom of the furnace. One hybrid EFPI/LPFG was placed on the bottom of the furnace and the other was placed at the 2/3 length from the bottom the furnace together with one movable EFPI sensor. One LPFG temperature sensor was placed on Column #2 at the top of furnace and the other was placed on the base of Column #1. Figure 4.9 (b) shows the

details of sensor installation. Ceramic high temperature adhesives that can endure up to 1100 ℃ (2012 ℉) was applied to attach the optical sensors to the inside face of the column flanges.

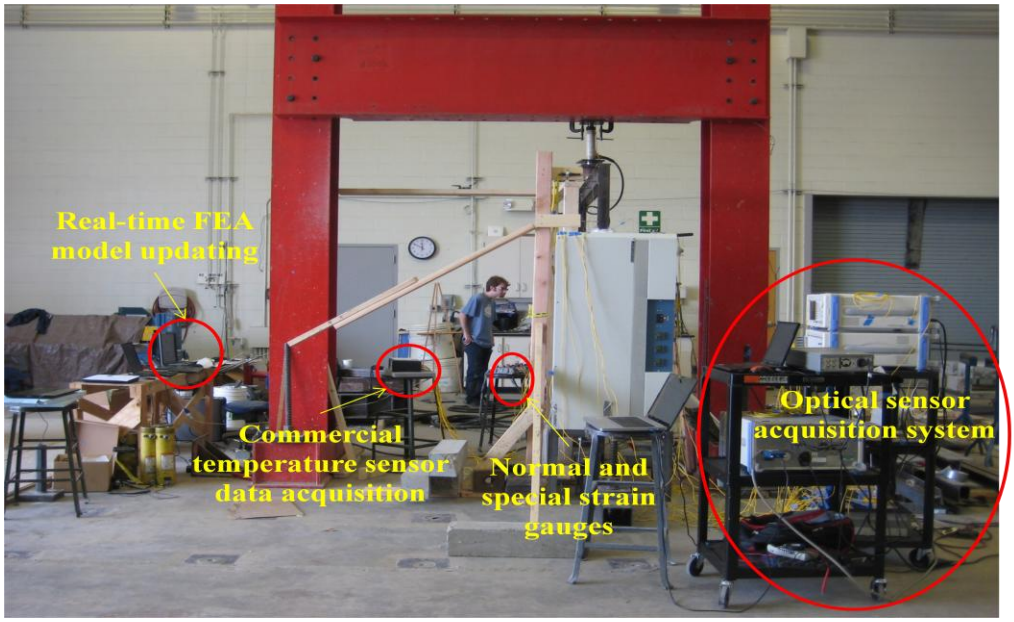

Figure 4.7 Sensing systems and network

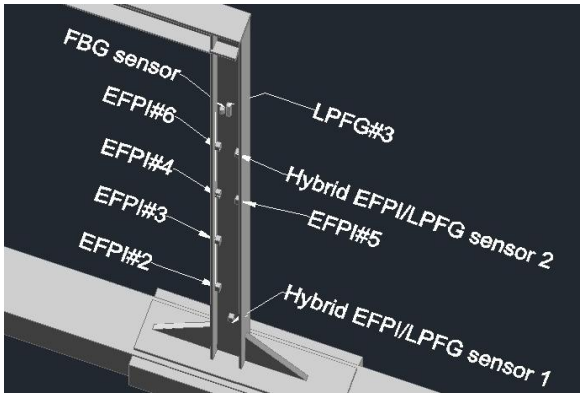

Figure 4.8 Specific locations of fiber optical sensors in three-dimensional view

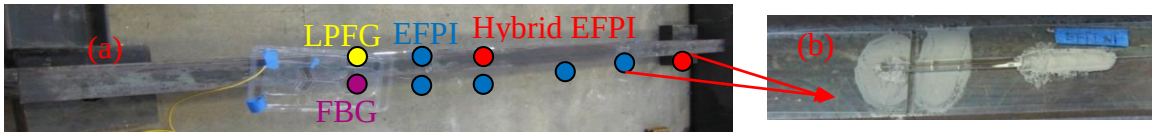

Figure 4.9 Detailed sensor installation: (a) optical sensor layout and (b) the installed optical sensor and thermocouple

4.3.3.1.1. LPFG based high temperature sensing system. All the LPFG sensors used in this study were fabricated as described in [102]. The sensitivity of the LP_{05} of the LPFG sensor (monitored in this test) towards temperature change is approximately 0.08 nm/℃, as shown in Figure 4.10 (a). In the simulated post-earthquake fire test, two LPFGs were attached on the steel frame. One was right above the furnace which was shown by the yellow circle in Figure 4.10 (a) and the other was located at the bottom of Column #1. The two LPFG sensors were connected to an optical signal spectrometry (supplied by Advantest with a series of Q8460), which was further connected to a personal computer. The optical signal spectrometry has four channels, providing both the light source and the data recording of the sensing system. A combined program of Labview and Matlab was developed on the personal computer to record the grating spectrum, transfer the spectrum to the required resonant wavelength, and further produce the temperature change in real time.

4.3.3.1.2. FBG based temperature sensing system. FBG temperature sensors and sensor arrays have been widely applied in harsh environments. Although FBG sensors are often related to a permanent modulation of refractive index in fiber core, their exposure to a high-temperature environment usually results in a bleach of the refractive index modulation. The maximum temperature reported in various FBG sensor applications is approximately 600 °(1112 ℉) due to its weak bond of germanium and oxygen [126]. Thus, in the simulated fire test, one FBG sensor was attached to the column at the top of the furnace as indicated by the purple circle in Figure 4.10 (a), where it was expected to experience the highest temperature within the FBG measuring limit. Figure 4.10 (b) shows a temperature sensitivity of 11pm/℃ for an FBG sensor. Data from the FBG sensors were collected by an optical sensing integrator (OSI) SM125 (Micron Optics, Inc) with a record rate of 1/sec. A Matlab program was developed to transfer the recorded resonant wavelength of the FBG to the required temperature information in real time.

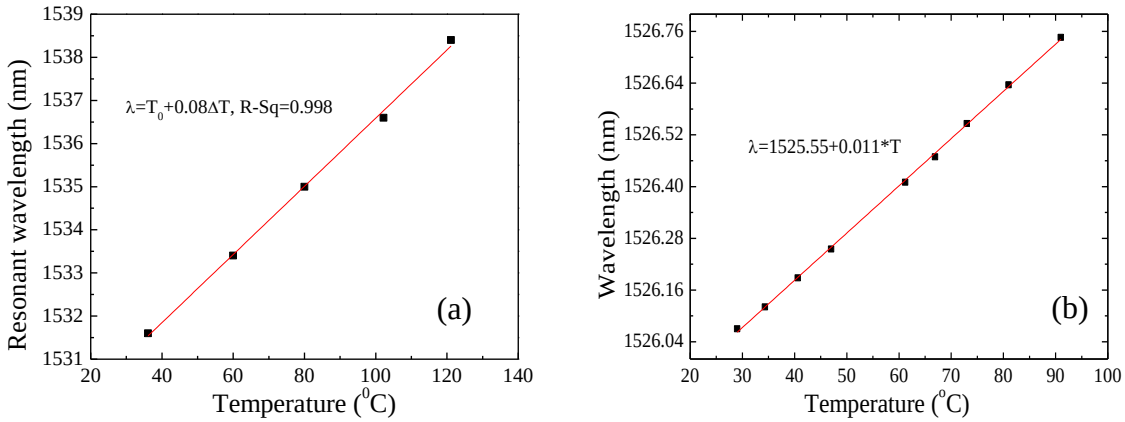

Figure 4.10 Optical fiber temperature sensors: (a) LPFG and (b) FBG

4.3.3.1.3. <u>Movable EFPI based large strain sensing system.</u> As stated in Chapter 2, the rugged movable EFPI sensor can measure strain up to 12%. Figure 4.11 (a) shows the reflected optical spectrum of the EFPI with various cavity lengths and Figure 4.11 (b) shows the calculated EFPI cavity length from the spectral change compared to the reference one measured with a microscope. In the simulated post-earthquake fire test, five large strain movable EFPI sensors were attached to Column #2 inside the furnace for large strain monitoring in high temperature conditions. The specific locations of the five EFPI sensors inside the furnace were represented by the blue circles in Figure 4.9 (a). One 400 nm tunable laser system (produced by Agilent Technology with a series of 81600B) was applied to provide a light source for the movable EFPI sensors, and one optical signal analyzer (OSA, produced by YOKOGAWA with a series of AQ6373) was used as a real time data acquisition and recording. The light source and the OSA were then connected with the five sensors by a SB series 1×8 fiber optic switch (supplied by JDSU with a D configuration). The OSA was further connected to a personal computer with a combined Labview and Matlab program that was specifically written for this study to record the grating spectrum and analyze the recorded data for strain information in real time.

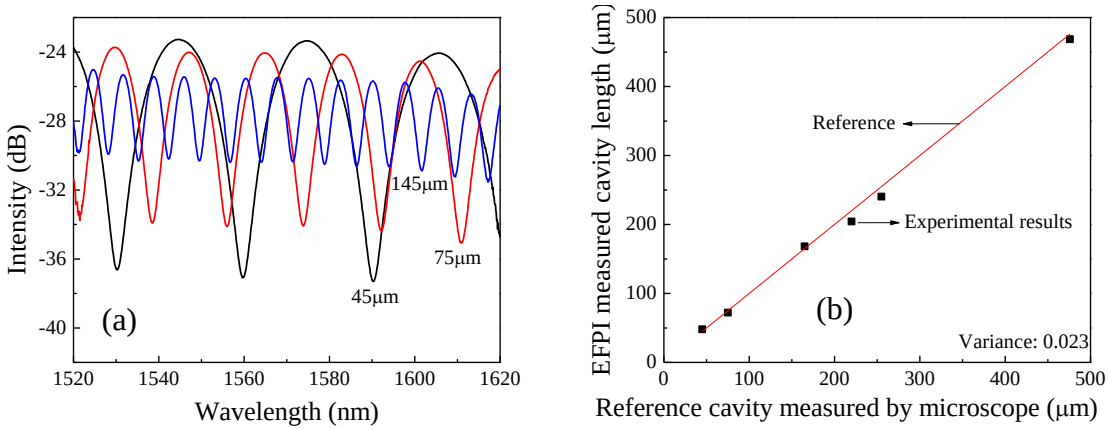

Figure 4.11EFPI based large strain sensing system: (a) spectral change of EFPI sensors with various strains and (b) calibrated results for an EFPI strain sensor

4.3.3.1.4. <u>Hybrid EFPI/LPFG sensing system for simultaneous large strain and high temperature measurement.</u> A sensing network is set up for the developed hybrid EFPI/LPFG sensor for simultaneous large strain and high temperature measurement. In the simulated post-earthquake fire test, two hybrid EFPI/LPFG sensors were attached to Column #2 inside the furnace. The specific locations of the two sensors are indicated by the red circles in Figure 4.9 (a). Figures 4.12 (a, b) show the strain accuracy and temperature sensitivity of a hybrid EFPI/LPFG sensor for simultaneous large strain and high temperature measurement.

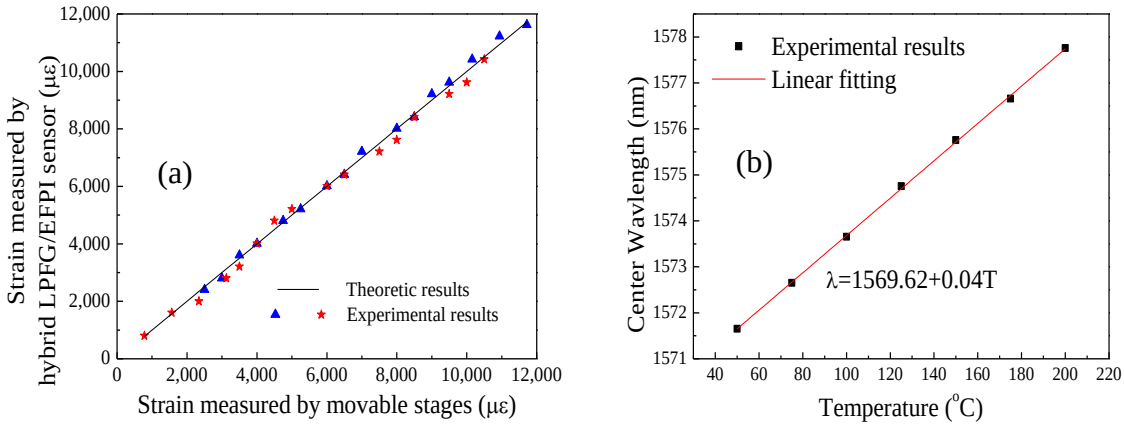

Figure 4.12 Hybrid EFPI/LPFG sensor: (a) Measured versus exact strains from the spectral signal and the movable stage, and (b) temperature sensitivity of the sensor

4.3.3.2. Commercial sensing network. To monitor the temperature distribution change along the steel frame, ten K-type thermocouples (manufactured by ThermoWorks with a series of heavy duty surface probe) were placed along the frame as illustrated in Figure 4.13. A 12-channel scanning thermocouple thermometer supplied by Diqi-Sense was used to acquire the temperature measurement in real time. For strain measurements, in addition to the 15 conventional strain gauges applied during the simulated earthquake loading, five high temperature endurable strain gauges (manufactured by Micro-Vichy) were attached along the top beam and Column #2 for strain monitoring in the simulated post-earthquake fire environment. Figure 4.13 shows a sensor layout of the high temperature strain gauges. These ZC-Series strain gauges are etched Kanthal (Fe-Cr-Al alloy) foil grids in free-filament form for high-temperature applications. They can measure up to 5,000 με. To compensate for the effect of temperature, a dummy gage needs to be deployed with a minimum thermally induced strain. In this study, the measured temperature was used to compensate for the temperature effect on the high temperature strain gauges. Nichrome ribbon leads at the end of high temperature strain gauges were welded to the wire leads. Since the soft Nichrome ribbon materials cannot hold the ZC-series gauges, special care must be exercised for their installation. A 24 channel strain gauge recorder was connected to the strain gauges to measure strain changes in real time.

4.3.4. Structural Behavior Evaluation of the Steel Frame.

4.3.4.1. Simulated post-earthquake fire environments. The furnace used to simulate the post-earthquake fire condition was supplied by Thermo Scientific with a series of Lindberg/Blue M Tube Furnace. It has three temperature zones that can be programmed and operated independently. In this study, the three temperature zones of the furnace were programmed to have the same temperature increase profile as shown in Figure 4.14 (a). The temperature increased from room temperature (20 ℃, 68 ℉) to 800 ℃ (1472 ℉) by an interval of 100 ℃ (180 ℉). Thus, the evaluated temperatures included are 20 ℃ (68 ℉), 100 ℃ (212 ℉), 200 ℃ (392 ℉), 300 ℃ (572 ℉), 400 ℃ (752 ℉), 500 ℃ (932 ℉), 600 ℃ (1112 ℉), 700 ℃ (1292 ℉), and 800 ℃ (1472 ℉). At each temperature level, the test was paused for 10 minutes to arrive at temperature stabilization

both inside and outside the furnace. Between two consecutive temperatures, a temperature increasing rate of 10 ℃/min (18 ℉/min) was utilized to simulate the fire induced high temperature conditions. Note that the test stopped for less than 2 min at 750 ℃ to ensure that the steel frame is still safe to take additional temperature loading.

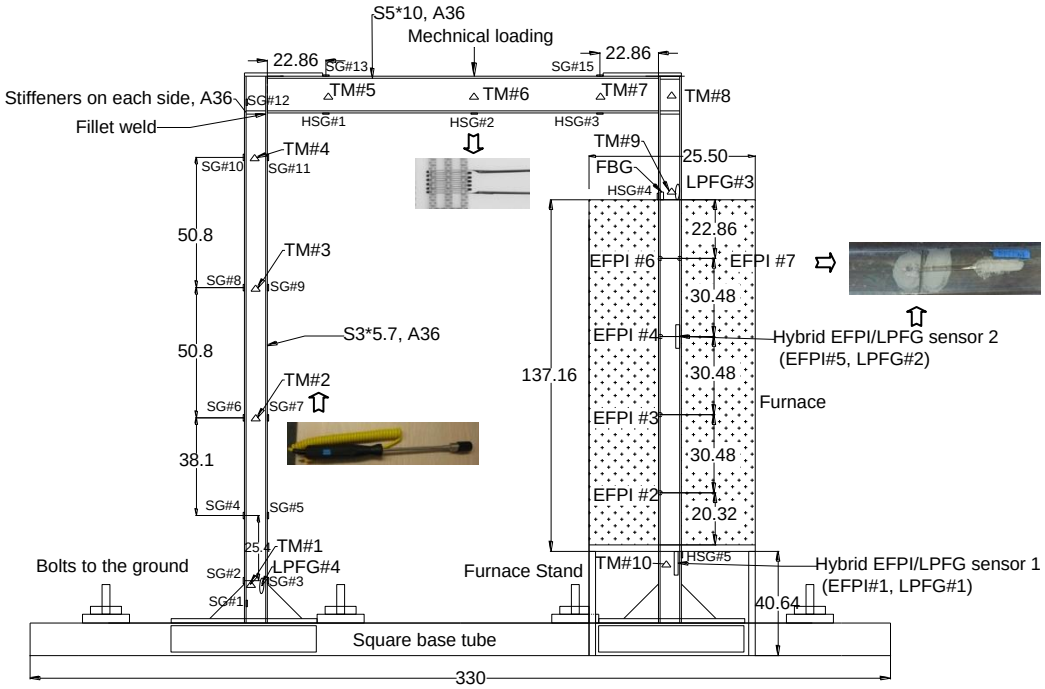

Figure 4.13 Instrumentation for simulated post-earthquake fire tests with photographic illustrations (unit: cm)

During the test at high temperature, the steel frame was also subjected to a point load at the mid-span of the top beam by a hydrostatic trigger that was controlled in displacement. A load cell was placed between the trigger and the top beam to measure the applied load on the frame. In this study, an initial load of 20.46 kN (4.6 kips) was applied by the trigger. As the temperature increased, Column #2 expanded, reducing the distance between the top beam and the hydrostatic trigger or increasing the applied load. Figure 4.14 (b) shows the load change over the time, which corresponded to the increasing of furnace temperature. Overall, as the furnace temperature increased, the load applied on the top beam increased from 20.46 kN (4.6 kips) to 44.48 kN (10 kips), indicating that a

large vertical force was applied to the steel frame. The applied force was introduced to mainly simulate the gravity effect on the frame structure.

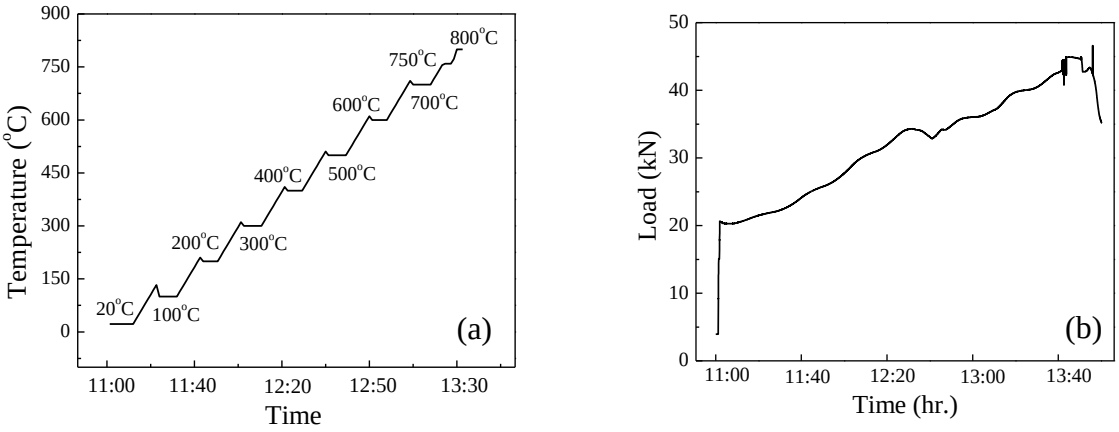

Figure 4.14 Loading profile: (a) temperature (℉= ℃×9/5+32) and (b) vertical load

4.3.4.2. Structural condition evaluation from optical fiber sensing network.

4.3.4.2.1. <u>Measured temperature distribution.</u> Figure 4.15 (a) shows the measured temperatures by the LPFG components. LPFG#1, which was placed inside the furnace, showed the same trend as the furnace temperature profile shown in Figure 4.14 (a). Figure 4.15 (b) shows the measured temperature by the FBG sensor. The temperature on the top of the furnace increased up to 288 ℃ (550 ℉).

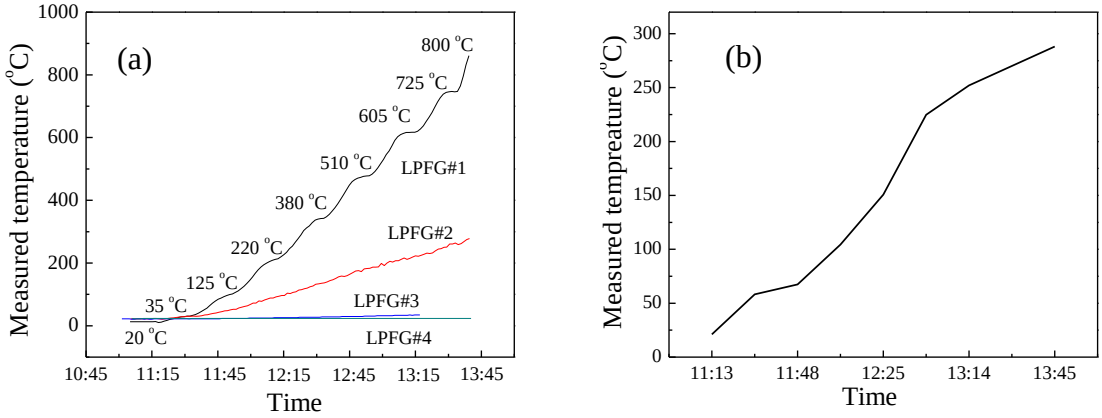

Figure 4.15 Measured temperature (℉= ℃×9/5+32): (a) LPFG sensor and (b) FBG sensor

4.3.4.2.2. <u>Measured strains by movable EFPI sensors.</u> Figures 4.16 (a, b) show a detail layout of the five EFPI sensors inside the furnace and their measured strains, respectively. At the top end of the furnace, the steel column exhibited a strain of 8% at the temperature of 500 ℃ (932 ℉). With an initial cavity of 50~60 μm, an EFPI sensor is limited to 10% in strain measurement. Thus, the two sensors on the top of the furnace ran out of the effective strain range at over 600 ℃ (1112 ℉). Other sensors with the maximum strain of less than 10% remained functional until the temperature was stabilized. Compared to the 1% strain determined from the simulated earthquake load, the strain produced by the high temperature effect was gradually increased to more than 10%, having more severe damage effects. Finally, at the evaluated temperature of 800 ℃ (1472 ℉), Column #2 failed due to extensive strain and deformation, resulting in the progressive collapse of the steel frame.

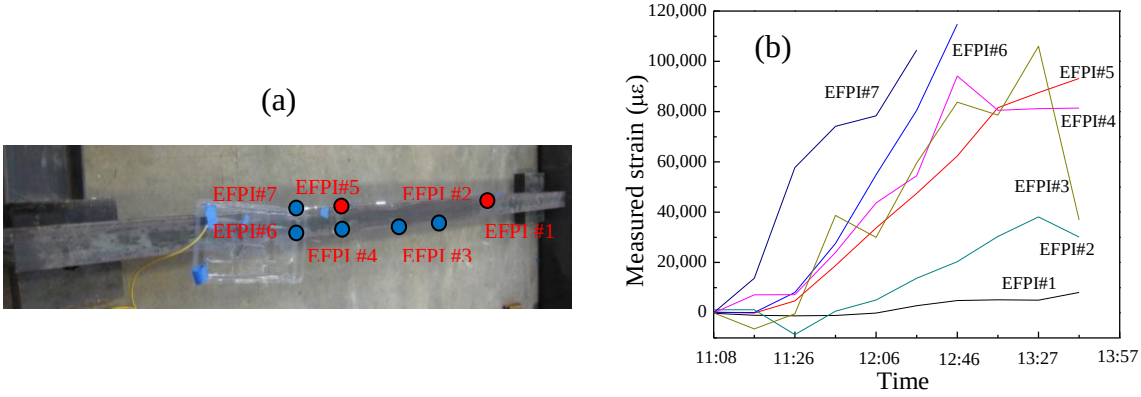

Figure 4.16 EFPI sensors: (a) detailed layout and (b) measured strains

4.3.4.3. Structural condition evaluation from commercial sensing network.

4.3.4.3.1. <u>Measured temperature.</u> With distributed thermocouple surface probes as shown in Figure 4.13, the temperature distribution along the steel frame outside the furnace area can be monitored in real time. Figure 4.17 (a) shows the measured temperature change along the steel frame as the furnace temperature increased with time. The temperature of the top beam and Column #1, where temperature loading was not directly applied, remained nearly unchanged as the furnace temperature increased. The bottom of Column #2 also remained around room temperature even as the heating temperature increased up to 800 ℃ (1472 ℉). This is likely attributed to its connection to

the large area of reinforced concrete strong floor. However, on the top of Column #2, the temperature increased dramatically up to 427 ℃ (800 ℉) as the furnace temperature rise to 800 ℃ (1472 ℉). At the location of TM #1, 9, and 10, optical temperature sensors (LPFG or hybrid EFPI/LFPG) were also deployed for comparison.

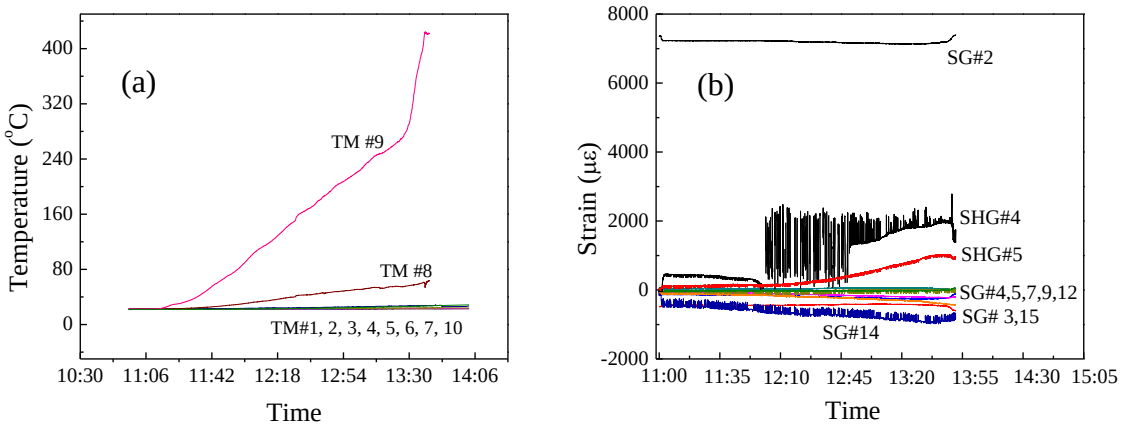

Figure 4.17 Changes monitored by commercial sensors: (a) temperature (℉= ℃×9/5+32) and (b) strain

4.3.4.3.2. <u>Measured strains.</u> All the strain gauges used during the simulated earthquake test also recorded data under the high temperature effect. Figure 4.17 (b) shows the measured strains as the furnace temperature increased. Without any direct thermal effect on Column #1, the plastic strain induced by the simulated earthquake remained nearly the same. At the location of SG#2, the permanent strain of 0.75% remained constant during the high temperature effect. Other locations did not yield fully until the furnace temperature reached 800 ℃ (1472 ℉). Figure 4.17 (b) also shows the measured strains from the high temperature strain gauges, SHG #4 and #5 prior to temperature compensation. As shown in Figure 4.17 (b), the measured strain from SHG#4 fluctuated significantly and was unreliable. This unstable situation was most likely contributed by the potential sensor damage during installation and by the potential influence of the high temperature change at this location.

4.3.4.4. Comparison among various sensing systems. The strains measured by EFPI#1 and HSG#5 are compared in Figure 4.18 (a) near the bottom of Column #2 immediately below the furnace. The two measurements showed a similar trend with a

correlation coefficient of 0.963. This comparison verified the viability of using fiber optical sensors for strain measurements. Similarly, Figure 4.18 (b) compares various temperature measurements by TM#9, LPFG#3, and FBG sensors near the top of Column #2 immediately above the furnace. Overall they are in good agreement even though the LPFG sensor appeared to give a better comparison with the thermocouple in two temperature ranges as seen in Figure 4.18 (b). Figure 4.18 clearly indicates that the developed optical fiber sensing network can closely monitor the strain and temperature information from the structures in harsh environments such as post-earthquake fire conditions, and can be further applied to practical applications for potential future studies.

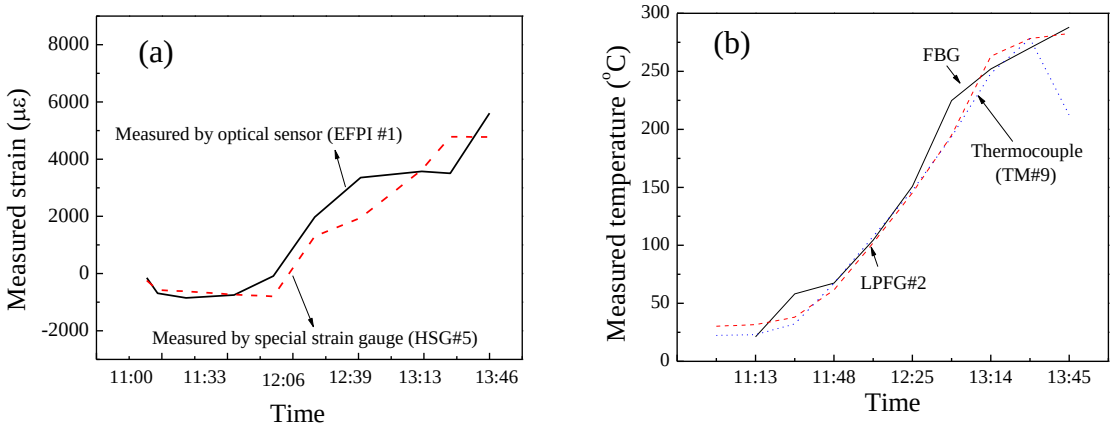

Figure 4.18 Comparison among various sensors: (a) strain measurements and (b) temperature measurements (℉= ℃×9/5+32) (b)

4.4. SUMMARY ABOUT SENSOR NETWORKS AND ITS EXPERIMENTAL VALIDATIONS

This chapter investigated the sensor networking of optical fiber sensors such as the movable EFPI sensors and the hybrid EFPI/LPFG sensors that have been discussed in previous chapters. The optical fiber sensing network was quasi-distributed and composed of LPFG and FBG sensors for temperature measurements, EFPI sensors for large strain measurements, and hybrid EFPI/LPFG sensors for simultaneous large strain and high temperature measurements. For comparison, a commercial sensing network of

thermocouples and high temperature strain gauges were also deployed to validate the performance of the optical fiber sensing network.

By using the comprehensive sensing network, the structural behavior of the one-story, one-bay steel frame was monitored and evaluated to provide insightful information on the development of the frame's buckling process under the postulated post-earthquake fire condition. Depending upon the earthquake magnitude, the post-earthquake fire induced damage may exceed the damage induced by the earthquake effect. With increasing temperature effects, the frame structure may progressively collapse even after it survives the earthquake effects. By comparing the experimental results from various sensing techniques, it was successfully demonstrated that the optical fiber system with movable EFPI, LPFG, and hybrid EFPI/LPFG sensors can measure strain and temperature up to 10% at 800 ℃ (1472 ℉). The optical sensing system can simultaneously measure large strain and high temperature in real time and is thus a promising device for structural health monitoring in post-earthquake fire conditions.

5. TEMPERATURE-DEPEDENT FINITE ELEMENT MODEL UPDATING

5.1.INTRODUCTION

In a post-earthquake fire condition, steel structures suffer from high temperature and large strain effects. Due to cost considerations, full-scale fire tests in real fires have been limited to very few structures in the world. This challenge thus stimulated an increasing interest in the use of numerical models. On the other hand, the development of a credible computational model needs the model validation data from full-scale fire testing [61]. In this case, cost consideration dictates that sensor deployments be limited to the strategic locations of a structure. During the past two decades, significant efforts have been made to develop various finite element models (FEM) for both the response of the structure to the fire disturbance and the analysis of design advantages resulted from structural modifications [62-65].

At present, there are a few research- and commercial-level software tools available for the analysis of fire hazards, structural responses, and loss estimation [12, 128-129]. Among them, FIRES-RC II, FASBUS II SAFIR, ABAQUS, and DIANA are commonly used for a nonlinear FEM analysis under fire effects with the nonlinear properties of a structure explicitly taken into account. In this case, the temperature dependence of the material properties represents one of the key challenges in numerical simulations [67]. In the past two decades, several attempts have been made to characterize the temperature-dependent material properties of steel structures [68-74]. In addition to the advanced nonlinear simulations, simplified approaches with a linear model are also acceptable for low temperature or free thermal expansion applications. When a structure is not subjected to external loads, a temperature threshold of 400℃-500℃ (752℉-932℉) is often considered according to ASTM E-119 furnace tests [75], at which the yield point of steel is well above the stress that any structural member must carry during a fire.

An FEM updating technique is often introduced to ensure that the predicted structural responses be in good agreement with their corresponding test results [74-77]. Up to date, most of the model updating studies were focused on the updating of natural frequencies by modifying structural properties under earthquake loading. To our best

knowledge, no research work on the temperature-dependent FEM updating analysis has been done for a real-time prediction of structural behaviors under fire conditions. In this study, the FEM of a steel structure is assumed to be accurate at room temperature since it can be modified against any field test data available under normal operation conditions in practical applications. The model updating is only required due to an uncertain temperature distribution along the structural members in a fire environment.

In this chapter, the single-story single-bay steel frame tested in Chapter 4 is modeled and analyzed for both earthquake and high temperature effects in ABAQUS, following the test procedure as described in Chapter 4. Initial analysis is conducted without updating temperature distribution and material properties over time and, the numerical results are compared with the test results. To better predict the structural behavior of the steel structure in harsh environments (post-earthquake fire in this study), a temperature-dependent FEM updating technique is proposed and developed by minimizing a combined normalized error of both strain and temperature predictions. A fire gravity factor is introduced to describe temperature distribution in the high temperature region, and updated in the FEM for future predictions. After model updating, the simulation results are compared again with the test results to demonstrate the accuracy of the FEM updating technique for practical applications.

5.2.FEM ANALYSIS FOR SIMULATED EARTHQUAKE EFFECT

5.2.1. Model Setup and Earthquake Effect. In this study, the single-story single-bay steel frame described in Chapter 4 was modeled with ABAQUS computer software [79], as shown in Figure 5.1 (a). In the FEM, perfect ties were considered to connect various structural components. For a future FEM analysis of the structure in fire environments, the coupled temperature-displacement linear elements (C3D8T, C3D6T, and C3D4T) were used. For example, C3D8T represents an 8-node thermally coupled brick, tri-linear displacement and temperature element [79]. The beam, Column #1, and Column #2 have 290, 396, and 2335 elements, respectively, totaling 3665 elements including stiffeners at the beam-column connections as shown in Figure 5.1 (b). The bottom ends of two columns of the steel frame are fixed to the ground by 15.24 cm (6 in.)

long stiffeners. To simulate the earthquake effect and its following post-earthquake fire effect, two simulation steps were defined in the FEM analysis for the simulated earthquake effect and the post-earthquake fire effect, respectively. In Step 1, both vertical static and lateral cyclic loads were applied. To consider the potential dead load of upper structures, a vertical load of 1.75 Mpa (254 lb/in^2) was applied at the mid-span of the top beam over an area of 15.24 cm ×15.24 cm (6 in. × 6 in.) at the beginning of the FEM analysis. A lateral cyclic load was then applied on the top of the Column #1 by using the comment of loading amplitude in ABAQUS. Since the simulated earthquake damage effect was investigated with approximately half of the frame (L-shaped), the lateral cyclic load applied on the entire frame in simulations was twice as much as 30.25 kN (6.8 kips) for the first four cycles and 33.8kN (7.6 kips) for the last cycle following the loading amplitude as shown in Figure 5.1 (c) to simulate the earthquake effect.

5.2.2. Material Property. A36 steel was used to build the laboratory frame structure tested in Chapter 4. The material properties of steel vary with temperature. Since the frame structure was subjected to a simulated post-earthquake fire condition, the temperature-dependent steel properties were used in the FEM analysis. Over the past century, the temperature dependence of steel properties had been investigated by researchers in fire safety. In this chapter, the most related temperature-dependent properties of steel are reviewed and utilized in the FEM analysis.

In this study, the nonlinear stress-strain relationship of steel at elevated temperatures as illustrated in Figure 5.2 is determined from the Euro-Code EN 1993-1.2 [69, 70]. The shape of the stress-strain relationship was considered to remain unchanged in high temperature applications, which will be further discussed in Chapter 6. As shown in Figure 5.2, the first part of the curve (point a to b) is a linear line, corresponding to the proportional limit, $f_{p,T}$, and the elastic modulus, $E_{a,T}$. The second part of the curve (point b to c) shows a transition from the elastic to the plastic range, relating to the effective yielding strength, $f_{y,T}$, the stress that corresponds to a strain of 2% or 20,000 με. The third part (point c to the end) of the curve is a flat yielding state, where the stress remains constant and the strain continues increasing. The relationship in Figure 5.2 was formulated in [70] and reproduced as listed in Table 5.1 for clarity.

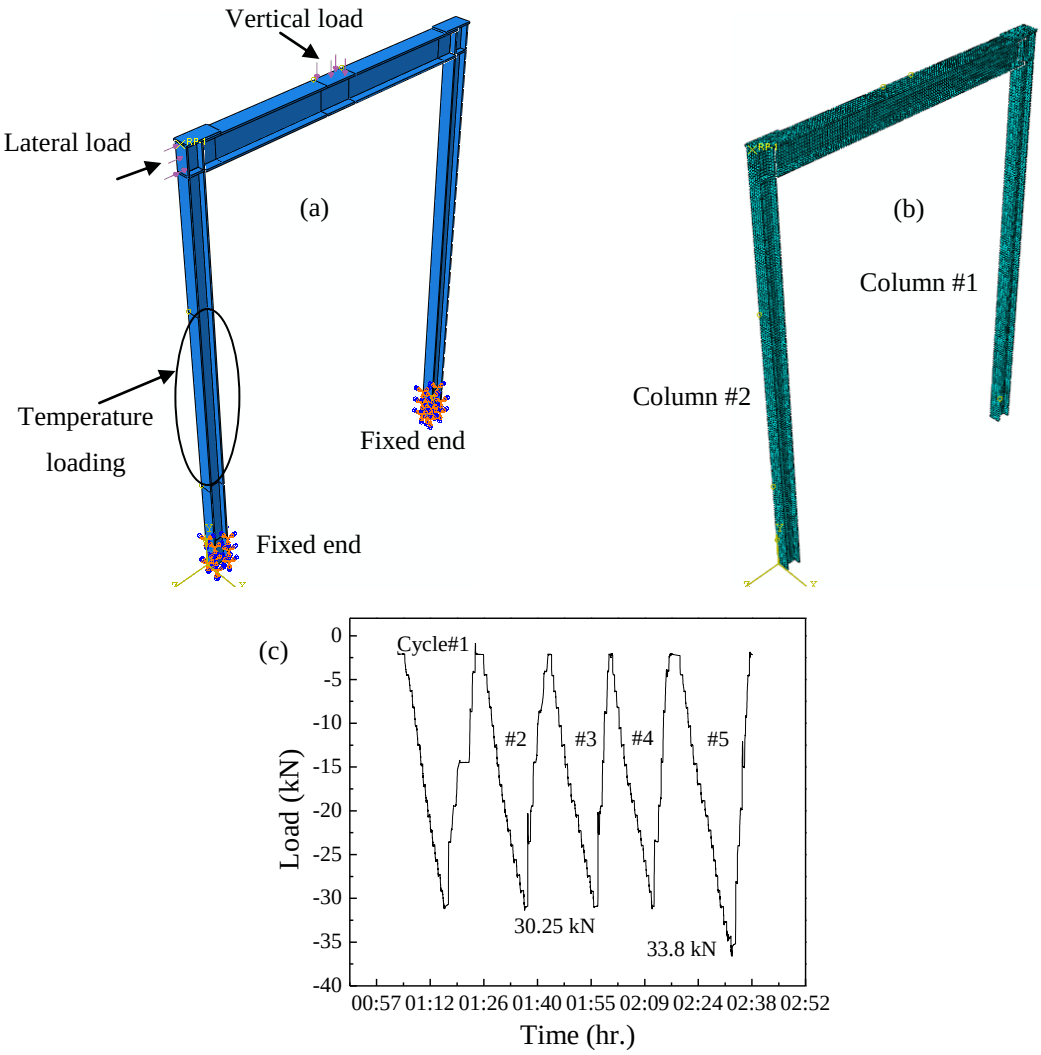

Figure 5.1 FEM setup: (a) loading and boundary conditions, (b) finite element meshes, and (c) lateral loading profile

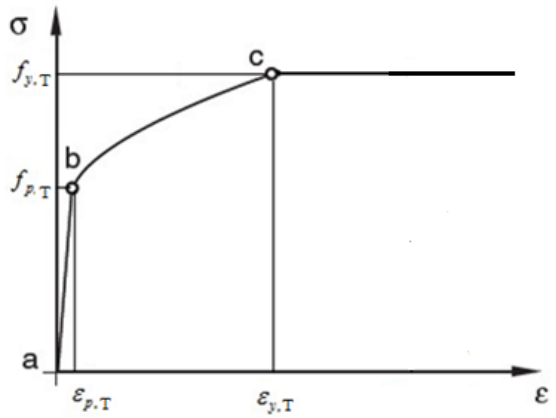

Figure 5.2 Stress-strain relationship of steel at elevated temperatures

Table 5.1Stress-strain formulation of steel at elevated temperatures [70]

Strain range	Stress, σ	Tangent modulus
$\varepsilon \le \varepsilon_{p,T}$	$\varepsilon E_{a,T}$	$E_{a,T}$
$\varepsilon_{p,T} \le \varepsilon \le \varepsilon_{y,T}$	$f_{p,T} - c + \frac{b}{a}\sqrt{a^2 - (\varepsilon_{y,T} - \varepsilon)^2}$	$\frac{b(\varepsilon_{y,T} - \varepsilon)}{a\sqrt{a^2 - (\varepsilon_{y,T} - \varepsilon)^2}}$
$\varepsilon_{y,T} \le \varepsilon \le \varepsilon_{t,T}$	$f_{y,T}$	0
Parameters	$\varepsilon_{p,T} = \frac{f_{p,T}}{E_{a,T}}, \varepsilon_{y,T} = 0.02 = 2\%$	
Functions	$a^2 = (\varepsilon_{y,T} - \varepsilon_{p,T})(\varepsilon_{y,T} - \varepsilon_{p,T} + \frac{c}{E_{a,T}})$; $b^2 = c(\varepsilon_{y,T} - \varepsilon_{p,T})E_{a,T} + c^2$; $c = \frac{(f_{y,T} - f_{p,T})^2}{(\varepsilon_{y,T} - \varepsilon_{p,T})E_{a,T} - 2(f_{y,T} - f_{p,T})}$.	

In a high temperature environment, both the stiffness and yielding strength of steel vary significantly with temperature. According to EN 1993-1.2 [69, 70], various modification factors can be introduced as presented in Figure 5.3 (a), including the reduction factor for effective yield strength, $f_{y,T}$ ($k_{y,T}$), proportional limit, $f_{p,T}$ ($k_{p,T}$), and the slope of the linear elastic range, $E_{a,T}$, ($k_{E,T}$). It is clearly seen from Figure 5.3 (a) that all the stiffness and strength modification factors decrease significantly with temperature, especially when the temperature becomes more than 500 ℃ (932 ℉).

In addition to the nonlinear strain-stress relationship, other temperature-dependent material properties of steel must be considered in fire conditions. These properties include the thermal conductivity, the specific heat, and the thermal expansion of steel. Figures 5.3 (b) and (c) show the thermal conductivity ($\lambda_{a,T}$ in W/mK) and the specific heat ($c_{a,T}$ in J/Kg K). Figure 5.3 (d) shows the temperature-dependent coefficient of thermal expansion according to AISC in 1989 [72, 75]. Considering a temperature measurement accuracy of 1 ℃ (1.8 ℉), the curves for various material properties of steel specified in EN 10025 [70] can be discretized every 5 ℃ in the FEM analysis.

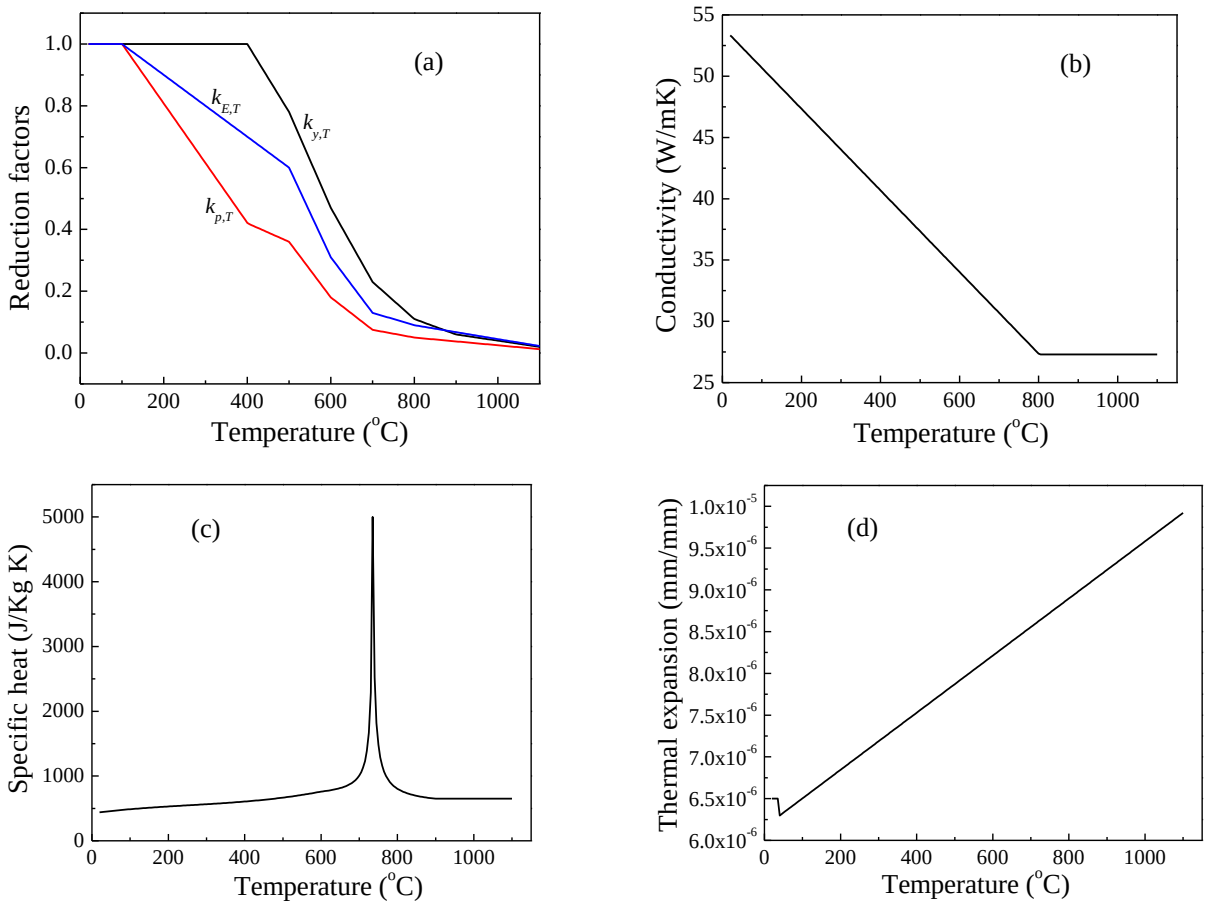

Figure 5.3 Material property modifications of steel: (a) reduction factors, (b) thermal conductivity, (c) specific heat, and (d) coefficient of thermal expansion

5.2.3. Earthquake-Induced Responses and Discussion. With the material properties of steel, the established FEM was analyzed under a simulated post-earthquake fire effect in ABAQUS. Figures 5.4 (a) and (b) display the lateral deformation of the entire steel frame and Column #1 at the end of simulation Step #1 under earthquake loads. The maximum deformation of 5.36 cm (2.11 in.) under the lateral cyclic loading occurred at the top of the column. Figures 5.4 (c) and (d) show the strain distribution of the steel frame and Column #1 at the end of Step #1. The largest strain located at the bottom of the column, which is immediately above the bottom stiffener with 17.78 cm (7 in.) above the end of the column, and the value of the largest strain associated with the last cyclic loading reaches 1.2%, indicating that the bottom of the column already yielded.

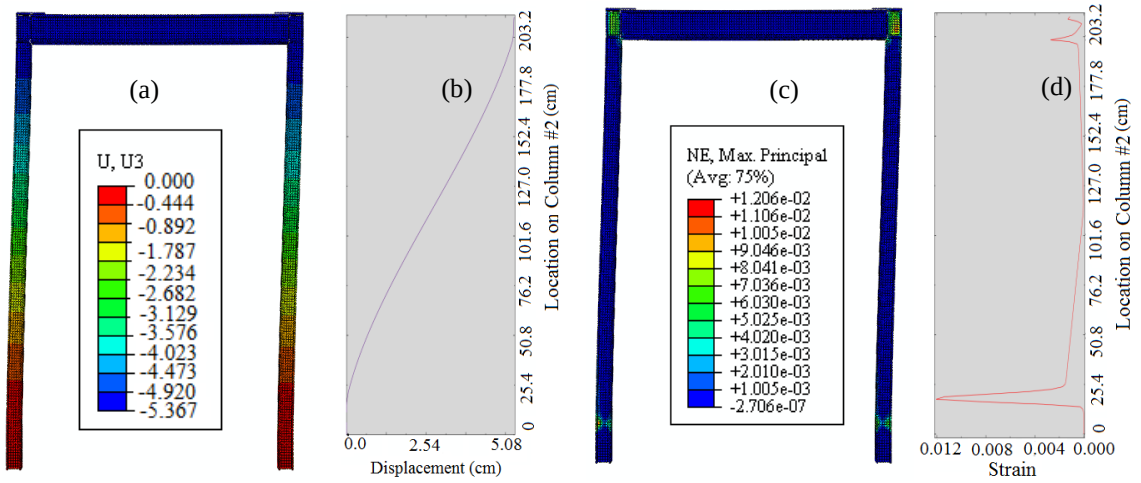

Figure 5.4 Simulation results under earthquake effects: (a) lateral deformation distribution of the frame structure, (b) lateral deformation distribution of Column #1, (c) strain distribution of the steel frame at the last loading cyclic, and (d) strain distribution along Column #1

5.2.4. Comparison between FEM Analysis and Experiment. Comparison between the FEM simulation and the experimental results from Section 2 of Chapter 4 is made in Figure 5.5. For all the five cycles of loading, the results from the FEM simulation show similar trends as the experimental results did. At the key locations, where the largest strain occurred, the difference between the simulation and the experimental results is less than 10% and the maximum differences at all the investigated locations are less than 40%, which proved the validation of the input of the FEM analysis including the material property, loading, and boundary conditions.

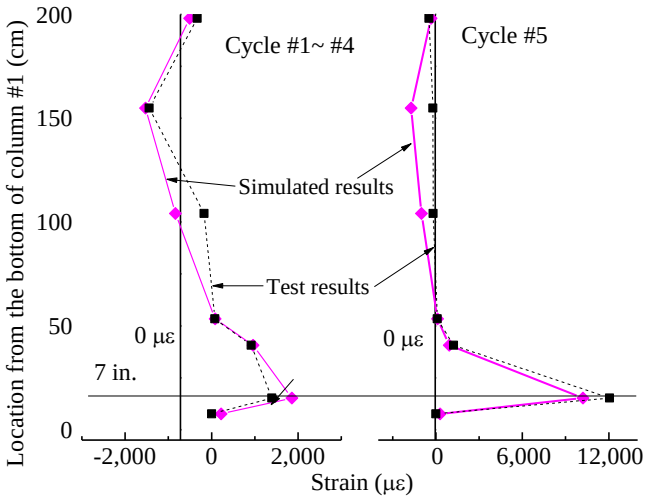

Figure 5.5 Comparison between FEM simulated strains and experimental strains

5.3.FEM ANALYSIS UNDER SIMULATED FIRE EFFECTS

5.3.1. Fire Effect. The steel frame that has already experienced the simulated earthquake-induced damage was then subjected to the simulated post-earthquake fire condition in Step 2. The simulated fire condition was introduced as temperature restraints at various boundaries of the FEM. As shown in Figure 5.6 (a), a portion of Column #2, 91.44cm (36 in.), is directly subjected to a temperature increase. The temperature loading zone starts at 63.5 cm (25 in.) and ends at 154.94 cm (61 in.) from the bottom of the column, as stated in Chapter 4. The temperature loading profile is referred to Figure 4.14 (a), gradually increasing from room temperature to 800 ℃ (1472 ℉) by an interval of 100 ℃ (180 ℉). For an initial analysis without model updating for temperature effects, the elevated temperature was assumed to uniformly distribute throughout the temperature loading zone. The temperature outside the heating zone linearly decreased with the distance from the closest point of the furnace from the elevated temperature ($T_{elevated}$) to room temperature (T_{room}) at both ends of Column #2 as illustrated in Figure 5.6. All model setup steps except for the temperature loading are the same as stated in Step 1.

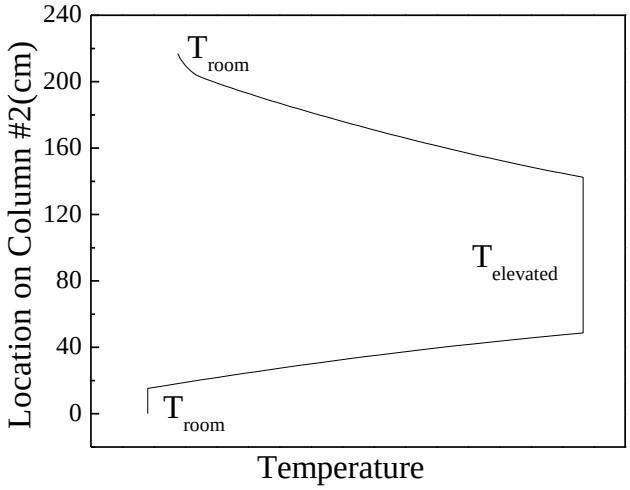

Figure 5.6 Temperature distribution over Column #2 for simulated fire condition

For a better comparison with model updating in Section 5.4, Step 2 FEM analysis was divided into eight sub-steps, each sub-step based on the information from the previous sub-step by restarting the analysis in ABAQUS using the "RESTART" function. For Sub-step 1, the temperature in the heating zone increased from room temperature (20 ℃ or 68 ℉) to 100 ℃ (212 ℉). Sub-step 2 then restarted based on the results from Sub-step 1 as temperature increased from 100 ℃ (212 ℉) to 200 ℃ (392 ℉). Each of Sub-steps 3-8 repeated Sub-step 2 based on the previous simulation results as the elevated temperature in the heating zone increased from 200 ℃ (392 ℉) to 800 ℃ (1472 ℉) at 100 ℃ (180 ℉) interval. Each sub-step took 10 minutes as shown in Figure 4.14 (a). As such, the nonlinear analysis of the FEM can be conducted in real time.

5.3.2. Simulated Fire-Induced Responses and Discussion. Figures 5.7 (a) and (b) present the simulated temperature distributions of the steel frame and Column #2, respectively, at an evaluated temperature of 800 ℃ (1472 ℉) in the heating zone. Similarly, Figures 5.7 (c) and (d) respectively show the normal strain distributions of the steel frame and Column #2. The temperature distribution over Column #2 follows exactly what was assigned. At 800 ℃ (1472 ℉), the maximum strain of the frame is 2.28%; it takes place on the top of heating zone of the furnace. At the bottom of Column #2, a plastic strain of over 1% remains as the temperature loading increases.

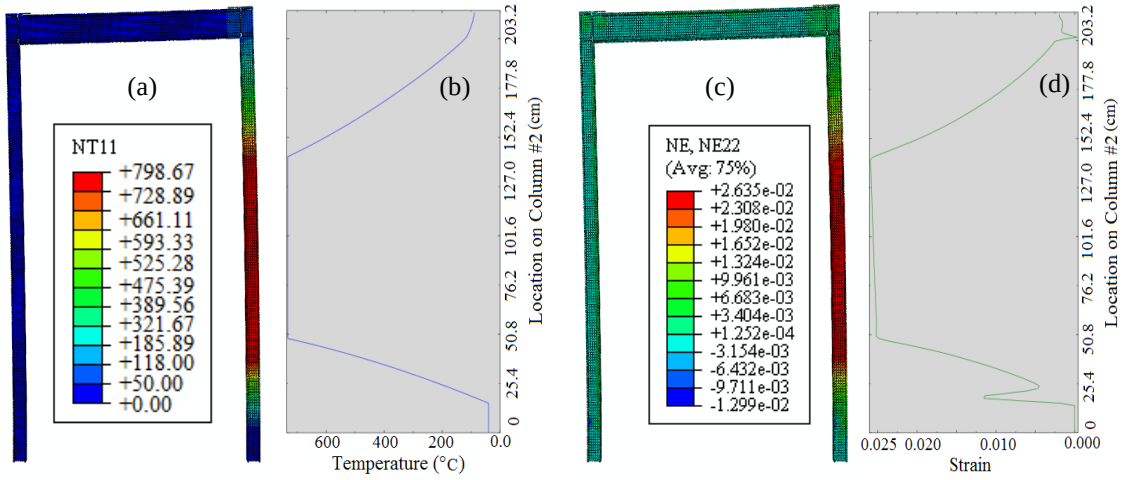

Figure 5.7 Simulated fire-induced responses at 800 ℃: (a) temperature distribution of the steel frame, (a) temperature distribution over Column #2, (c) strain distribution of the steel frame, and (d) strain distribution over Column #2

5.3.3. Simulation versus Experiment. The simulated temperature and strain are compared in Figure 5.8 with their respective experimental results. The simulated and the measured temperatures agree well at three locations with the maximum relative difference of less than 15%. The simulated strains are also in good agreement with the test results outside the furnace area; their difference is less than 10%. However, their strain difference inside the furnace is as high as 70%. This comparison indicates that the simulated temperature and strain conditions inside the furnace may differ significantly from the test conditions. To reduce their relative difference, a temperature-dependent model updating technique is proposed and developed below for material property modifications based on the measured temperature in real time.

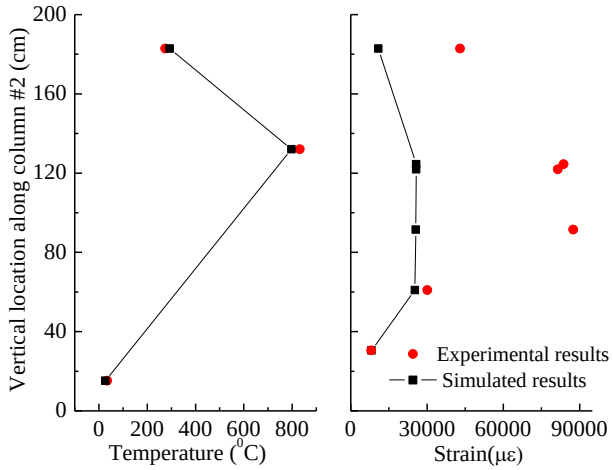

Figure 5.8 Comparison between FEM simulated results and the experimental results

5.4.TEMPERATURE-DEPENDENT MODEL UPDATING

The structural response in fire does not only depend on the fire-induced high temperature but also the heat generated by the fire. High temperature changes the material property of steel [130]. In general, heat transfers in three ways: conduction, convection, and radiation. Conduction describes the heat transfer process through a solid material by the change of material properties such as density, specific heat, and thermal conductivity. Convection depicts the heat transfer through a fluid, either gas or liquid, which linearly changes with the temperature of the fluid. Radiation is a heat transfer process by an electromagnetic wave; it highly depends upon the gas temperature as well.

5.4.1. Temperature Distribution in a Structure. For steel structures with fire protection, the temperature distribution in steel components is mainly determined by the heat transfer process in convection and radiation [130]. The temperature of unprotected steel will eventually reach the level of the fire compartment. The time to achieve a stable temperature depends on the nature of the fire exposure, the weight of a steel shape, and the heated perimeter of the steel [131]. Once the steel temperature is equivalent to the fire environment, the thermal dynamics of the steel will essentially remain stable for the duration of the fire. Based on this fact, the steel components are assumed to share the same temperatures with their surrounding gas in simulated fire environments.

Previous studies with a jet fire showed that the vertical temperature distribution of heated air with a certain speed can be evaluated by a second-degree polynomial function of the axial position along the centerline of the heated air [132-135]. For the sake of simplicity, a piecewise linear function is proposed to simulate the vertical temperature distribution of the heated air (generated by a vertically placed furnace) as illustrated in Figure 5.9 and expressed by Eq. (31).

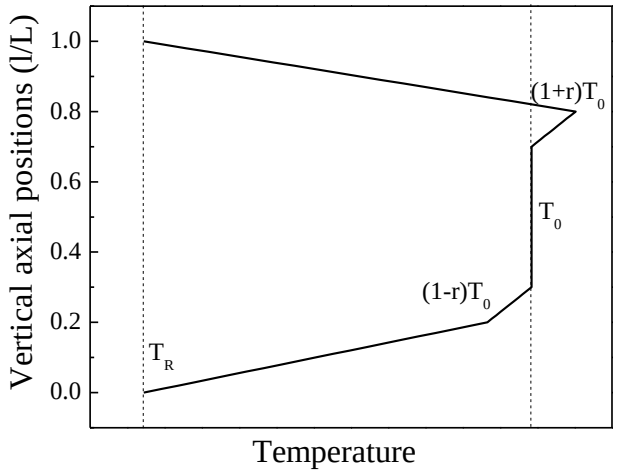

Figure 5.9 Piecewise linear vertical distribution of the temperature of heated air

$$T=\begin{cases}5p(1-r)T_0+(1-5p)T_R, & 0\le p\le 0.2\\ T_0(1-3r+10rp), & 0.2\le p\le 0.3\\ T_0, & 0.3\le p\le 0.7\\ T_0(1-7r+10rp), & 0.7\le p\le 0.8\\ 5(1-r)(1-p)T_0+(5p-4)T_R, & 0.8\le p\le 1\end{cases} \tag{32}$$

where T_0 represents the temperature in the heating zone of a vertical furnace, T_R denotes the room temperature, p is a normalized vertical position (l/L), l represents the position of the heated air, L is the total length affected by the heated air, and r is a temperature gradient factor that represents the fire gravity effect and can be evaluated by experiments.

5.4.2. Model Updating Strategy and Algorithm. For simplicity, this study is limited to a fire that initiates from one location of a steel building. In this case, the steel

structure is subjected to the highest temperature near the fire zone and a linearly decreasing temperature with distance from the near end of the fire zone. The temperatures at joints where several structural members are connected are the same. At the boundaries of the steel structure where structural members are directly connected with the ground or when the steel components are far away from the heating zone, a room temperature is assumed.

5.4.2.1. Model updating strategy. A temperature-dependent model updating strategy is proposed as illustrated in Figure 5.10. With an initial *r*, the FEM analysis of a steel structure is first conducted under fire effects. The simulated responses are then compared with the test results at strategic locations. Their difference will be minimized in the least squares sense by modifying the temperature distribution in the steel structure represented by *r* and thus the steel material properties. The minimization process leads to a model updating algorithm that will be derived in this section. With the updated *r*, a revised FEM analysis can be conducted for a better prediction of stress and strain distributions of the steel structure in a high temperature environment. The above model updating will repeat in numerical simulations at various time steps of a fire.

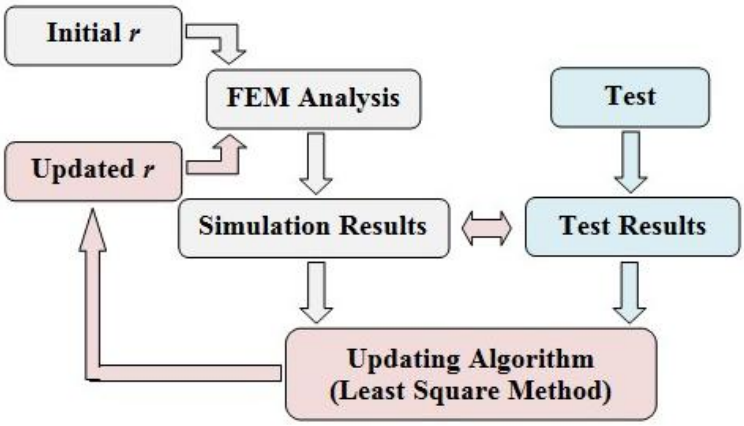

Figure 5.10 Temperature-dependent model updating

5.4.2.2. Model updating algorithm. The objective function for the development of a model updating algorithm is to minimize a total simulation error against various experimental results. That is,

$$S = \beta s_1^2 + (1-\beta) s_2^2 \tag{33}$$

in which S is the weighted sum of the squared of relative errors by the FEM prediction with s_1 for temperature sensors and s_2 for strain sensors and β is a weighting factor on the effect of temperature. The weighting factor was selected to range from 0 to 0.5 since strain depends on the change of temperature with more uncertainty and thus requires more weight to minimize its corresponding error. When β=0.5, the strain and temperature play an equal weight in the updating process. The relative error associated with each type of sensors s1 and s2 can be evaluated by:

$$s_1^2 = \alpha_T \sum_{j=1}^{N} \left[\left(T_{mj,n+1} - f_{T,j}\left(r_{n+1}\right) \right) \right]^2, s_2^2 = \alpha_\varepsilon \sum_{j=1}^{M} \left[\left(\varepsilon_{mj,n+1} - g_{\varepsilon,j}\left(r_{n+1}\right) \right) \right]^2 \tag{34}$$

in which α_T and α_ε are the temperature and strain normalization coefficients, respectively, which can be further expressed as:

$$\alpha_T = \frac{1}{\sum_{j=1}^{N} \left(T_{mj,n} - T_{sj,n} \right)^2}, \alpha_\varepsilon = \frac{1}{\sum_{j=1}^{N} \left(\varepsilon_{mj,n} - \varepsilon_{sj,n} \right)^2} \tag{35}$$

where N and M represent the numbers of temperature and strain sensors, respectively; r_n and r_{n+1} denote the temperature gradient factors at time step n and $n+1$, respectively; $T_{mj,n}$ and $T_{sj,n}$ stand for the measured temperature at the j^{th} sensor and the simulated temperature with $r=r_n$ at time step n; $f_{T,j}(r_{n+1})$ is the simulated temperature at sensor location j when $r=r_{n+1}$. Similarly, $\varepsilon_{mj,n}$ and $\varepsilon_{sj,n}$ stand for the measured and simulated strain at the j^{th} sensor with $r=r_n$ in at time step n; $g_{\varepsilon,j}(r_{n+1})$ is the simulated strain at sensor location j when $r=r_{n+1}$.

The objective function in Eq. (33) will be minimized when its first derivative of S is set to zero [136]:

$$\beta\alpha_T \sum_{j=1}^{N} \frac{df_{T,j}(r_{n+1})}{dr_{n+1}} \left(T_{mj,n+1} - f_{T,j}(r_{n+1})\right) + (1-\beta)\alpha_\varepsilon \sum_{j=1}^{M} \frac{dg_{\varepsilon,j}(r_{n+1})}{dr_{n+1}} \left(\varepsilon_{mj,n+1} - g_{\varepsilon,j}(r_{n+1})\right) = 0 \quad (36)$$

From Eq. (36), it can be seen that with proper setting of β value, less iterations, faster calculation, and better solutions are expected. When r is assigned to an initial value such as $r_0=0.1$ and a weighting factor $\beta=0.5$, Eq. (36) gives r_1 that can be used to predict a more accurate temperature distribution along various members of the steel structure for the next step of strain simulations. In general, the temperature gradient factor r_n at time step n is used in Eq. (36) to determine an updated r_{n+1} for accurate prediction of both temperature and strain distributions in the structure. This process continues until the fire is over.

5.4.3. Validation of the Temperature-Dependent Model Updating Technique.

5.4.3.1. Implementation of model updating algorithm. The FEM of the steel frame for the initial analysis as illustrated in Figures 5.1 (a, b), Figure 5.2, and Figures 5.3 (a~d) is considered for further analysis with model updating in ABAQUS [79]. The only difference is the introduction of a temperature distribution with the fire gravity effect as shown in Figure 5.9 and Eq. (32). To accurately represent the particular temperature distribution, the steel frame was divided into 13 temperature zones along the steel member as shown in Figure 5.11. The temperature loading in the furnace area, representing a direct contact of steel column with the high temperature environment over 91.44 cm (36 in.) long, is designated as T_0 and located in T-zone 5. The elevated temperatures in the following zones are set to be: room temperature (T_R) in T-zone 1 and T-zone 13, $(1-r)T_0$ in T-zone 3, $(1+r)T_0$ in T-zone 7, $(1-2r)T_0$ in T-zone 9, and $(1-3r)T_0$ in T-zone 11. The temperatures in the remaining zones are linearly interpolated. The temperature, T_0, increases from room temperature (20 ℃ or 68 ℉) to 800 ℃ (1472 ℉) at an interval of 100 ℃ (180 ℉), as shown in Figure 4.14 (a) similar temperature profile as used for the initial analysis and laboratory test in Section 5.3.

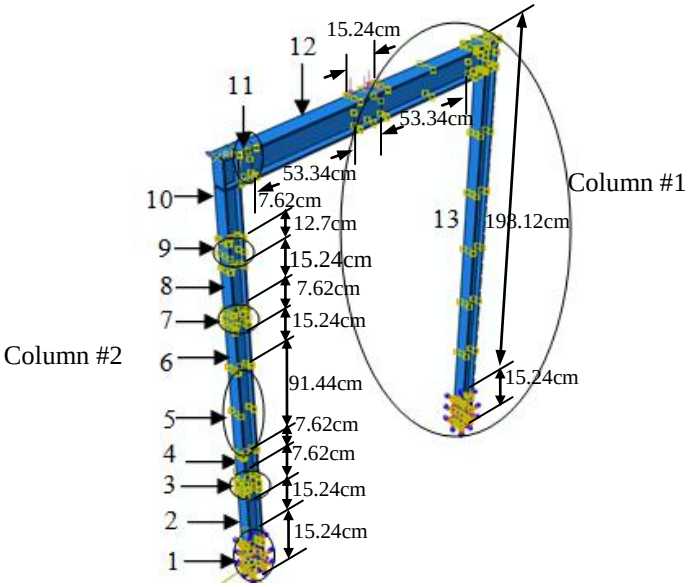

Figure 5.11 FEM of the steel frame and temperature zones

5.4.3.2. FEM analysis with model updating. For the purpose of model updating, the nonlinear stress analysis of the frame structure was conducted in 8 steps under the combined dead and thermal loads. The fire gradient factor r_{i-1} obtained in Step *i-1* was used as the initial value in the model updating algorithm for Step *i* (*i=1,2, ..., 8*). The temperature loading in each step is 20-100 ℃ (68-212 ℉), 100-200 ℃ (212-392 ℉), 200-300 ℃ (392-572 ℉), 300-400 ℃ (572-752 ℉), 400-500 ℃ (752-932 ℉), 500-600 ℃ (932-1112 ℉), 600-700 ℃ (1112-1292 ℉), and 700-800 ℃ (1292-1472 ℉). This series of analyses were executed automatically using the "restart" command in ABAQUS. Each step of ABAQUS analysis took approximately half a minute for any single iteration so that near real time updating of the FEM is feasible in practical applications. For each step of analysis, two iterations when $\beta = 0.3$ or two or three iterations when $\beta = 0.5$ are expected. The ABAQUS results are fed into a MATLAB Program that was written to implement the temperature-dependent model updating algorithm.

5.4.3.3. Effects of model updating. Figure 5.12 (a) shows the simulated strain distribution of the steel frame at an elevated temperature of 800 ℃ (1472 ℉) after a temperature-dependent model updating was completed in real time with $\beta=0.5$. Figure 5.12 (b) shows a view of the steel frame deformation after the validation test. The numerical simulations in Figure 5.12 (a) show the maximum out-of-plane deformation of

7.07 cm (2.78 in.) at the top of Column #2. Correspondingly, the permanent out-of-plane deformation of Column #2 is 7.62 cm (3 in.) as observed at the completion of thermal load tests. The good comparison between Figure 5.12 (a) and Figure 5.12 (b) indicates that the temperature-dependent model updating method can accurately predict the failure mode of the steel frame with a relative error of 7.2% in permanent deformation. Figure 5.12 (a) also shows the strain distribution of the FEM analysis in the last temperature loading step at 800 ℃ (1472 ℉) after the use of the temperature- dependent model updating technique.

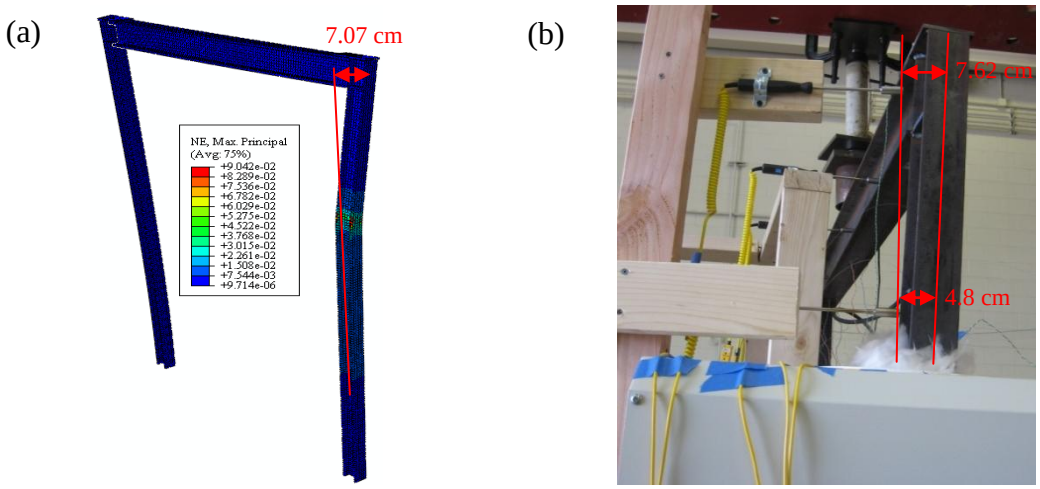

Figure 5.12 Performant deformation of the steel frame: (a) simulation with model updating and (b) observation at the completion of thermal tests

In addition, the relative error of the simulation before and after model updating is also compared as illustrated in Figure 5.13. The relative error of the FEM results ranges from 75% to 100% before model updating, and becomes less than 20% after model updating. The proposed model updating algorithm can effectively reduce the prediction error by numerical simulations.

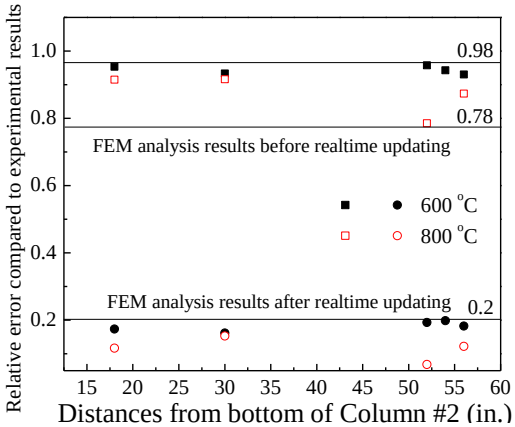

Figure 5.13 Relative errors of the FEM predictions before and after model updating

5.4.4.4. Model updating sensitivity analysis. To better understand the sensitivity of the proposed model updating algorithm to various influence parameters, a series of FEM analyses were conducted as summarized in Table 5.2 for three cases of sensor deployment objectives. The effect of the number of sensors used in model updating on the maximum strain (ε_{max}) of the steel frame is presented in Table 5.3 at 800 ℃ (1472 ℉) when β=0.5. It is clearly seen from Table 5.3 that Case #2 has similar accuracies to Case #1; both cases are much more accurate than Case #3. This comparison indicates that inclusion of the key sensors in the heating zones in model updating is necessary and sufficient. Specifically, the four locations corresponding to the four characteristic temperatures in the high temperature zones as shown in Figure 5.9 must be monitored closely.

Table 5.2 Sensor deployment objectives in three cases

Case #.	Sensors for performance validation	Sensors for updating
1	SG#1~12; TM#1~4; TM#9~10; LPFG#4; FBG	SG#13~15; HSG#3~5; TM#5~8; EFPI#1~7; LPFG#1~3
2	SG#1~15; HSG#3~5; TM#1~8; TM#9~10; LPFG#4; FBG	EFPI#1~7; LPFG#1~3
3	SG#1~15; HSG#3~5; EFPI#2,4,6; TM#1~8; TM#9~10; HSG#3; LPFG#4; FBG	EFPI#1,3,5,7; LPFG#1~3

Table 5.3 Influence of the number of updating sensors (T_5=800 ℃, 1472 ℉)

Distance from Column #2 Base (cm)	Relative error (%) of predicted maximum strain (ε_{max}) by FEM		
	Case #1	Case #2	Case #3
45.72	11.7	11.9	13.3
76.20	15.3	15.7	18.6
132.1	6.82	7.21	19.9
142.2	12.2	12.9	18.3

The selection of β is then investigated. Figures 5.14 (a, b) compare the numerical simulations for strain and temperature distributions, respectively, when β=0.5, 0.3, and 0.1 and prior to model updating at an elevated temperature of 800 °C (1472 °F). As β increases, the level of agreement between the simulations to the experiment results improve first and then either drops for strain comparison or remains nearly unchanged for temperature comparison. As such, β=0.3 provides the best updated estimation of both temperature and strain. For a more detailed analysis, more β values from 0.1 to 0.5 with an interval of 0.05 were taken. Table 5.4 compares the relative errors in maximum strain at various β values. The minimum error for a combined strain and temperature prediction appears to occur when *β=0.3*, indicating that the temperature-dependent model updating is more sensitive to the strain effect than the temperature.

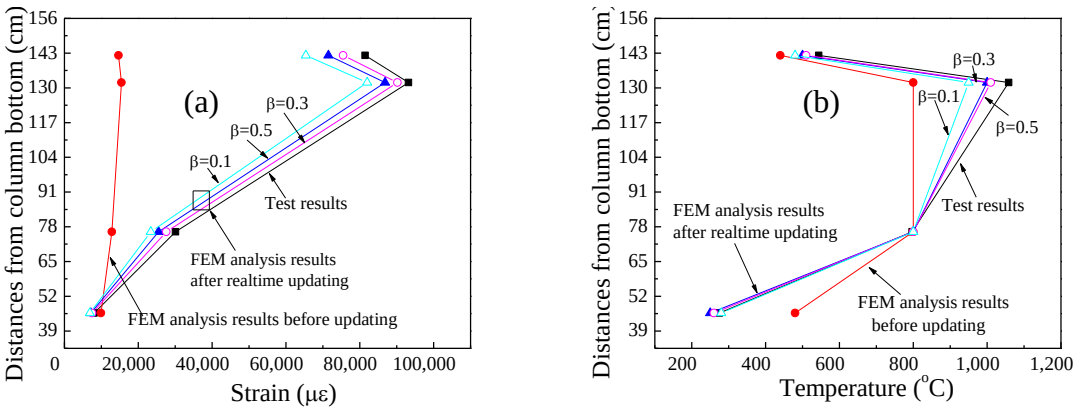

Figure 5.14 Experimental versus simulated strains before and after model updating for various β values: (a) strain comparison and (b) temperature comparison

Table 5.4 Influence of β (Case #1 in Table 5.2)

Distance from Column #2 Base (cm)	Relative error (%) in Maximum Strain (ε_{max})						
	β=0.5	β=0.4	β=0.35	β=0.3	β=0.25	β=0.2	β=0.1
45.72	11.7	11.3	10.9	10.2	11.7	12.8	13.7
76.20	15.3	14.9	14.0	13.2	14.9	16.2	17.8
132.1	6.82	6.45	6.19	5.26	6.27	6.81	7.31
142.2	12.2	12.1	11.8	11.6	12.2	13.7	14.3

In addition, the effect of the initial temperature gradient factor on the maximum strain is also investigated as shown in Table 5.5 for three cases: r_0=0.05, 0.1, and 0.15 with β=0.5. It can be seen from Table 5.5 that various selections of initial r_0 values don't significantly affect the model updating results as a result of two opposing effects. On one hand, three selections of the initial value in Table 5.5 changed the updated temperature gradient factor significantly at low temperature but little at high temperature. On the other hand, the structural material properties change little at low temperature but significantly at high temperature. The net effects of the above two influences were cancelled each other. Therefore, an approximate estimate of temperature distribution at low temperature has little influences on the material properties of the frame structure and on the maximum strain. As the temperature increases, the updated temperature gradient factor becomes increasingly more accurate, leading to high accuracy in the prediction of the maximum strain.

Table 5.5 Influence of initial r_0 (Case #1 in Table 5.2)

Step No.	r_0=0.05		r_0=0.1		r_0=0.15	
	r_{n+1}	ε_{max} (με)	r_{n+1}	ε_{max} (με)	r_{n+1}	ε_{max} (με)
1	0.12	728	0.14	736	0.17	764
2	0.14	1098	0.16	1116	0.17	1133
3	0.16	2201	0.17	2255	0.18	2277
4	0.17	9483	0.18	9524	0.18	9524
5	0.18	24140	0.18	24140	0.19	24280
6	0.19	51580	0.19	51580	0.19	51580
7	0.20	78610	0.20	78610	0.20	78610
8	0.21	90430	0.21	90430	0.21	90430

5.5. SUMMARY ABOUT TIMPERATURE-DEPEDENT MODEL UPDATING

In this chapter, the structural behavior of the steel frame discussed in Chapter 4 was predicted by its FEM with and without model updating in real time. Based on extensive simulations and their comparison with corresponding experimental results, the following conclusions can be drawn:

(1) The temperature-dependent model updating technique was successfully implemented in real time during the test of a steel frame under combined gravity and thermal loads. It can accurately predict structural behaviors of the steel structure with the predicted permanent out-of-plane deformation in column less than 7.2% in relative error from the corresponding test result.

(2) The proposed model updating algorithm was formulated to minimize the sum of normalized strain and temperature differences between simulations and measurements. It can reduce relative strain errors at 800 ℃ (1472 ℉) from at least 75% to less than 20%. Thus, the proposed model updating technique is a viable approach to evaluate various behaviors of steel structures in real time.

(3) The number of sensors in fire zones that can satisfactorily capture the four characteristic temperatures in vertical temperature distribution function is necessary and sufficient in the application of the proposed model updating algorithm. The

accuracy of the updating algorithm is insensitive to the selection of the initial temperature gradient factor but sensitive to the selection of the weight factor β. As such, an initial value of $r_0=0.1$ and the best weight factor β=0.3 is suggested in engineering applications.

6. PROGRESSIVE COLLAPSE EVALUATION OF STEEL BUILDINGS WITH ADAPTIVE MULTI-SCALE MODELING

6.1. INTRODUCTION

Civil engineering structures are large in scale and often built with multiple materials such as steel, concrete, masonry, and wood. Full-scale experimentations of such large-scale complex structures are cost prohibitive in most cases. Therefore, computational tools have become increasingly used in design and analysis of civil engineering structures, particularly with the advent of computer technologies.

Among various platforms, finite element approximations can handle a large number of calculations in parallel and have already emerged as a powerful computational tool for many practical applications [137]. Three-dimensional (3-D) beam and two-dimensional (2-D) plate elements are often used in the finite element model (FEM) of a civil engineering structure under earthquake loads [138]. Although sufficient in representing the behavior of a structure, these elements cannot provide the detailed information about materials and their potential damage over a cross section of the structural components. Therefore, for large strain areas or stress concentration spots [139, 140], a structural component such as beam and column must be discredited into many 3-D solid elements over any cross section [141], each referred to as a fiber element of the component in this study. On the other hand, using fiber elements to model a beam or column requires significantly more computation efforts, especially for large-scale structures in civil engineering application.

To make the best use of FEM tools for complex systems, multi-scale modeling has been investigated to evaluate composite structures [142] or chemical processes [143]. For instance, micro-scale and meso-scale models were combined for the contact analysis of masonry structures under impact loads [144, 145] and for the progressive failure analysis of steel structures under seismic loads [83]. To date, the potential advantages of combined micro- and large-scale modeling are yet to be fully explored.

Furthermore, civil engineering structures are nowadays designed with the load and resistance factor design (LRFD) philosophy in most parts of the world. This philosophy recognizes the uncertainty in the determination of loads and strengths [84].

Viewed as a sample of the LRFD space, the material properties [85] and external loads of a structure are unknown in prior at any time of service life, although general properties such as the modulus of elasticity and density can be evaluated from low amplitude vibration under operational loads. The critical properties for structural behavior evaluation such as yield strength of steel and tensile/compressive strengths of concrete cannot be obtained without damaging the structure. Therefore, to understand and evaluate the actual behavior of an engineering structure, real-time structural monitoring and model updating in multiple scales is necessary during an extreme event such as earthquakes. The process to resolve a solution with real time monitoring and updating of a multi-scale model is referred to as hybrid simulations with adaptive multi-scale modeling in this study. Such a strategy has been applied into an analysis of crack propagation and contact analysis for masonry bridges [144, 145]. However, up to date, no material property, environmental change, and structural behavior associated adaptability has been considered in practical applications.

In this chapter, built upon the validated structural sensing and model updating methods in Chapters 4 and 5, a hybrid simulation method with adaptive multi-scale modeling is proposed for an engineering structure. The adaptive multi-scale model of the structure has a representative substructure fully instrumented for its actual structural and material behaviors under external loading, and the remaining substructures computationally simulated for its predicted behavior. Therefore, a hybrid simulation of instrumented and computational components is realized.

A structure is divided into many groups, each having similar geometries and identical materials due to structural symmetry. For each group, the most critical structural member referred to as “master member” is modeled with fiber elements and the remaining members called “slave members” are modeled with beam and plates elements. The material behavior (stiffness & yielding stress), service environments (temperature distribution and external loading), and structural damage of the master member can be monitored in real time with sensor technologies and introduced to the modeling of slave members in real time, based on the premise that the latter can be related to the former in terms of construction process and noise characteristics.

Emphasis is placed on the development of an overall adaptive multi-scale modeling framework with noise characterization, load monitoring, environmental monitoring (basically temperature distribution), and resistance evaluation in real time. Towards this end, the master member is instrumented with an array of sensors for material property, temperature distribution, and structural behavior monitoring, and the slave members are numerically simulated with a finite element model established in ABAQUS. To verify and support the premise about member construction processes and noise attributes, model updating is performed to ensure that the interface between the master member and the slave members is compatible in terms of temperature, forces, and displacements under a predetermined evaluation criterion.

To prove its feasibility in practical applications, the adaptive multi-scale modeling concept is applied to a full-scale steel building with four stores and two bays, which was tested experimentally on the 3-D shake table located in Miki City, Hyogo Prefecture, Japan for the effects of the 1995 Kobe earthquake [85, 146, 147]. Both the predicted structural behaviors (frequency and displacement) with and without adaptive multi-scale modeling are compared with the experimental results to validate the developed hybrid simulation method for practical applications.

6.2.ADAPTIVE MULTI-SCALE MODELING STRATEGY

In addition to the real-time updating of environmental conditions such as temperature distribution as introduced in Chapter 5, material properties that significantly affect the structural behavior under harsh environments must be carefully considered. Critical properties for structural behavior evaluation such as yield strength of steel and tensile/compressive strengths of concrete are unable to obtain without damaging the structure. Moreover, the elastic waves due to crack nucleation generated in a solid structure may change the characteristics of noise under extreme loads.

6.2.1. Probability Distribution of Material Property. The material properties (MP) of structural members are generally non-uniform. For example, even steel that is often considered to be uniform has an approximately 10% variation of material

parameters [148]. In most cases, the property of structural materials approximately follows a Gaussian probability distribution if a large number of specimens of a material parameter were taken and tested [149]. That is,

$$f(x;\mu,\sigma^2)=\frac{1}{\sigma\sqrt{2\pi}}e^{-\frac{(x-\mu)^2}{2\sigma^2}} \tag{36}$$

where μ and σ represent the mean/expectation and the standard deviation of the material parameter, respectively. Figure 6.1 illustrates how the probability distribution function of material strength changes for (a) elastic-perfectly-plastic and (b) bi-linear strain hardening systems. For the elastic-perfectly-plastic steel members, only one probability distribution function is needed to characterize the property distribution of material strength, which can be identified from the yield strength or the modulus of elasticity (*k*). For the bi-linear steel members, at least two probability distribution functions are required for yield strength and strain hardening. For concept validation and simplicity, the elastic-perfectly-plastic steel members are considered and their corresponding probability distribution functions are used in the adaptive modeling as shown in Figure 6.1 (a).

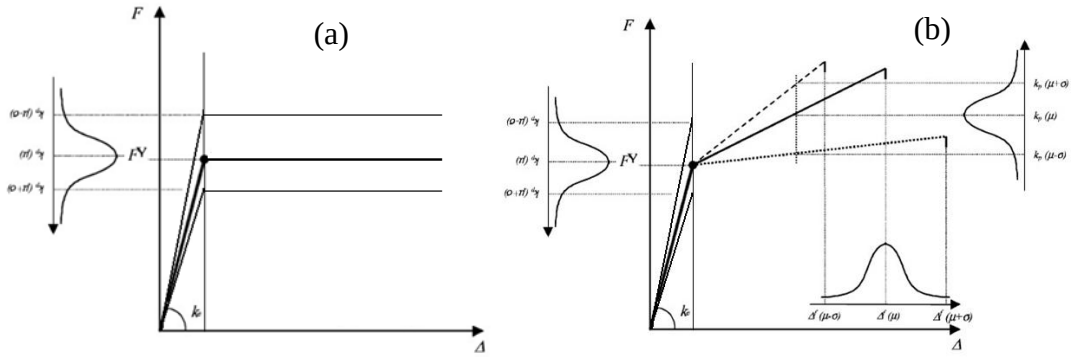

Figure 6.1 Probability distribution of steel material properties: (a) elastic perfectly plastic and (b) strain hardening

6.2.2. Adaptive Multi-Scale Modeling Concept. Figure 6.2 shows a flow chart of the adaptive multi-scale modeling concept. A model structure is divided into many groups, each having similar geometries and material properties following the same probability distribution due to structural symmetry. For each group, the most critical structural member or "master member" is modeled with a suite of 3-D linear hexahedral elements in parallel or fiber elements. The remaining members or "slave members" are modeled with beam and plate elements. By estimating the material properties of the "master member" and updating those of the "slave members" in real time, the dynamic behavior of the multi-scaled structural system can be evaluated accurately.

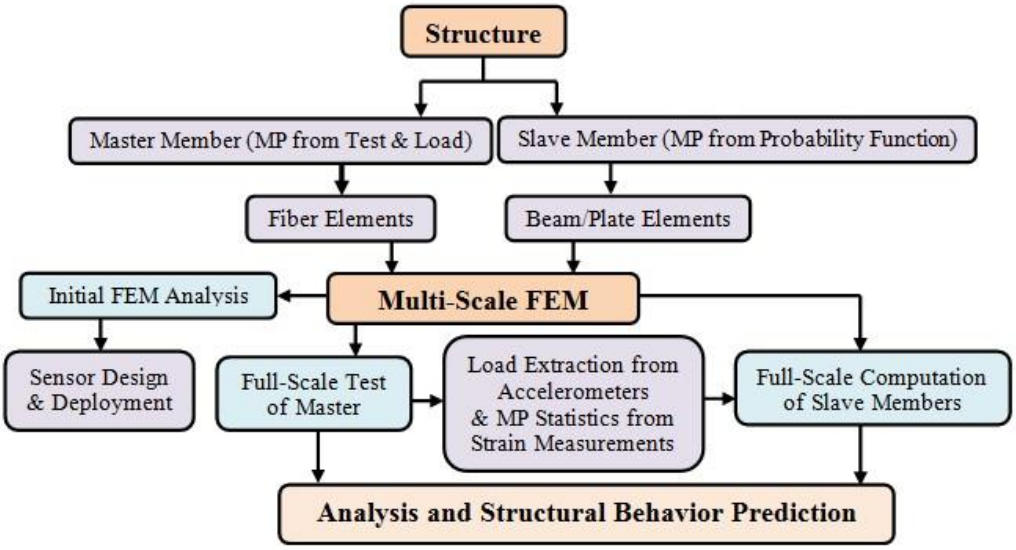

Figure 6.2 Hybrid simulation flow chart with an adaptive multi-scale FEM

A FEM model can be validated with laboratory and/or field experimentations. For cost effectiveness, a model structure is partially instrumented at strategic locations. In this study, the master member is determined by analyzing a conventional FEM of the entire structure under earthquake excitations. The master member is then instrumented with a large number of sensors to obtain the properties of material parameters in real time and the slave members with a few sensors for global model updating. The sensed/measured data such as load, strain, displacement, and environmental information is recorded by a data acquisition system, processed in real time with a high frequency data processing

algorithm, and used to directly predict material properties and structural behaviors including stress, material property, damage, and resistance.

The evaluated material properties from the master member were considered as the corresponding mean values of the slave members in the same group. Empirical estimations were used to determine the standard derivation of the slave members based on their probability distribution functions [148] with due consideration of construction processes and noise characteristics from the structural damage under various external loads. In addition, the measured loads and temperatures can also be used to update the material properties of structural members as appropriate. With the updated structural properties and environmental conditions, the FEM will be re-analyzed and compared with the measured data from the slave members. If the difference between the simulation and tested data is within a certain acceptable range, the adaptive multi-scale model can be applied for future structural behavior prediction under extreme loads such as earthquakes, fires, and blasts. If not, the material properties and structural behaviors of the slave members will be re-assigned based on the probability distribution function of material parameters until the response prediction of the slave members is in good agreement with the experimental responses at sensor locations.

6.3.HYBRID SIMULATION ON EARTHQUAKE-INDUCED RESPONSES

To illustrate the hybrid simulation with the proposed adaptive multi-scale modeling concept and evaluate the effectiveness of the modeling technique, the 4-story, 2-bay steel building tested on the 3-D shake table in Miki City, Hyogo Prefecture, Japan, was taken as a test bed in this study [146,147]. As indicated by the longitudinal (X-direction in North-South) and transverse (Y-direction in East-West) directions in Figure 6.3, the building has a rectangular plan with longitudinal dimension of 10 m (32.8 ft.) and transverse dimension of 6 m (19.7 ft.). It has four stories, each 3.5 m (11.5 ft.) tall with a total of 14 m (45.9 ft.). According to Suita et al (2007a, 2007b) [146, 147], the columns were made of cold-formed square tubes and the beams were made of hot-rolled wide flanges. The detail design of the building structure including member sizes can be referred to [146, 147]. The building structure was analyzed in the ABAQUS software

platform in two cases: with and without the adaptive process in real time under the 1995 Kobe earthquake excitations.

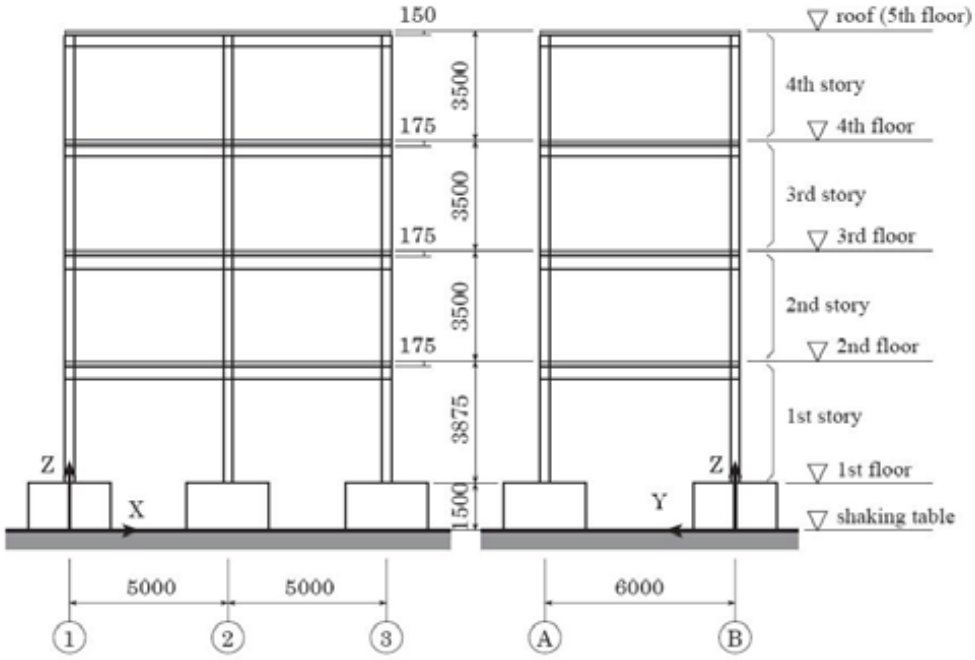

Figure 6.3 Dimension of the 4-story, 2-bay steel structure (unit: mm)

6.3.1. Multi-Scale Model and Instrumentation. A multi-scale model was established in ABAQUS for the 4-story, 2-bay steel building structure. As shown in Figure 6.4 (a), a portion of one corner column in the 1st to 3rd stories and its connecting beams and girders (half members) were considered as "master" members that were represented by many 3-D linear hexahedral elements of type C3D8R in ABAQUS. The remaining members were considered as "slave" members that were represented by 3-D linear beam elements of type B31. Each master member (column or beam or girder) was divided into 10 fiber elements in parallel. Overall, the multi-scale model has a total of 9196 elements, including 556 B31 elements (slave) and 8640 C3D8R elements (master). The slave and master elements were connected together by enforcing a kinematic coupling condition that constrained all six degrees of freedom. The steel material has the modulus of elasticity of 200 GPa (2.9×10^4 ksi), yield strength of 34.95 MPa (5.07 ksi), and density of 33 kg/m^3 (2.06 lb/ft^3). The 60% recorded 1995 Kobe earthquake in Takatori station, Japan, as shown in Figure 6.4 (b), was selected as the earthquake ground

motion input. The same earthquake loads were applied as table excitations during the 3-D shaking table tests [145, 146].

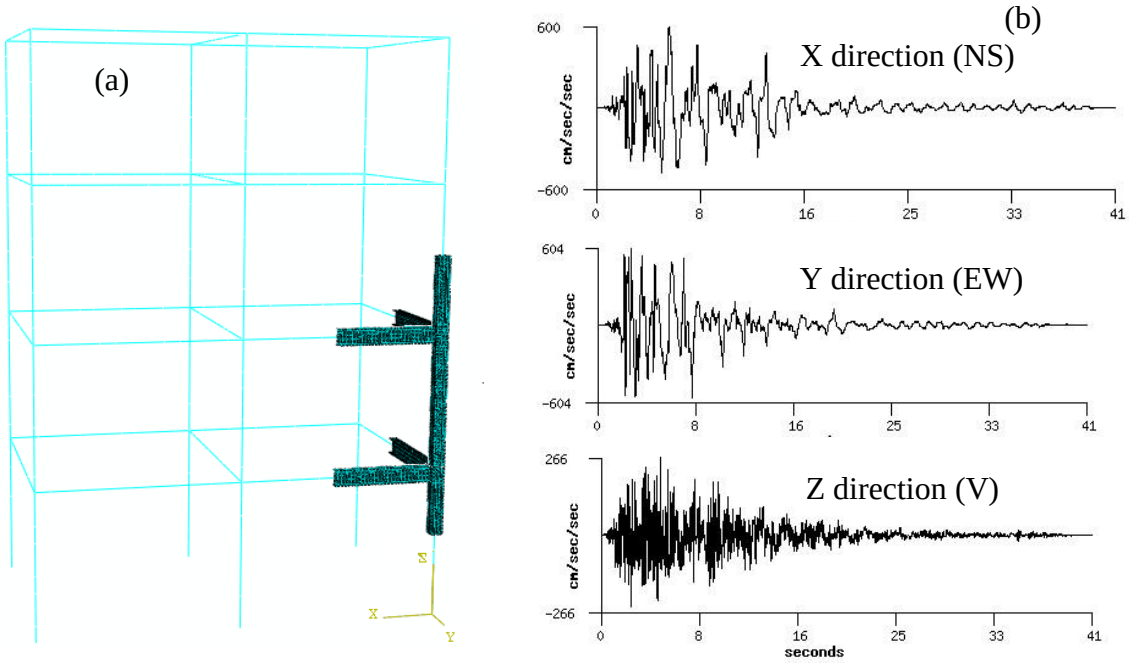

Figure 6.4 Model setup: (a) multi-scale FEM and (b) 1995 Kobe earthquake record, Takatori station

For the shake table test, various sensors were deployed both inside and outside of the building to measure strains, displacements, and 3-D accelerations under the 1995 Kobe earthquake excitation [146, 147]. Figure 6.5 (a) illustrates the locations of accelerometers in the longitudinal direction and Figure 6.5 (b) illustrates the location of laser sensor for displacement measurement and strain gauges. A total of 588 strain gauges were installed in the building model, particularly on the surface of the side and middle columns in the longitudinal direction as illustrated in Figure 6.5 (b). Together with the accelerations recorded on the top floors, the measured strains can be used to evaluate the properties of structural materials for the fiber elements of a master member.

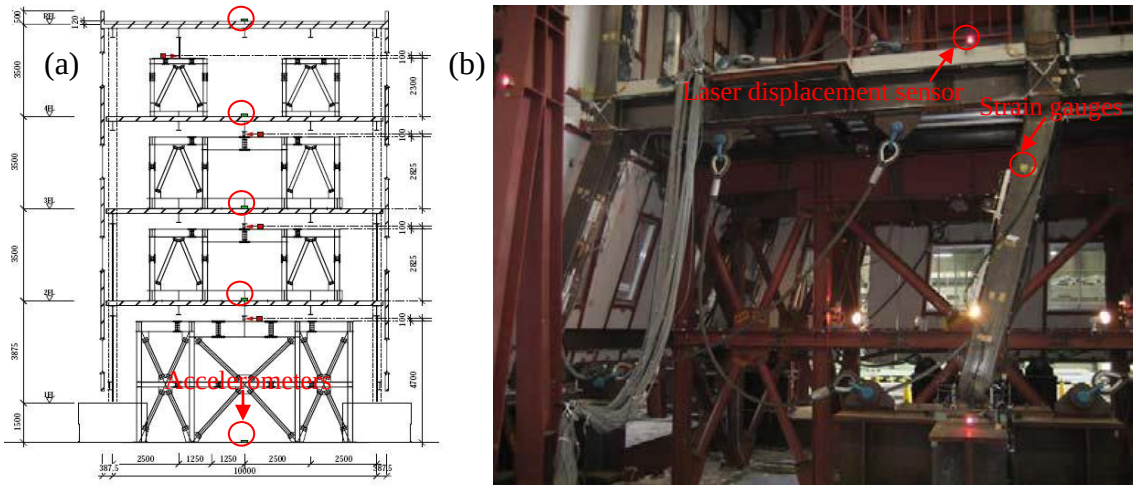

Figure 6.5 Full-scale shake table test [85]: (a) instrumentation and (b) failure mode

6.3.2. Seismic Analysis without Model Updating. Figure 6.6 shows the stress distribution of the 4-story steel structure after 6.3 sec of the earthquake load, which corresponds to the incipient collapse of the structure. With multi-scale modeling, the stress distribution of the structure can be predicted both in large scale for plastic hinge locations and in detail of the formation of the plastic hinges. It can be seen from Figure 6.6 that the plastic hinges are formed both at the bottom and top of the columns and two ends of the beams on the first and second floors.

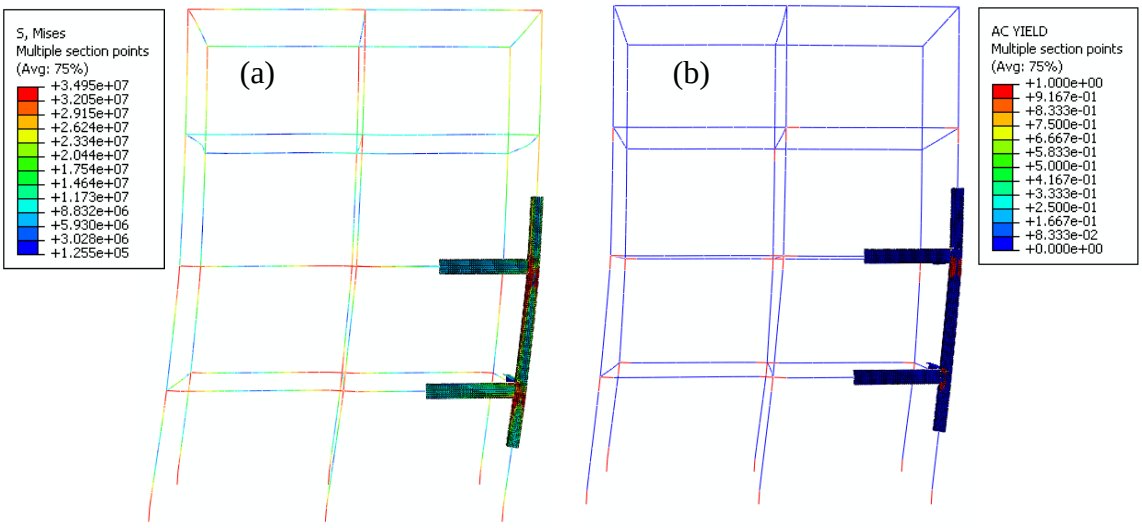

Figure 6.6 Seismic analysis without model updating: (a) Von Misses stress distribution and (b) plastic hinge distribution

Figure 6.7 (a) shows the distribution of plastic hinges in the longitudinal frame, corresponding to the failure mode indicated in Figure 6.5 (b). Figure 6.7 (b) presents the distribution of the modulus of elasticity (E) from the monitored steel beams. As determined from the data in Figure 6.7 (b), a mean value of 202.5 GPa (2.94×10^4 ksi) and a standard derivation of 4.8 GPa (696 ksi) were obtained at the peak of ground motion. On the other hand, the measured data from the two instrumented columns gave a mean modulus of elasticity of 90.8 GPa (1.3×10^4 ksi) and a standard derivation of 1.4 GPa (203 ksi). The stiffness of the columns was more than twice less than that of the beams due to significant inelastic deformation. Therefore, the direct use of steel stiffness for columns without updating in real time would have induced significant errors in simulation. The measured displacements and accelerations were compared with the simulated results and used to validate the developed adaptive multi-scale modeling concept.

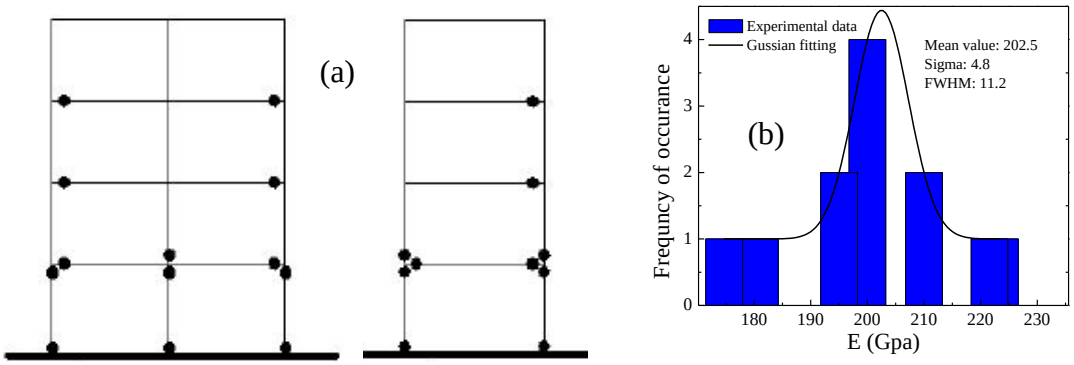

Figure 6.7 Seismic analysis without model updating: (a) detected plastic hinges and (b) material property distribution of the beams

6.3.3. Seismic Analysis with Model Updating. With the estimated material property probability distribution, the material properties of the slave members can then be generated by following reference [149] for the generation of random numbers from the prescribed probability distribution by using Box and Muller method. In this study, only stiffness, E, is considered to be updated to the model analysis. Figure 6.8 (a, b) respectively show the Von Misses stress and plastic hinge distribution of the steel building after the proposed multi-scale model has been updated in real time. By updating

material properties for the fiber elements of "master" members and their corresponding "slave" elements based on the material probability distribution, the plastic hinges are formed at the bottom and top of the 1st-story columns, at two ends of the beams on the 1st and 2nd floors, and at the top of the 2nd-story and 3rd-story columns. By comparing Figure 6.6 (b) and Figure 6.8 (b) with Figure 6.7 (a), it can be seen that the model updating results in a more accurate prediction of plastic hinges.

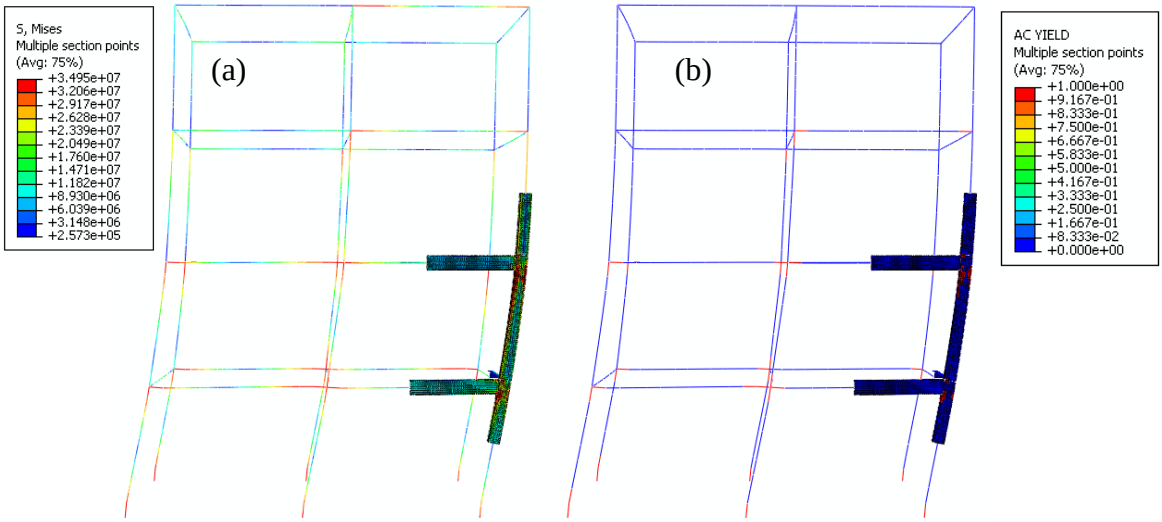

Figure 6.8 Seismic analysis with model updating: (a) Von Misses stress distribution and (b) plastic hinge distribution

Table 6.1 compares the X-direction (North-South), relative displacements simulated with four analysis techniques and their corresponding relative errors from experimental results. The four techniques include two multi-scale model analyses with and without model updating, pre-test simulations [85], and post-test calibrated simulations [85]. It is clearly seen from Table 6.1 that the updating of the multi-scale model yielded significantly more accurate relative displacement predictions with relative errors of less than 12%. On the 4th floor, the relative error with the adaptive multi-scale modeling drops below 5%, the lowest of all numerical techniques. Among all four techniques, the adaptive multi-scale model analysis leads to the least relative error on all building floors. In particular, the relative displacement errors on all floors predicted by the adaptive multi-scale model analysis are significantly smaller than those of the

calibrated simulations after the shaking table test [85]. Therefore, the proposed adaptive multi-scale model is a viable approach for an accurate prediction of structural behaviors of large-scale structures under earthquake excitations.

Table 6.1 Comparison among X-direction (NS) relative displacements determined from various analyses (mm) and their relative errors

Floor Level	Measured relative displacement	Simulated relative displacement		Relative error (%)			
		Without updating	With updating	Without updating	With updating	Pre-test simulation	Post-test simulation
1	0	0	0	-	-	-	-
2	75	64	84	15	12	71	15
3	135	110	146	19	8	61	13
4	177	131	170	26	4	59	11
5	200	141	180	30	10	61	11

6.4.PROGRESSIVE COLLAPSE ANALYSIS OF A STEEL BUILDING UNDER A POST-EARTHAKE FIRE CONDITIONS

6.4.1. Progressive Collapse of Steel Structures. Progressive collapse is known as the collapse of all or a large part of a structure precipitated by damage or failure of a relatively small part of it [2]. The phenomenon of progressive failure matters because this process is often associated with a disproportionate design/structure. For structures that are susceptible to progressive failures, minor damage may trigger catastrophic consequences. For example, a 7-story steel building in the University of Aberdeen Zoology, Aberdeen, Scotland, completely collapsed during construction on November 1, 1966, resulting in five fatalities and three injuries. This event represents the first example of the progressive collapse of a steel-framed building. The total collapse was caused by the fatigue effect on the low quality welds of girders as a result of wind-induced frequent oscillations. On September 11, 2001, the twin building of the World Trade Center, New York, the United

States of America, collapsed progressively following a terrorist attack due to the subsequent fires, causing 2,752 deaths. This tragedy attracted a worldwide attention to the progressive failure of steel structures in harsh environments. After three years of investigation for the World Trade Center collapse by the National Institute of Standards and Technology (NIST), the cause for the initiation of the progressive collapse was attributed to the instability of the attacked floors by the loss of fire protection from the impact and explosion and the creep buckling induced by the prolonged heating of steel columns up to 800 ℃. The falling superstructure as a rigid body further induced dynamic overloads on the lower floors, leading to a complete collapse of the entire building system [3].

Therefore, the behavior of steel structures in harsh environments such as earthquakes, explosions, and fires becomes a significant concern in the safety evaluation of steel structures. Critical buildings, such as hospitals and police stations, must remain functional even in harsh environments, for example, immediately following a major earthquake or a terrorist attack or its subsequent fire condition. Due to earthquake or explosion effects, buildings often experience inelastic behavior (large strains), leading to progressive collapses. During this process, tenants could be injured and trapped in the collapsed buildings. The subsequence fire induces a high temperature environment, accelerates the process of collapses in steel structures, and results in increasing difficulties for post-earthquake or post-attack rescues. Therefore, a numerical prediction of the progressive failure based on limited measurements in real time is of paramount importance to post-earthquake or attack responses and evacuation in earthquake-prone regions. An accurate assessment and a reasonable numerical prediction of the progressive failure of the involved buildings in these harsh conditions can assist fire fighters in their rescue efforts.

Based on the temperature-dependent model updating technique developed in Chapter 5 and the adaptive multi-scale modeling technique developed in Sections 6.2 and 6.3, the progressive failure mode of a steel building under post-earthquake fire conditions can be predicted accurately. In this section, a 4-story 2-bay steel building is considered as an example for the prediction of a progressive failure in simulated fire conditions. The structure modeling and numerical analysis are conducted with ABAQUS.

6.4.2. FEM of Steel Structures for Progressive Collapse Studies. The single-story single-bay steel frame tested in Chapter 4 and analyzed in Chapter 5 was expanded into a 4-story 2-bay steel building in this study. All the floor beams are made of A36 steel S3×5.7 hot-rolled sections. All the columns are made of A36 steel S5×10 hot-rolled sections. To reduce the computation time and cost, a multi-scale FEM was established with one bay of the first story of the steel building simulated by 3-D fiber elements ("master" members) and the other structural components simulated by 3-D beam elements ("slave" members), as shown in Figure 6.9 (a). The "master" members were modeled with linear hexahedral elements, C3D8T in ABAQUS, and the "slave" members were modeled with linear beam elements, B31 in ABAQUS. The multi-scale model includes 10,630 C3D8T and 799 B31 elements, amounting to a total of 11,429 elements. The bottom ends of all columns in the first story were fixed to the ground to simulate the boundary condition of typical steel buildings in practical applications.

For simplicity, the post-earthquake fire condition is represented by lateral loads and temperature effects (or temperature boundary conditions). The lateral loads were first applied on the first floor both in X and Z directions, and induced a plastic strain larger than 0.5% at the bottom end of the column. The temperature effects that were represented by the temperature distribution in Figure 5.9 were then introduced in one of the columns in the first story. Figure 6.9 (b) shows the temperature distribution in the entire steel structure at an elevated temperature of 550 ℃ (1025 ℉), including an insert for close-up view. Fire was considered to start around the exterior column in the first story as illustrated in Figure 6.9 (b). The temperature loading profile of the fire is the same as shown in Figure 4.14 (a). In addition to the lateral loads and tempeature effects, vertical loads were applied on each floor beam to simulate the dead load from each floor, which is identical to that used in Chapter 5 for the single-story single-bay steel frame.

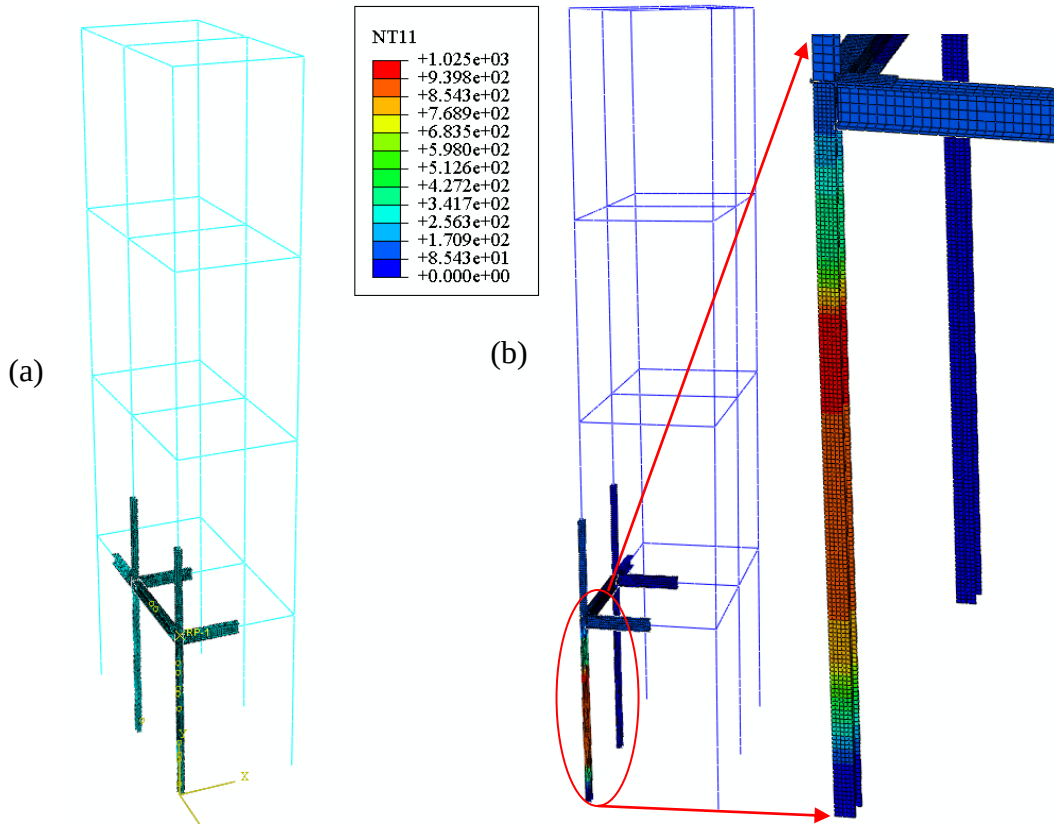

Figure 6.9 Modeling of a 4-story 2-bay steel building: (a) multi-scale FEM and (b) overall temperature distribution with an enlarged view of thermal loading zone (unit: ℉)

6.4.3. Damage and Failure Criteria. The commercial software, ABAQUS, offers various general capabilities for the modeling of damage and failure in engineering structures [129]. However, to predict the progressive collapse of a steel structure, material failures related to a complete loss of loading capacity from a progressive degradation of material stiffness must be defined in the FEM. In this study, a ductile fracture damage model was applied to simulate the progressive material damage. The ductile fracture damage as shown in Figure 6.10 (a) for strain-hardening materials includes the undamaged constitutive behavior or perfect elastic-plastic constitutive relation with respect to temperature dependence, damage initiation (point A), damage evolution (path A to B), and choice of material removal (point B) [79]. In Figure 6.10 (a), σ_{y0} and $\bar{\varepsilon}_0^{pl}$ are the yield strength and the equivalent plastic strain at the onset of damage, respectively, and $\bar{\varepsilon}_f^{pl}$ is the equivalent plastic strain at failure, which means an overall

damage variable D = 1. The overall damage variable, D, captures the combined effect of all active damage mechanisms and is computed in terms of the individual damage variables. The value of the equivalent plastic strain at failure, $\bar{\varepsilon}_f^{pl}$, depends on the characteristic length of the element [79].

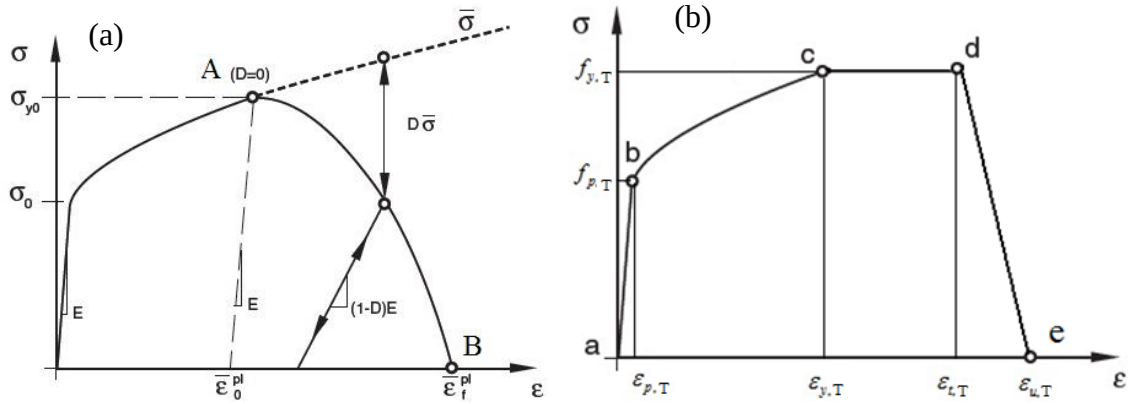

Figure 6.10 Ductile fracture damage: (a) strain hardening material and (b) classic elastic-plastic material [70]

In this study, a ductile damage criterion is used to define the initiation of damage. To do this, the stress-strain relationship of carbon steel with consideration of high temperature material degradation was modified according to the Euro-Code EN 1993-1-2 [70] and shown in Figure 6.10 (b). The assumed undamaged constitutive behavior of the steel (point a to d in Figure 6.10 (b)) is the same as shown in Figure 5.2, Table 5.1, and Figure 5.3 (a); it represents a temperature-dependent constitutive behavior. Unlike Chapter 5 where the plastic strain of steel goes up to infinity or $\varepsilon_{t,T} = \infty$, here the strain at the initiation of damage, $\bar{\varepsilon}_0^{pl}$, is set to be 0.15 for all elevated temperatures or $\varepsilon_{t,T} = 0.15$. Thus, for the steel used in this study, the damage initiation point (A in Figure 6.10 (a)) is set to be point d in Figure 6.10 (b), where the strain and stress are equal to $\varepsilon_{t,T}$ and yielding strength $f_{y,T}$, respectively.

In addition to the ductile damage criteria, the evolution of damage must also be discussed for the progressive failure analysis of materials. In this study, a damage evolution is assumed to be linear according to the Euro-Code EN 1993-1-2 [70] and the

point when an element can be deleted, $\bar{\varepsilon}_f^{pl}$, is set as 0.2 regardless of the elevated temperature. Therefore, the effective plastic displacement, $\bar{u}_f^{pl}$, at the point of failure can be related to the ultimate strain, $\bar{\varepsilon}_f^{pl}$, by the characteristic length L of the element as follows:

$$\bar{u}_f^{pl} = L\bar{\varepsilon}_f^{pl} \tag{39}$$

The last step for a progressive failure and damage analysis of materials is to delete an element once the maximum degradation of the element, D_{max}, is reached. The maximum degradation is an upper bound of the material progressive failure to the overall damage variable, D. In this study, the D_{max} is set to be 1.0 as an element removal criterion. In a heat transfer analysis, the thermal properties of the element material are not affected by the progressive damage of the material stiffness until the condition for the element deletion is met and the thermal contribution of the element is thus removed [79].

6.4.4. Progressive Failure Analysis with Adaptive Multi-scale Modeling. The process of adaptive multi-scale modeling for progressive failure analysis is similar to that for structural behavior simulations summarized in Figure 6.2. For convenience, Figure 6.11 presents a slightly modified flow chart of the analysis procedure, explicitly accounting for the ductile damage under temperature loading. Through the "master" members, the column that is directly exposed to a fire condition is evaluated for a potential progressive failure, which is indicated by plastic strain distribution, temperature distribution, damage initiation, and local bulking. According to the damage evolution criterion, the elements that are stressed for 20% or more strains are deleted from the FEM. In doing so, the progressive failure of the entire building can be predicted and validated against experimental data if available.

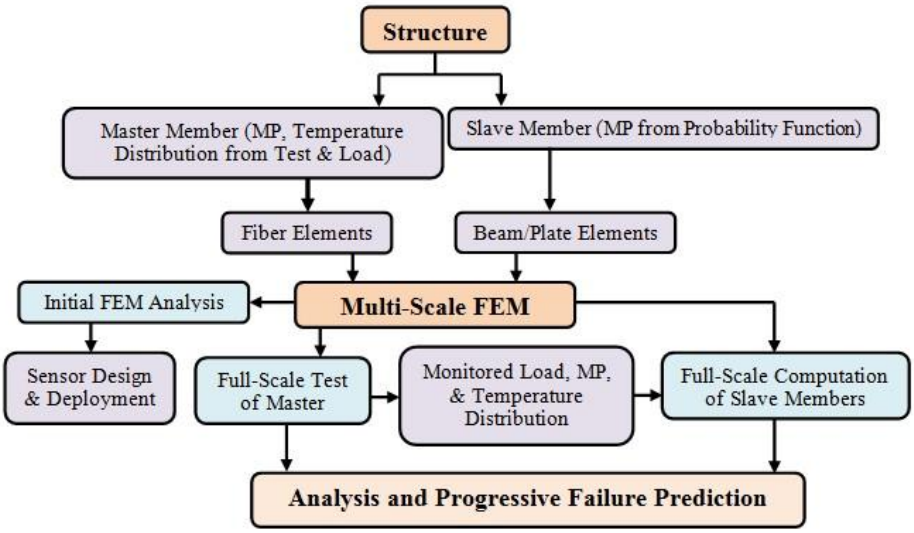

Figure 6.11 Flow chart of adaptive multi-scale modeling and progressive failure analysis

6.4.5. Progressive Failure Analysis Results and Discussion. Figure 6.12 shows a plastic strain distribution over the entire structure when temperature at the exterior column of the 1st story reaches 700 ℃ (1292 ℉). With a direct exposure to the fire condition, a portion of the column loses its stability and experiences local buckling. The maximum plastic strain is more than 28.5% or 285,000 με.

With accumulative damage of the ductile steel material, the elements of the exterior column directly exposed to the fire condition, whose plastic strain exceeds 20% or 200,000 με, can no longer support gravity and thermal loads. These elements were removed from the FEM in the following progressive failure analysis. Figure 6.13 shows the Von Misses stress distribution over the entire struture after deletion of the failed elements. With loss of the column directly exposed in fire, the overall load on the entire building was redistributed and two columns in the 2nd story as circled in Figure 6.13 started yeilding and lost their load-bearing capacity.

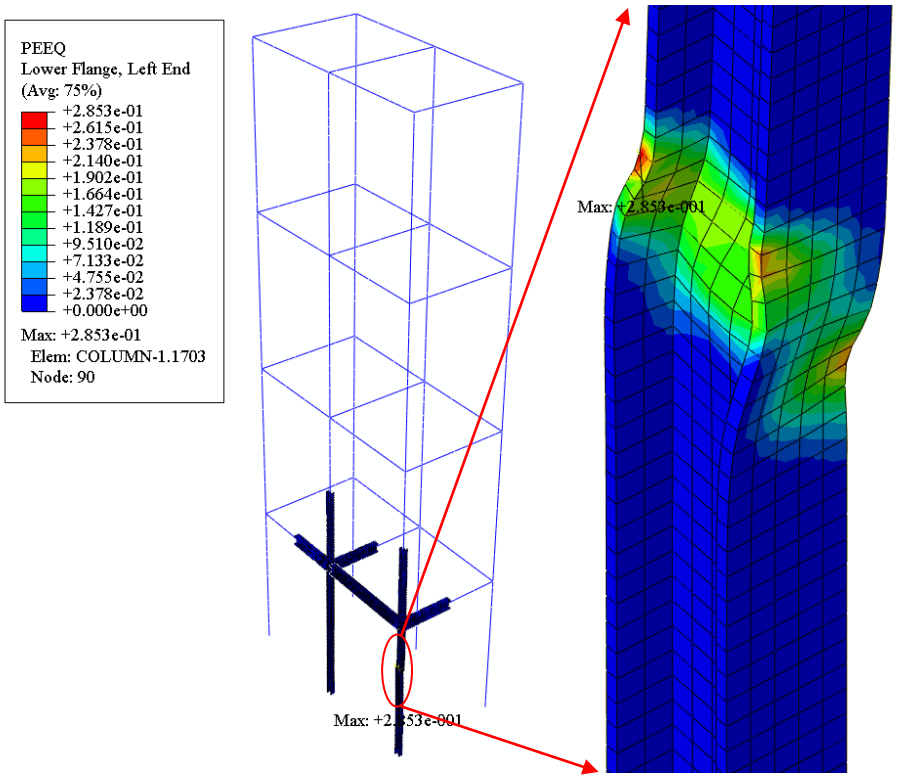

Figure 6.12 Initial column failure with an enlarged view of local buckling

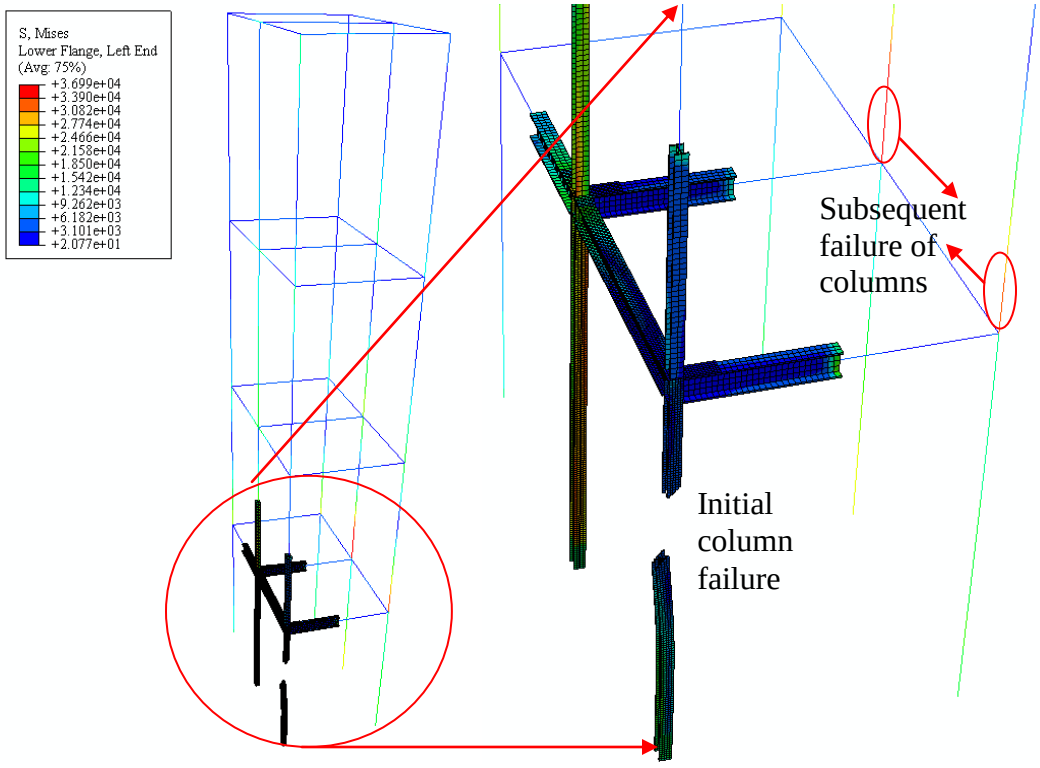

Figure 6.13 Subsequent failure of columns

After the three columns in the 1st and 2nd stories have lost their load-bearing capacity, the overall load on the entire building was further redistributed, resulting in the overall Von Misses stress distribution as illustrated in Figure 6.14 and causing the failure of additional four columns as indicated in the insert of Figure 6.14. In this case, 4 out of 6 columns in the 2nd story failed and the upper substructure started crashing into the 1st story, leading to the collapse of the entire steel building.

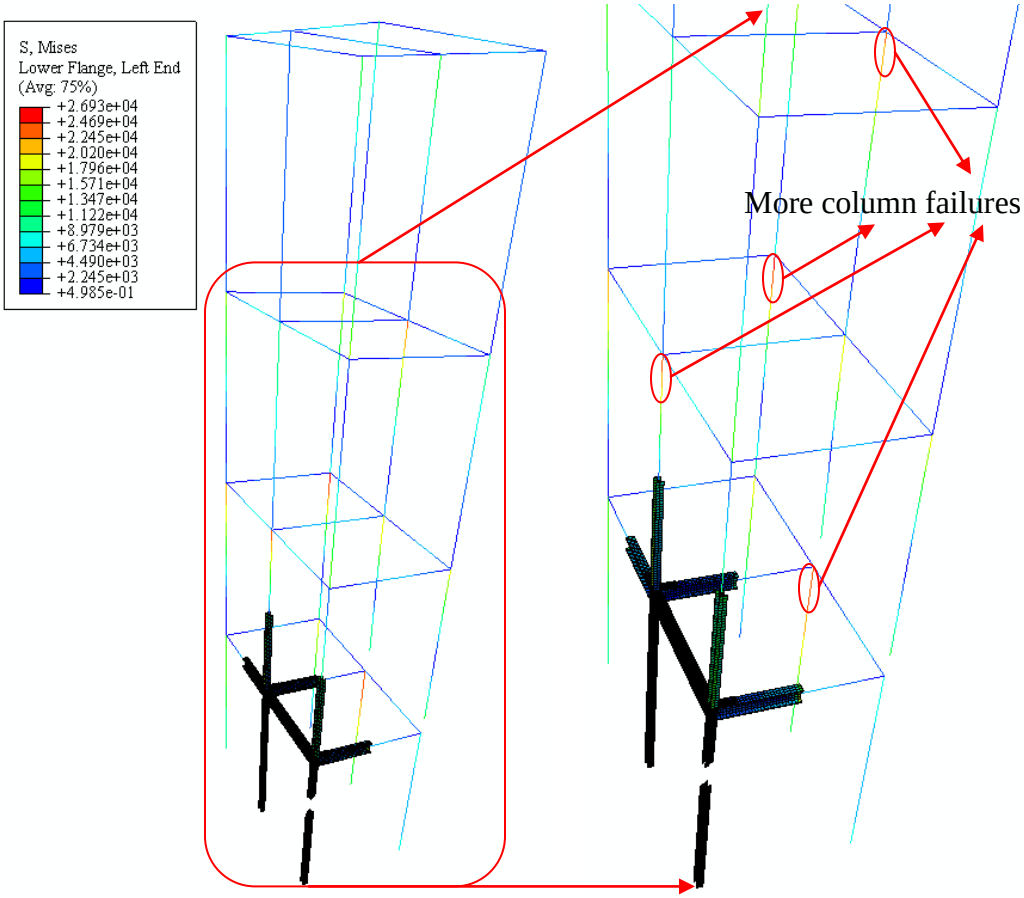

Figure 6.14 More column failures with an enlarged view of failure locations

6.5.SUMMARY ABOUT THE ADAPTIVE MULTI-SCALE MODELIING

In this chapter, an adaptive multi-scale model with material property and external load updating in real time is developed and successfully demonstrated in a practical application scenario through hybrid simulations. An engineering structure is divided into a representative substructure, which is fully instrumented for its actual behavior, and the

remaining substructures that are computationally simulated for their predicted behavior. Both the material properties (stiffness and yielding strength) and service environments (temperature distribution) of the representative substructure are introduced to the modeling of other substructures in real time based on the premise that all the substructures are built with the same material using identical construction procedures and methods.

To validate the developed concept, adaptive multi-scale modeling has been applied to establish an FEM of the full-scale 4-story, 2-bay steel building that was tested experimentally on the 3-D shake table in Miki City, Hyogo Prefecture, Japan for earthquake effects. The simulated structural responses with the proposed adaptive multi-scale model were found in good agreement with the experimental results. In fact, the prediction accuracy of the multi-scale model is even significantly higher than that by the FEM that has been calibrated with the shake table test data.

With the validated adaptive multi-scale modeling technique, a progressive collapse analysis of another 4-story, 2-bay steel building structure under post-earthquake fire conditions was performed. The steel building was expanded from the laboratory tested steel frame in Chapter 5 so that some levels of physical understanding on the high temperature behavior of the steel frame can be inferred from the previous study. Ductile damage criteria and buckling failure criteria were considered in the progressive damage and failure analysis of the steel structure. The progressive failure path of the 4-story, 2-bay steel building was identified successfully. The adaptive multi-scale model can thus be used in practice to develop the best rescue route in critical facilities in the event of a post-earthquake fire.

7. CONCLUSIONS AND FUTURE WORK

7.1.MAIN FINDINGS FROM THE OVERAL DISSERTATION WORK

In this dissertation, a novel comprehensive optical fiber sensing system is proposed for real-time monitoring of steel buildings in harsh environments, for example, in the event of a post-earthquake fire. The key technical challenge in sensor innovation and development is a simultaneous measurement of large strain and high temperature. To cost-effectively provide an overall understanding of building behaviors with limited sensor placements, an adaptive multi-scale finite element modeling technique is developed in the context of hybrid simulations with combined instrumentation and computation and used to update both material properties and external loads of a building structure in real time. The multi-scale modeling technique is applied to investigate the progressive collapse of a 4-story steel building in high temperature environments. Based on the above comprehensive investigations both numerically and experimentally, several conclusions can be drawn from this study:

1. A movable extrinsic Fabry-Perot interferometer (EFPI) optical fiber sensor was developed with a novel three-layer packaged structure for large strain measurements in high temperature. The packaged EFPI sensor can measure strains as large as 12% or 120,000 με. Three data processing methods investigated allow the strain measurement resolution of a movable EFPI sensor to be selective as needed in various applications. Together, the three methods with frequency, period, and phase tracking have an adjustable strain resolution ranging from 6,000 με to 10 με.
2. Two types of optical fiber sensors were developed for simultaneous large strain and high temperature measurements: a single long period fiber grating (LPFG) sensor and a hybrid EFPI/LPFG sensor. By using two different cladding modes, the single LPFG sensor can simultaneously measure a strain of 2.4% or 24,000 με and temperature of 800 ℃ (1472 ℉). To increase the dynamic range of strain sensing, the movable EFPI sensor and the LPFG sensor were integrated into a hybrid EFPI/LPFG sensor. The hybrid sensor can measure 12% strain and

temperature as high as 800 ℃ (1472 ℉) at the same time. It is recommended for the progressive collapse assessment of steel structures in harsh environments.

3. The spatial frequency division and wavelength division multiplexing methods are applied to link individual hybrid EFPI/LPFG sensors into a quasi-distributed optical fiber sensor network. The signal demodulation between two hybrid sensors and between the EFPI and LPFG components has been experimentally demonstrated to be quite successful, making the sensor networking feasible in large-scale civil infrastructure applications. Experimental results indicated that the optical fiber sensor network can monitor structural behaviors of a steel frame structure at a strain of more than 10% or 100,000 με and temperature of up to 800 ℃ (1472 ℉) and its relative error of strain and temperature measurements is within 10% in the progressive failure investigation of the steel frame in harsh environments.
4. A temperature-dependent finite element model updating technique was developed and implemented in real time during the testing of a single-story single-bay steel frame. The model updating algorithm was formulated by minimizing the total error of strain and temperature predictions. Test results verified that the proposed model updating can significantly reduce the relative error of strain predictions from over 75% to below 20%.
5. An adaptive multi-scale modeling technique was developed for a hybrid simulation of structures, allowing both material properties and external loads updated in real time. It consisted of a representative substructure fully instrumented for its actual behavior and the remaining substructures computationally simulated for its predicted behavior. The adaptive multi-scale modeling technique was validated with the seismic testing of a full-scale 4-story, 2-bay steel building on the E-Defense shake table in Japan. Its seismic response predictions are more accurate than those from the conventional finite element method even with post-earthquake calibrations. The validated technique was successfully applied to assess the progressive collapse of another 4-story, 2-bay steel structure under high temperature effects.

For more details, the above main findings can be referred to a number of papers that have been published or submitted for potential publication during the Ph.D. dissertation work. These papers are listed as follows:

1. G. Chen, H. Xiao, **Y. Huang**, Z. Zhou, and Y. Zhang (2009). "A novel long-period fiber grating optical sensor for large strain measurement," *Proceedings of SPIE Annual Symposium on Smart Structures and NDE*, March 8-12, 2009, Vol. 7292, No. 7292-2, San Diego, California, USA.
2. **Y. Huang**, Z. Zhou, Y. Zhang, G. Chen, and X. Hai (2009). "A novel long period fiber grating sensor for large strain measurement in high temperature environment," *Proceedings of the 2009 ANCRiSST Meeting*, July 2009, Boston, USA.
3. **Y. Huang**, Z. Zhou, Y. Zhang, G. Chen, and H. Xiao (2010). "A temperature self-compensated LPFG sensor for large strain measurements at high temperature," *IEEE Transactions on Instrumentation and Measurement*, Vol. 59, No.11, pp. 2997-3004.
4. **Y. Huang**, T. Wei, Z. Zhou, Y. Zhang, G. Chen, and H. Xiao (2010). "An extrinsic Fabry–Perot interferometer-based large strain sensor with high resolution," *Measurement and Science Technology*, Vol. 21, pp.105308-105318.
5. Y. Zhang, Y. Li, T. Wei, X. Lan, **Y. Huang**, G. Chen and H. Xiao (2010). "Fringe visibility enhanced extrinsic Fabry-Perot interferometer using a graded index fiber collimator," *IEEE Photonics Journal*, Vol. 2, No. 3, pp.469-481.
6. G. Chen, H. Xiao, **Y. Huang**, Y. Zhang, and Z. Zhou (2010). "Simultaneous strain and temperature measurement using long-period fiber grating sensors," *Proceedings of SPIE Annual Symposium on Smart Structures and NDE*, March 7-11, 2010, Vol. 7649, No. 7649-1, 8p., San Diego, California, USA.
7. **Y. Huang**, G. Chen, H. Xiao, Y. N. Zhang, and Z. Zhou (2011). "A quasi-distributed optical fiber sensor network for large strain and high temperature measurement of structures," *Proceedings of SPIE Annual Symposium on Smart Structures and NDE*, March 6-10, 2011, Vol. 7983, No.7983-40, 12p., San Diego, California, USA.

8. **Y. Huang**, W. Bevans, Z. Zhou, H. Xiao, and G. Chen (2011). "Structural behavior evaluation of a steel frame in simulated post-earthquake fire environment using a comprehensive sensing network," *Proceeding of the 2011 ANCRiSST Meeting*, Paper No.38, 12p., Dalian, China.
9. G. Chen, **Y. Huang**, and H. Xiao (2012). "Steel building assessment in post-earthquake fire environments with optical sensors," Book Chapter 19 in *Earthquake Resistant Structures – Design, Assessment and Rehabilitation*, Edited by Abbas Moustafa, In-Tech Press, ISBN 978-953-51-0123-9, pp. 481-506.
10. **Y. Huang**, W. Bevans, Z. Zhou, H. Xiao, and G. Chen (2012). "Experimental validation of finite element model analysis of a steel frame in simulated post-earthquake fire environments," *Proceedings of SPIE Annual Symposium on Smart Structures and NDE*, March 11-15, 2012, Vol. 8345, No.8345-23, 12p., San Diego, California, USA.
11. G. Chen and **Y. Huang** (2012). "Adaptive multi-scale modeling of structures under earthquake loads," *Proceedings of the 15th World Conference on Earthquake Engineering*, September 24-28, 2012, Lisbon, Portugal.
12. **Y. Huang**, X. Fang, Z. Zhou, H. Xiao, and G. Chen (2012). "Large-strain optical fiber sensing and real-time finite element model updating of steel structures under high temperature effects," Submitted to *Smart Materials and Structures*.

7.2.FUTURE WORK

The optical fiber sensors, sensing network, and the adaptive multi-scale modeling technique proposed in this study have been validated in laboratory. For practical applications, implementation issues must be further studied in the future. Specifically, future research can be directed to address the following topics:

(1) A more robust sensing network design based on the developed optical fiber sensors is desirable in practical applications. It can be achieved by improving sensor ruggedness, optical fiber connection integrity, and network redundancy so that the system reliability of a sensing network can be enhanced. Ideally, a sensor network can be designed with fault detection and reorganization capabilities.

(2) The novel optical fiber sensors and sensing network should be further validated for earthquake effects under dynamic loading such as shake table tests.

(3) The novel sensors and sensing network should be further tested in real fire environments. In addition to the high temperature effect addressed in this dissertation, a real fire induces smoking and fire ball effects on a steel structure, a potentially harsher environment for sensor design. More importantly, the temperature of a structure in a fire increases rapidly, requiring a sensing system further checked against fire design specifications.

(4) The progressive collapse process of a 4-story, 2-bay steel building investigated in this dissertation is predicted by numerical simulations only. To ultimately validate the proposed adaptive multi-scale modeling technique, physical tests of a large- or full-scale steel building are necessary.

(5) The proposed adaptive multi-scale model can be further developed by introducing a spatially-correlated material property and/or external input updating strategy for large-scale civil infrastructure.

BIBLIOGRAPHY

[1] Sun, R., Huang, Z., Burgess, I. W. (2012). "Progressive Collapse Analysis of Steel Structures under Fire Conditions." *Engineering Structures*, 34, 400–413.

[2] Starossek, U., (2007). "Typology of Progressive Collapse." *Engineering Structures*, 29, 2302–2307.

[3] Bazant, Z. P., Zhou, Y. (2002). "Why Did the World Trade Center Collapse? Simple Analysis." *ASCE Journal of Engineering Mechanics*, 128(1), 2–6.

[4] Balageas, D., Fritzen, C. P., and Guemes, A. (2006). *Structural Health Monitoring*, ISTE Lt, Newport Beach, CA.

[5] Thomson, W. (1857). "On the Electro-dynamic Qualities of Metals." *Proceedings of the Royal Society A*, 8, 46-50.

[6] Schedin, E., and Melander, A. (1986). "The Evaluation of Large Strains from Industrial Sheet Metal Stampings with a Square Grid." *Journal of Applied Metal Working*, 4 (2), 143-156.

[7] Dupre. J. C., Cottron, M., and Lagarde, A. (1995). "Grating Interrogations: from Small to Large Strain Measurement." *Experimental Mechanics*, 35(2), 153-158.

[8] Takahashi, T., and Aoki, I. (1996). "Development of Analyzing System Applicable for Large Plastic Deformation." *Proc., Technology of Plasticity: Advanced Technology of Plasticity*, JSTP, Japan, 583-590.

[9] Sawada, T., and Sakamoto, M. (2004). "High Resolution of Large Strain with Fourier Phase Correlation Method by Image Sensing Camera." *Steel Grips*, 2, 681-685.

[10] Rotinat,R., Ti ébi, R., Valle, V., and Dupr é, J. C. (2001). "Three Optical Procedures for Local Large-strain Measurement." *Strain*, 37(3), 89-98.

[11] Easerling, K. E. (1963). "High Temperature Resistance Strain Gauges." *Britain Journal of Applied Physics*, 14(2), 79-84.

[12] Gregory, O. J., and Chen, X. M. (2007). "A Low TCR Nano-composite Strain Gage for High Temperature Aerospace Applications." *Proc., Sensors*, IEEE, GA, 624-627.

[13] Udd, E. (1991). *Fibre Optic Sensors*, John Wiley and Sons, New York.

[14] Claus, R., Matias, I., and Arregui, F., (2001). *Handbook of Fiber Optics Vol 3*, McGraw Hill, New York.

[15] Gholamzadeh, B., and Nabovati, H. (2008). *Fiber Optic Sensors*, World Academy of Science, Engineering and Technology, NM.

[16] Li, X., Deng, Y., Yu, Y., Wang, X., and Li, J. (2008). "Microbending Optical Fiber Sensors and Their Applications." *Proc., Advanced Infocomm Technology,* ACM, New York, 89-96.

[17] Yao, S. K., and Asawa, C. K. (1983). "Fiber Optical Intensity Sensors." *IEEE Journal of Selected Areas in Communication*, 1(3), 562 – 575.

[18] Yuan. J., and El-Sherif, M. A. (2003). "Fiber-optic Chemical Sensor Using Polyaniline as Modified Cladding Material." *IEEE Sensors Journal*, 3(1), 5-12.

[19] Spillman, W. B., and McMahon, D. H. (1980). "Frustrated-total-internal-reflection Multimode Fiber-optic Hydrophone." *Applied Optics*, 19(1), 113-117

[20] Connelly, M. C. (2005). *Fiber Sensors*, Elsevier Ltd., Limerick, UK.

[21] Senior, J. M. , Murtaza, G., Stirling, A. I., and Wainwright, G. H. (1992). "Single LED Based Dual Wavelength Referenced Optical Fibre Sensor System Using Intensity Modulation." *Optics & Laser Technology*, 24(4), 187–192.

[22] Kashyap, R. (1999). *Fiber Bragg Gratings*, Academic Press, San Diego, CA.

[23] Hill, K. O., Fujii, Y., Johnson, D. C., and Kawasaki, B. S. (1978). "Photosensitivity in optical fiber waveguides: application to reflection fiber fabrication." *Applied Physics. Letter*, 32 (10), 647-650.

[24] Meltz, G. (1989). "Formation of Bragg Gratings in Optical Fibers by a Transverse Holographic Method." *Optics Letters*, 14 (15), 823-825.

[25] Davis, C. M., Carome, E. F., Weik, M. H., Ezekiel, S., Einzig, R. E. (2002). *Handbook of Fiber Optic Sensors Technology*, Optical Technologies, Dynamic System Inc., Herndon, VA.

[26] Koo, K. P., Tveten, A. B., and Vohra, S. T. (1999). "Dense Wavelength Division Multiplexing of Fibre Bragg Grating Sensors Using CDMA." *Electronics Letter*, 35(2), 165-167.

[27] Cooper, D. J. F., Coroy, T., and Smith, P. W. E. (2001). "Time-division Multiplexing of Large Serial Fiber-optic Bragg Grating Sensor Arrays." *Applied Optics*, 40(16), 2643-54.

[28] Bhatia, V., and Vengsarkar, A. (1996). "Optical Fiber Long Period Grating Sensors." *Optics Letters*, 21, 692-694.

[29] Vengsarkar, A. M., Pedrazzani, J. R. , Judkins, J. B., Lemaire, P. J. , Bergano, N. S., and Davidson, C. R., "Long-period Fiber-grating-based Gain Equalizers." *Optics Letters*, 21(5), 336-338.

[30] Guan, B. O., Tam, H. Y., Ho, S. L., Liu, S. Y., and Dong, X. Y. (2000). "Growth of Long-period Gratings in H_2-loaded Fiber after 193 nm UV Inscription." *IEEE Photonics Technology Letters*, 12, 642–644.

[31] Davis, D. D., Gaylord, T. K., Glytsis, E. N., Kosinski, S. G., Mettler, S. C., and Vengsarkar, A. M. (1998). "Long-period Fiber Grating Fabrication with Focused CO_2 laser Beams." *Electronics Letters*, 34, 302-303.

[32] Shu, X. W., Zhang, L., and Bennion, I. (2001). "Fabrication and Characteristics of Ultra-long-period fiber Gratings." *Optics Communications*, 203, 277-281.

[33] Shu, X. W., Zhang, L., and Bennion, I. (2002). "Sensitivity Characteristics of Long-Period Fiber Gratings." *Journal of Light-wave Technology*, 20(2), 255-266.

[34] Huang, Y., Zhou, Z., Zhang, Y., Chen, G., and Xiao, H. (2010). "A Temperature Self-compensated LPFG Sensor for Large Strain Measurements at High Temperature." *IEEE Transaction of Instrumentation and Measurements*, 50(11), 2997-3004.

[35] Huang, Y., Chen, G., Xiao, H., Zhang, Y., and Zhou, Z. (2011). "A Quasi-distributed Optical Fibre Sensor Network for Large Strain and High-temperature Measurements of Structures." *Proc., SPIE*, CA, 17-27.

[36] Wang, Y. (2010). "Review of Long Period Fiber Gratings Written by CO_2 Laser." *Journal of Applied Physics*, 108, 81101-18

[37] Davis, D. D., Gaylord, T. K., Glytsis, E. N., and Mettler, S. C. (1999). "Very-high-temperature Stable CO_2-laser-induced Long-period Fibre Gratings," *Electronics Letters*, 35, 740-743.

[38] Zhu, Y., Shum, P., Bay, H. W., Yan, M., Yu, X., Hu, J., Hao, J., and Lu, C. (2005) "Strain-insensitive and High-temperature Long-period Gratings Inscribed in Photonic Crystal Fiber." *Optics Letters*, 30(4), 367-369.

[39] Wang, Y. P., Xiao, L., D. Wang, N., and Jin, W. (2006). "Highly Sensitive Long-period Fiber-grating Strain Sensor with Low Temperature Sensitivity." *Optics Letters*, 31(23), 3414-3416.

[40] Peshko, I., Cherry, O., Rutkevich, T., Hockley, B., and Rubtsov, V. (2005). "Long-period Gratings in Optical Fibres for Chemical Sensing Applications." *Measurement Science and Technology*, 16, 2221–2228.

[41] Corres, J. M., Matias, I. R., Villar, I., and Arregui, F. J. (2007). "Design of pH Sensors in Long-Period Fiber Gratings Using Polymeric Nano-coatings." *IEEE Sensors Journal*, 7(3), 455-463.

[42] Rindorf, L., Jensen, J. B., Dufva, M., Pedersen, L. H., Høiby, P. E., and Bang, O. (2006). "Photonic Crystal Fiber Long-period Gratings for Biochemical Sensing." *Optics Express*, 14(18), 8224-8231.

[43] Longhurst, R. S. (1967). *Geometrical and Physical Optics*, Longmans, London.

[44] Choi, H. Y., Kim, M. J., and Lee, B. H. (2007). "All-fiber Mach-Zehnder Type Interferometers Formed in Photonic Crystal Fiber." *Optics Express*, 15(9), 5711-20.

[45] Yuan, L., Yang, J., Liu, Z., and Sun, J. (2006). "In-fiber Integrated Michelson Interferometer." *Optics Letters*, 31(18), 2692-94.

[46] Yoshino, T., Kurosawa, K., and Ose, T. (1982). "Fiber-optic Fabry-Perot Interferometer and Its Sensor Applications." *IEEE Transactions on Microwave Theory and Techniques*, MTT-30(10), 1612-21.

[47] Culshaw, B. (2006). "The Optical Fibre Sagnac Interferometer: An Overview of Its Principles and Applications." *Measurement Science and Technology*, 17, R1–R16.

[48] Bhatiat, V., Murphyt, K. A., Claust, R. O., Tran, T. A., and Greene, J. A. (1995). "Recent Developments in Optical-fiber-based Extrinsic Fabry-Perot Interferometric Strain Sensing Technology." *Smart Materials and Structures*, 4, 244-251.

[49] Easley, C. J., Legendre, L. A., Roper, M. G., Wavering, T. A., Ferrance, J. P., Landers, J. P. (2005). "Extrinsic Fabry-Perot Interferometry for Noncontact Temperature Control of Nanoliter-volume Eenzymatic Reactions in Glass Microchips." *Analytic Chemistry*, 77(4), 1038-45.

[50] Zhang, Y. (2005). *Miniature Fiber-optic Multicavity Fabry-Perot Interferometric biosensor*, Ph. D Thesis, Virginia Polytechnic Institute and State University, Blacksburg, Virginia, USA.

[51] Maalej, M., Ahmed, S. F. U., Kuang, K. S. C., and Paramasivam, P. (2004). "Fiber Optic Sensing for Monitoring Corrosion-Induced Damage." *Structural Health Monitoring*, 3(2), 165-176.

[52] Wnuk, V. P., Méndez, A., Ferguson, S., and Graver, T. (2005). "Process for Mounting and Packaging of Fibre Bragg Grating Strain Sensors for Use in Harsh Environment Applications." *Proc., SPIE*, CA, 46-54.

[53] Mateus, C. F. R., and Barbosa, C. L (2007). "Harsh environment temperature and strain sensor using tunable VCSEL and multiple fibre Bragg gratings." *Proc.*, Microwave & Optoelectronics, SBMO/IEEE MTT-S, Brazil, 496-498.

[54] Xiao, H., Zhao, W., Lockhard, R., and Wang, A. (1997). "Absolute Sapphire Optical Fibre Sensor for High Temperature Applications." *Proc., SPIE.*, CA, 36-42.

[55] Huang, Y., Wei, T., Zhou, Z., Zhang, Y., Chen, G., and Xiao, H. (2010). "An Extrinsic Fabry– Perot Interferometer-based Large Strain Sensor with High Resolution." *Measurement Science and Technology*, 21(10), 105308.1-8.

[56] Yamakawa, H., Iwaki, H., Mita, A., and Takeda, N. (1999). "Health Monitoring of Steel Structures Using Fiber Bragg Grating Sensors." *Proc., Structural Health Monitoring*, CA, 502-510.

[57] Chen, G., Xiao, H., Huang, Y., Zhou, Z., and Zhang, Y. (2009). "A Novel Long-period Fiber Grating Optical Sensor for Large Strain Measurement." *Proc., SPIE*, CA, 729212.1-12.

[58] Habel, W. R., Hofmann, D., Hillemeier, B., and Basedau, F. (1996). "Fiber Sensors for Damage Detection on Large Structures and for Assessment of Deformation Behavior of Cementitious Materials." *Proc., Engineering Mechanics,* ASCE, CA, 355-358.

[59] Habel, W. R., and Hillemeier, B. (1998). "Non-Reactive Measurement of Mortar Deformation at Very Early Ages by Means of Embedded compliant Fiber-optic Micro Strain Sensors." *Proc., Engineering Mechanics,* ASCE, CA, 799-802.

[60] Habel, W. R., Hofmann, D., and Hillemeier, B. (1997). "Deformation measurement of mortars at early ages and of large concrete components on site by means of embedded fiber-optic microstrain sensors." *Cement and Concrete Composites*, 19(1), 81-102.

[61] Nwosu, D. I., and Kodur, V. K. R. (1999). "Behaviour of Steel Frames under Fire Conditions." *Canadian Journal of Civil Engineering*, 26, 156-167.

[62] Franssen, J. M., Cooke, G. M., and Latham, D. J. (1995). "Numerical Simulation of a Full Scale Fire Test on Loaded Steel Framework." *Journal of Constructional Steel Research,* 35, 377-408.

[63] Tide, R. H. R. (1998). "Integrity of Structural Steel after Exposure to Fire." *Engineering Journal*, 1, 26-38.

[64] Bailey, C. G., Burgess, I. W., and Plank, R. J. (1996). "Computer Simulation of a Full-scale Structural Fire test." *The Structural Engineer*, 74, 93-100.

[65] Vila, P. P. M. R., Lopes, N., Simoes da, L. S., Piloto, P., and Franseen, J. M. (2004). "Numerical Modeling of Steel Beam-columns in Case of Fire-comparison with Eurocode 3." *Fire Safety Journal*, 39, 23-29.

[66] Mousavi, S., Bagchi, A., and Kodur, V. K. R. (2008). "Review of Post-earthquake Fire Hazard to Building Structures." *Canadian Journal of Civil Engineering*, 35, 689-698.

[67] National Institute of Standards and Technology (NIST). (2004). *Development of a National R&D Roadmap for Structural Fire Safety Design and Retrofit of Structures*, Report No. NISTIR 7133, NIST, Gaithersburg, MD.

[68] Wainman, D. E., and Kirby, B. R. (1988). *Compendium of UK Standard Fire Test Data for Unprotected Structural Steel*, British Steel Corporation, Swinden Laboratories, Rotherham.

[69] Eurocode 3. (1990). *Design of Steel Structures, Part 1-2: Structural Fire Design*, Commission of European Communities, London, England.

[70] Lennon, T., Moore, D. B., Wang, Y. C., Bailey, and C. G. (2007). *Handbook for the Fire Design of Steel, Composite and Concrete Structures to the Eurocodes*, Thomas Telfor Publishing, Heron Quay, London.

[71] Twilt, T. (1991). *Stress-strain Relationships of Structural Steel at Elevated Temperatures: Analysis of Various Options and European Proposal*, Report No. TNO-BI-91-015, TNO Building and Construction Research, Delft, the Netherlands.

[72] AISC. (1989). *Manual of Steel Construction: Allowable Stress Design*, 9th edition, Miscellaneous Data and Mathematical Tables, Chicago, IL.

[73] Toh, W. S., Tan, K. H., and Fung, T. C. (2001). "Strength and Stability of Steel Frames in Fire: Rankine Approach." *Journal of Structural Engineering*, 127(4), 461-469.

[74] Takagi, J. and Deierlein, G. G. (2007). "Strength Design Criteria for Steel Members at Elevated Temperatures." *Journal of Constructional Steel Research*, 63, 1036-1050.

[75] ASTM. *Standard Test Methods for Fire Tests of Building Construction and Materials*, Code E119-09c, West Conshohocken, PA.

[76] Friswell, M. I., and Mottershead, J. E. (1999). *Finite Element Model Updating in Structural Dynamics*, Kluwer Academic Publishers, Dordrecht, The Netherlands.

[77] Dascotte, E., and Guggenberger, J. (2005). "In Search of Simulating Reality: Validation and Updating of FE Models for Structural Analysis." *Proc., FEM Technology with ANSYS CFX & ICEM CFD*, CAD-FEM, Planegg, Germany. 1-10.

[78] Brownjohn, J. M. W., Xia, P. Q., Hao, H., and Xia, Y. (2001). "Civil Structure Condition Assessment by FE Model Updating: Methodology and Case Studies." *Finite Elements in Analysis and Design*, 37, 761-775.

[79] ABAQUS/Standard User's Manual 6.9-1

[80] Sargent, R. G. (1994). "A Historical View of Hybrid Simulation/analytic Models." *Proc., Winter Simulation*, SCS, CA, 383-386

[81] Kendra, J. R., and Sarabandi, K. (1999). "A Hybrid Experimental/Theoretical Scattering Model for Dense Random Media." *IEEE Transactions of Geosciences and Remote Sensing*, 37(1), 21-35.

[82] Huang, Z., Kosterev, D., Guttromson, R., and Nguyen, T. (2006). "Model Validation with Hybrid Dynamic Simulation." *Proc., Power Engineering Society General Meeting*, IEEE, Montreal, Quebce, 1-9.

[83] Lin, Z. X., Jiang, F. F., and Tang, Y. Q. (2012). "Multi-scale Analyses on Seismic Damage and Progressive Failure of Steel Structures." *Finite Elements in Analysis and Design*, 48, 1358–1369.

[84] AISC. (2005). *Specification for Structural Steel Buildings*, ANSI/AISC360-05, ASIC Inc., Chicago, IL.

[85] Pavan, A. (2008). *Blind Prediction of a Full-scale 3D Steel Frame Tested under Dynamic Conditions*, Master Thesis, Unversity of Pavia, Lombardy, Italy.

[86] Claus, R. O., Gunther, M. F., Wang, A., and Murphy, K. A. (1992). "Extrinsic Fabry-Perot Sensor for Strain and Crack Opening Displacement Measurements from -200 to 900 Degrees C." *Smart Materials and Structures*, 1(3), 237-242.

[87] Cibula, E., and Donlagic, D. (2007). "In-line Short Cavity Fabry-Perot Strain Sensor for Quasi Distributed Measurement Utilizing Standard OTDR." *Optics Express*, 15(14), 8719-8730.

[88] Liu, T., and Fernando, G. F. (2000). "A Frequency Division Multiplexed Low-finesse Fiber Optic Fabry-Perot Sensor System for Strain and Displacement Measurements." *Review of Scientific Instruments*, 71(3), 1275-1278.

[89] Qi, B., Pickrell, G. R., Xu, J., Zhang, P., Duan, Y., Peng, W., Huang, Z., Huo, W., Xiao, H., May, G. R., and Wang, A. (2003). "A Novel Data Processing Techniques for Dispersive White Light Interferometer." *Optical Engineering*, 42(11), 3165-3171.

[90] Kuang, K. S. C., Quek, S. T., Tan, C. Y., and Chew, S. H. (2008). "Plastic Optical Fiber Sensors for Measurement of Large Strain in Geo-textile Materials." *Advanced Materials Research*, 47(50), 1233-1236.

[91] Kuang, K. S. C., Quek, S. T., and Maalej, M. (2004). "Assessment of An Extrinsic Polymer-based Optical Fibre Sensor for Structural Health Monitoring." *Measurement Science and Technology*, 15(10), 2133-2141.

[92] Kuang, K. S. C., Quek, S. T., Koh, C. G., Cantwell, W. J., and Scully, P. J. (2009). "Plastic Optical Fiber Sensors for Structural Health Monitoring: A Review of Recent Progress." *Journal of Sensors*, 2009, 312053-66.

[93] Liehr, S., Lenke, P., and Krebber, K. (2008). "Distributed Strain Measurement with Polymer Optical Fibers Integrated into Multifunctional Geo-textiles." *Proc., SPIE*, CA, Article No.700302.

[94] Lenke, P., Liehr, S., Krebber, K., Weigand, F., and Thiele, E. (2007). "Distributed Strain Measurement with Polymer Optical Fiber Integrated in Technical Textiles Using the Optical Time Domain Reflectometry Technique." *Proc., Plastic Optical Fiber*, Turin, Italy, 21–24.

[95] Taylor, H. F. (2008). *Fiber Optic Sensor*, 2th edition, CRC Press, Boca Raton, FL.

[96] Han, M., and Wang, A. (2004). "Exact Analysis of Low-finesse Multimode Fiber Extrinsic Fabry-Perot Interferometers." *Applied Optics*, 43, 4659-4666.

[97] National Institute of Standards and Technology (NIST). (2006). *Federal Building and Fire Safety Investigation of the World Trade Center Disaster: Final Report on the Collapse of the World Trade Center Towers,* Report No. NIST-NCSTAR-1, NIST, Gaithersburg, MD.

[98] Eagar, T. W. and Musso, C. (2001). "Why Did the World Trade Center Collapse? Science, Engineering, and Speculation." *Journal JOM*, 53 (12), 8-11.

[99] Han, Y. G., and Lee, S. B. (2005). "Discrimination of Strain and Temperature Sensitivities Based on Temperature Dependence of Birefringence in Long-Period Fiber Gratings." *Japanese Journal of Applied Physics*, 44 (6A), 3971–3974.

[100] Bey, S. K. A. K., Sun, T., and Grattan, K. T. V. (2008). "Simultaneous Measurement of Temperature and Strain with Long Period Grating Pairs Using Low Resolution Detection." *Sensors and Actuators*, 144, 83-89.

[101] Han, Y. G., Lee, S. B., Kim, C. S., Kang, J. U., Paek, U. C., and Chung, Y. (2003). "Simultaneous Measurement of Temperature and Strain Using Dual Long-period Fiber Gratings with Controlled Temperature and Strain Sensitivities." *Optics Express*, 11(5), 476-481.

[102] Rao, Y. J., Ran, Z. L., Liao, X., and Deng, H. Y. (2007). "Hybrid LPFG/MEFPI Sensor for Simultaneous Measurement of High-temperature and Strain." *Optics Express*, 15(22), 14936-14941.

[103] Li, Y. J., Wei, T., Montoya, J. A., Saini, S. V., Lan, X. W., Tang, X. L., Dong, J. H., and Xiao, H. (2008). "Measurement of CO_2-laser-irradiation-induced Refractive Index Modulation in Single-mode Fiber toward Long- period Fiber Grating Design and Fabrication." *Applied Optics*, 47(29), 5296-5304.

[104] Kim, B. H., Park, Y., Ahn, T. J., Kim, D. Y., Lee, B. H., Chung, Y., Paek, U. C., and Han,W. T. (2001). "Residual Stress Relaxation in Core of Optical Fibers by CO_2 Laser Irradiations." *Optics Letters*, 26, 1657-1659.

[105] Anemogiannis, E., Glytsis, E. N., and Gaylord, T. K. (2003). "Transmission Characteristics of Long-period Fiber Gratings Having Arbitrary Azimuthal/radial Refractive Index Variations." *Journal of Light-wave Technology*, 21(1), 218-227.

[106] Erdogan, T. (1997). "Cladding-mode Resonances in Short- and Long-period Fiber Grating Filters." *Journal of Optical Society of America A*, 14(8), 1760-1773.

[107] MacDougall, T. W., Pilevar, S., Haggans, C. W., and Jackson, M. A. (1998). "Generalized Expression for the Growth of Long Period Grating." *IEEE Photonics Technology Letters*, 10(10), 1449-1451.

[108] Zhou, G. D., Li, H. N., Liang, R., and Li, D. S. (2006). "Influencing Parameters Analysis of Strain Transfer in Optic Fiber Bragg Grating Sensors." *Proc. of SPIE*, CA, 61790.1-61790.9.

[109] Li, J. L., Zhou, Z., and Ou, J. P. (2005). "Interface Strain Transfer Mechanism and Error Modification for Adhered FBG Strain Sensor." *The International Society for Optical Engineering*, 5851(1), 278-287.

[110] Cook, R. D., and Young, W. C. (1999) *Advanced Mechanics of Materials*, 2nd Edition, Prentice Hall, Upper Saddle River, NJ.

[111] Ma, J., and Tang, W. Z. (1997). "Second-order Sensitivity Effects on Optical Fiber Polarimetric Temperature Sensor and Strain Sensor." *Applied Optics*, 36 (34), 9010-9013.

[112] Rao, Y. J., Yuan, S. F., Zeng, X. K., Lian, D. K., Zhu, Y., Wang, Y. P., Huang, S. L., Liu, T. Y., Fernando, G. F., Zhang, L., and Bennion, I. (2000). "Simultaneous Strain and Temperature Measurement of Advanced 3-D Braided Composite Materials Using An Improved EFPI/FBG System." *Optics Lasers Engineering*, 38, 557-566.

[113] Rao, Y. J., Zeng, X. K., Wang, Y. P., Zhu, T., Ran, Z. L.(2002). "Temperature-strain Discrimination Using A Wavelength-division-multiplexed Chirped in-fibre-Bragg-grating/extrinsic Fabry-Perot Sensor System." Proc., Technical Digest, OFS, Portland, 207-210.

[114] Nguyen, L. V., Hwang, D., Moon, D. S., and Chung, Y. (2009). "Simultaneous Measurement of Temperature and Strain Using A Lyot Fiber Filter Incorporated with A Fiber Bragg Grating in A Linear Configuration." *Measure Science and Technology*, 20, 034006-11.

[115] Han, Y. G. and Lee, S. B. (2003). "Simultaneous Measurement of Temperature and Strain Using Dual Long-period Fiber Gratings with Controlled Temperature and Strain Sensitivities." *Optics Express*, 11(5), 476-481.

[116] Frazao, O., Baptista, J. M., and Santos, J. L. (2007). "Temperature Independent Strain Sensor Based on A Hi-Bi Photonic Crystal Fiber Loop Mirror." *IEEE Journal Sensors*, 7, 1453-1455.

[117] Zhao, C. L., Zhao, J. R., Jin, W., Ju, J., Cheng, L., and Huang, X. G. (2009). "Simultaneous Strain and Temperature Measurement Using A Highly Birefringence Fiber Loop Mirror and A Long-period Grating Written in A Photonic Crystal Fiber." *Optics Communications*, 282, 4077-4080.

[118] Rao, Y. J., Ran, Z. L., Liao, X., and Deng, H. Y. (2007). "Hybrid LPFG/MEFPI Sensor for Simultaneous Measurement of High-temperature and Strain." *Optics Express*, 15(22), 14936-14941.

[119] Dandridge, A., Tveten, A. B., Kersey, A. D., and Yurek, A. M. (1987). "Multiplexing of Interferometric Sensors Using Phase-generated Carrier Techniques." *Electronics letters*, 23(13), 665-666.

[120] Rao, Y. J., Jiang, J., and Zhou, C. X. (2005). "Spatial-frequency-multiplexed Fiber-Optic Fizeau Strain Sensor System with Optical Amplification." *Sensers and Actuators A*, A120, 354-359.

[121] Zhou, C. X., Rao, Y. J., and Jiang, J. (2004). "A Coarse-wavelength-division-multiplexed Extrinsic Fiber Fabry–Perot Sensor System," *Proc., SPIE*, CA, 5634-32.

[122] Kersey, A. D., Dorsey, K. L., and Dandridge, A. (1988). "Demonstration of An Eight-element Time-division Multiplexed Interferometric Fiber Sensor Array." *Electronics Letters*, 24(11), 689-691.

[123] Wentworth, R., Youngquist, R., Tur, M., Byoung, K., and Shaw, H. (1985). "Coherence Multiplexing of Fiber-optic Interferometric Sensors." *Journal of Light Wave Technology*, LT-3(5), 1062-72.

[124] Kersey, A. D. (1992). "Demonstration of A Hybrid Time/wavelength Division Multiplexed Interferometric Fiber Sensor Array." *Electronics Letters*, 27(7), 554-555.

[125] Chen, G., Xiao, H., Huang, Y., Zhang, Y., and Zhou, Z. (2010). "Simultaneous Strain and Temperature Measurement Using Long-period Fiber Grating Sensors." *Proc., SPIE*, CA, 7649-59.

[126] Zhang, B., and Kahrizi, M. (2007). "High Temperature Resistance Fiber Bragg Grating Temperature Sensor Fabrication." *IEEE Sensors Journal*, 7(4), 586-591.

[127] Iding, R., Bresler, B., and Nizamuddin, Z. (1977). *Fires-T3 A Comupter Program for the Fire Response of Structures—Thermal*, Report No. NIST-GCR-95-682, NIST, Gaithersburg, MD.

[128] Morente, F., Quintana, J., and Wald, F. (2005). *Natural Fire Safety Concept, Part 4: Software for Fire Design*, Valorisation Project Report No. RFS-C2-03048, Dissemination of Structural Fire Safety Engineering Knowledge – DIFISEK, UK.

[129] ASCI. (2003). *Facts for Steel Buildings-Fire*, ASCI, Chicago, IL.

[130] SFPE. (2002). *Handbook of Fire Protection Engineering*, 3rd Edition, SFPE, Bethesda, MD.

[131] BSI. (2003). *Application of Fire Safety Engineering Principles to the Design of Buildings: Structural Response and Fire Spread beyond the Enclosure of Origin*, BSI, London, UK.

[132] Poling, B. E. , Prausnitz, J. M., O'Connell, J. P. (2000). *The Properties of Gases and Liquids, Chapter 1: The Property of Gases*, 5th Edition, McGraw-Hill Professional, Berkshire, UK.

[133] Clancy, L. J. (1975). *Aerodynamics*, John Wiley & Sons, Hoboken, NJ.

[134] Gomez-Mares, M., Munoz, M., and Casal, J. (2009). "Axial Temperature Distribution in Vertical Jet Fires." *Journal of Hazardous Materials*, 172, 54-60.

[135] Meier, W., Barlow, R. S., Chen, Y. L., and Chen, J. Y. (2000). "Raman/Rayleigh/LIF Measurements in a Turbulent CH4/H2/N2 Jet Diffusion Flame: Experimental Techniques and Turbulence-Chemistry." *Interaction Combustion Flame*, 123, 326-343.

[136] Wolberg, J. (2006). *Data Analysis Using the Method of Least Squares: Extracting the Most Information from Experiments*, Springer, New York.

[137] Bozorgnia, Y., and Bertero, V. (2004). *Earthquake Engineering: From Engineering Seismology to Performance- Based Engineering*, CRC Press, Boca Raton, FL.

[138] Vaish, A. K. (1974). "Earthquake Finite Element Analysis of Structure-Foundation Systems." *Journal of the Engineering Mechanics Division*, 100(6), 1101-1116.

[139] Yun, G. J., Ghaboussi, J., and Elnashai, A. S. (2007). *Modelling of Hysteretic Behaviour of Beam-column Connections Based on Self-learning Simulation*, MAE Center Report No. 07-13, Mid-America Earthquake Centre, IL.

[140] Maheshwari, B. K., Truman, K. Z., Gould, P. L., and El Naggar, M. H. (2005). "Three-Dimensional Nonlinear Seismic Analysis of Single Piles Using Finite Element Model: Effects of Plasticity of Soil." *International Journal of Geomechanics*, 5(1), 35-45.

[141] Wilson, E. L. (1998). *Three Dimensional Static and Dynamic Analysis of Structures: A Physical Approach with Emphasis on Earthquake Engineering: Chapter 17 Seismic Analysis Modeling to Satisfy Building Codes*, Computers and Structures, Inc., Berkeley, CA.

[142] Ghosh, S., Lee, K., and Raghavan, P. (2001). "A Multi-level Computational Model for Multi-scale Damage Analysis in Composite and Porous Materials." *International Journal of Solids and Structures*, 38(14), 2335-2385.

[143] Li, J., Zhang, J., Ge, W., and Liu, X. (2004). "Multi-scale Methodology for Complex Systems." *Chemical Engineering Science*, 59, 1687-1700.

[144] Seible, F., and Kingsley, G. R. (1991). *Experimental and Numerical Methods in Earthquake Engineering: Modeling of Concrete and Masonry Structures Subjected to Seismic Loading*, Kluwer, Dordrecht.

[145] Mihai, L. A., and Ainsworth, M. (2009). "An Adaptive Multi-scale Computational Modeling of Clare College Bridge." *Computer Methods in Applied Mechanics and Engineering*, 198, 1839-1847.

[146] Suita, K., Yamada, S., Tada, M., Kasai, K., Matsuoka, Y., and Sato, E. (2007). "E-Defense Tests on Full-Scale Steel Buildings: Part 2 – Collapse Experiments on Moment Frames." *Proc., Structures Congress*, ASCE, CA, 18(12pages).

[147] Tada, M., Ohsaki, M., Yamada, S., Motoyui, S., and Kasai, S. (2007). "E-Defense Tests on Full-Scale Steel Buildings: Part 3 - Analytical Simulation of Collapse." *Proc., Structures Congress*, ASCE, CA, 19 (12pages).

[148] Hart, G. C. (1982). *Uncertainty analysis, loads, and safety in structural engineering, Prentice-Hall*, Upper Saddle River, NJ.

[149] Gervasio, H., Silva, L. S., and Borges, L. (2004). “Reliability Assessment of the Post-Limit Stiffness and Ductility of Steel Joints.” *Journal of Constructional Steel Research*, 60, 635-648.

VITA

Ms. Ying Huang was born in Yiyang, Hunan, the People's Republic of China. She was admitted to Guangzhou University, Guangzhou, China in 2002 and received her B.S. degree in Civil Engineering in 2006. After that, she began her graduate study in Harbin Institute of Technology, Harbin, China and received her M.S. degree in Civil Engineering in 2008.

Since August 2008, Ms. Ying Huang has been enrolled in the Ph.D. Program in Civil Engineering at Missouri University of Science and Technology (formerly University of Missouri-Rolla), Rolla, Missouri, USA. She has served both as a Graduate Research Assistant and Graduate Teaching Assistant between August 2008 and July 2012 in the Department of Civil, Architectural, and Environmental Engineering. During this period, her research interests were focused on structural health monitoring and smart structures involving the innovation and application of optical fiber sensors and sensing systems. Based on her dissertation work, she has authored and co-authored a dozen publications including one book chapter, four journal articles, and seven conference papers. In addition, she has published five papers in the general area of structural health monitoring and involved in two U.S. patent and one Chinese patent applications. In August 2012, she received her Ph.D. degree in Civil Engineering from Missouri University of Science and Technology, Rolla, Missouri.